

NASA/TM-2012-217593



Parametric Study of Decay of Homogeneous Isotropic Turbulence Using Large Eddy Simulation

*R. C. Swanson, Christopher L. Rumsey, Robert Rubinstein, Ponnampalam Balakumar, and Thomas A. Zang
Langley Research Center, Hampton, Virginia*

August 2012

NASA STI Program . . . in Profile

Since its founding, NASA has been dedicated to the advancement of aeronautics and space science. The NASA scientific and technical information (STI) program plays a key part in helping NASA maintain this important role.

The NASA STI program operates under the auspices of the Agency Chief Information Officer. It collects, organizes, provides for archiving, and disseminates NASA's STI. The NASA STI program provides access to the NASA Aeronautics and Space Database and its public interface, the NASA Technical Report Server, thus providing one of the largest collections of aeronautical and space science STI in the world. Results are published in both non-NASA channels and by NASA in the NASA STI Report Series, which includes the following report types:

- **TECHNICAL PUBLICATION.** Reports of completed research or a major significant phase of research that present the results of NASA Programs and include extensive data or theoretical analysis. Includes compilations of significant scientific and technical data and information deemed to be of continuing reference value. NASA counterpart of peer-reviewed formal professional papers, but having less stringent limitations on manuscript length and extent of graphic presentations.
- **TECHNICAL MEMORANDUM.** Scientific and technical findings that are preliminary or of specialized interest, e.g., quick release reports, working papers, and bibliographies that contain minimal annotation. Does not contain extensive analysis.
- **CONTRACTOR REPORT.** Scientific and technical findings by NASA-sponsored contractors and grantees.

- **CONFERENCE PUBLICATION.** Collected papers from scientific and technical conferences, symposia, seminars, or other meetings sponsored or co-sponsored by NASA.
- **SPECIAL PUBLICATION.** Scientific, technical, or historical information from NASA programs, projects, and missions, often concerned with subjects having substantial public interest.
- **TECHNICAL TRANSLATION.** English-language translations of foreign scientific and technical material pertinent to NASA's mission.

Specialized services also include organizing and publishing research results, distributing specialized research announcements and feeds, providing information desk and personal search support, and enabling data exchange services.

For more information about the NASA STI program, see the following:

- Access the NASA STI program home page at <http://www.sti.nasa.gov>
- E-mail your question to help@sti.nasa.gov
- Fax your question to the NASA STI Information Desk at 443-757-5803
- Phone the NASA STI Information Desk at 443-757-5802
- Write to:
STI Information Desk
NASA Center for AeroSpace Information
7115 Standard Drive
Hanover, MD 21076-1320

NASA/TM-2012-217593



Parametric Study of Decay of Homogeneous Isotropic Turbulence Using Large Eddy Simulation

*R. C. Swanson, Christopher L. Rumsey, Robert Rubinstein, Ponnampalam Balakumar, and
Thomas A. Zang
Langley Research Center, Hampton, Virginia*

National Aeronautics and
Space Administration

Langley Research Center
Hampton, Virginia 23681-2199

August 2012

The use of trademarks or names of manufacturers in this report is for accurate reporting and does not constitute an official endorsement, either expressed or implied, of such products or manufacturers by the National Aeronautics and Space Administration.

Available from:

NASA Center for AeroSpace Information
7115 Standard Drive
Hanover, MD 21076-1320
443-757-5802

Abstract

Numerical simulations of decaying homogeneous isotropic turbulence are performed with both low-order and high-order spatial discretization schemes. The turbulent Mach and Reynolds numbers for the simulations are 0.2 and 250, respectively. For the low-order schemes we use either second-order central or third-order upwind biased differencing. For higher order approximations we apply weighted essentially non-oscillatory (WENO) schemes, both with linear and nonlinear weights. There are two objectives in this preliminary effort to investigate possible schemes for large eddy simulation (LES). One is to explore the capability of a widely used low-order computational fluid dynamics (CFD) code to perform LES computations. The other is to determine the effect of higher order accuracy (fifth, seventh, and ninth order) achieved with high-order upwind biased WENO-based schemes. Turbulence statistics, such as kinetic energy, dissipation, and skewness, along with the energy spectra from simulations of the decaying turbulence problem are used to assess and compare the various numerical schemes. In addition, results from the best performing schemes are compared with those from a spectral scheme. The effects of grid density, ranging from 32 cubed to 192 cubed, on the computations are also examined. The fifth-order WENO-based scheme is found to be too dissipative, especially on the coarser grids. However, with the seventh-order and ninth-order WENO-based schemes we observe a significant improvement in accuracy relative to the lower order LES schemes, as revealed by the computed peak in the energy dissipation and by the energy spectrum.

Nomenclature

A = Jacobian matrix

ADM = Approximate Deconvolution Model

CFD = Computational Fluid Dynamics

DIA = Direct Interaction Approximation

DNS = Direct Numerical Simulation

DSM = Differential Stress Model

E = specific total energy

$E(\kappa)$ = energy as a function of wave number in Fourier space

ENO = Essentially Non-Oscillatory (numerical scheme)

FCT = Flux-Corrected Transport (numerical scheme)

G = LES convolution kernel

\mathcal{H}_i = sum of heat flux plus work done by stresses

L = length scale

LED = Local Extremum Diminishing

LES = Large Eddy Simulation

ILES = Implicit LES

M = Mach number

MILES = Monotone Implicit LES

MUSCL = Monotone Upstream-centered Schemes for Conservation Laws (numerical scheme)

PPM = Piecewise Parabolic Method (numerical scheme)

Pr = Prandtl number

Q_i = subgrid scale heat flux

R = gas constant

Re = Reynolds number

Re_λ = Taylor microscale Reynolds number

RK = Runge-Kutta

$\bar{S} = (2\bar{S}_{ij}\bar{S}_{ij})^{1/2}$

\bar{S}_{ij} = strain rate tensor

S_k = velocity derivative skewness factor
 SGS = Sub-Grid Scale
 SSM = Scale-Similarity Model
 T = temperature
 \mathcal{T}_{ij} = total stress tensor
 TVD = Total Variation Diminishing (numerical scheme)
 U = velocity
 U_i = state vector
 WENO = Weighted ENO (numerical scheme)
 WENO-L = Linear version of WENO (numerical scheme)
 c_p = specific heat constant
 c_s = constant in Smagorinsky SGS model
 c_v = specific heat at constant volume
 e = internal energy per unit volume
 f = represents general variable; also represents numerical flux
 k = filtered stress kinetic energy; also used as an index counter
 p = pressure
 t = time
 t = time
 t^* = time, nondimensionalized by U_{ref} and L_{ref}
 u_i = velocity component u, v, w
 x_i = Cartesian component x, y, z

Greek:

Δ = LES filter width; also represents a spatial difference
 $\bar{\Delta}$ = LES grid filter
 β_k = smoothness measure of WENO scheme
 δ_{ij} = Kronecker delta
 ϵ = turbulent dissipation rate
 ϵ_w = parameter to prevent division by zero in WENO weights
 γ = ratio of specific heats
 η = Kolmogorov length scale
 κ = wave number in Fourier space
 κ' = coefficient of thermal conductivity
 $\bar{\kappa}$ = variable in the MUSCL scheme
 λ = Taylor microscale
 μ = dynamic viscosity
 ν = kinematic viscosity
 ρ = density
 σ_{ij} = laminar part of the stress tensor
 τ = Kolmogorov time scale
 τ_{ij} = subgrid scale stress
 χ = ratio of compressible kinetic energy to total kinetic energy
 ω_k = weights of WENO scheme
 ϕ = represents general space-time variable

Subscripts, Superscripts, and Special Symbols:

overbar = resolved part; also spatially-filtered variable
 tilde = Favre-averaged variable
 angled brackets = average over all cells in the domain
 C = compressible
 I = incompressible

L = left
 R = right
 ref = reference
 rms = root-mean square
 t = turbulent
 x, y, z = in x, y, z directions
 0 = initial
 ∇ = mathematical “del” differential operator

1 Introduction

1.1 General Description of DNS and LES

Advancements in computer power, both processing speed and memory, in recent years and the need for improved representation of the effects of turbulence in practical engineering computations has encouraged increased interest in direct numerical simulation (DNS) and large eddy simulation (LES). In DNS the full Navier-Stokes equations are solved, and all the relevant scales, down to the Kolmogorov scale, of a physical problem are resolved. Unfortunately, even with the current computer capability, the computational requirements for DNS are too demanding for high Reynolds number (Re) problems since the number of grid points required is proportional to $Re^{9/4}$. Furthermore, as indicated by Piomelli [1], the computational cost scales like Re^3 . For these reasons DNS has generally been applied to flow problems with relatively low Re and simple geometries. Instead of resolving all the relevant scales of the turbulent motion, LES relies upon the assumption that the smaller scales of the turbulent motion have a more universal behavior that allows their effect (due to energy dissipation) on the larger scales to be represented by appropriate modeling. By modeling the physics of the smallest scales there is a significant reduction in the computational requirements relative to DNS, allowing the possibility to compute high Re turbulent flows over complex geometric configurations. There are two general approaches to LES. One involves the filtering of the Navier-Stokes equations in order to eliminate scales smaller than a prescribed value. The filtering introduces additional stresses and heat fluxes that are determined by the unresolved small scale (sub-grid scale) eddies. This approach relies on direct (explicit) modeling of the additional terms, and it is often called conventional or explicit LES. The second LES formulation depends on the numerical dissipation associated with the spatial discretization of the flow equations to emulate the physics of the smallest scales. This approach is called integrated or implicit LES (ILES).

1.2 Conventional LES Methods

In conventional LES the filtering to separate the large energy carrying eddies from the unresolved small scales is designed to remove the scales equal to or smaller than some filter width. This filter width is frequently represented by Δ , and it defines the characteristic resolution length. For the LES $\Delta \gg \eta$, with $\eta = O(Re^{-3/4})$ denoting the Kolmogorov length scale, whereas for DNS there is no “filter” so it is equivalent to LES with $\Delta \approx \eta$. The ultimate success in the LES computation depends upon how well the effects of the filtered scales on the larger resolved scales are represented. The explicit subgrid-scale (SGS) models of conventional LES have two general classifications: functional models and structural models. There are also mixtures of these two types (e.g., functional models with insufficient dissipation of the small scales also require some type of additional dissipation).

Functional models represent the subgrid terms (i.e., stress tensor and heat flux vector) indirectly by modeling the effect of the dissipative action of the small scales on the larger scales, whereas structural models represent the subgrid terms directly by approximating the unfiltered flow variables. One example of a functional model of the subgrid scale stress tensor is the Smagorinsky model [2]. With this algebraic eddy viscosity model the SGS stress tensor is a function of the mean strain rate

tensor and the square of the filter width, which is usually taken as the mesh cell size. There is also a constant that must be specified. An improvement of this methodology is the dynamic Smagorinsky model [3], which replaces the square of the constant by a coefficient that is dynamically adjusted according to information available at the smallest resolved scales. In general, eddy-viscosity models can reproduce SGS dissipation but not the subgrid forces in the filtered momentum equations.

In the case of the structural models the objective is to reconstruct some of the SGS information directly by generating a new solution field from the filtered one, resulting in an improved approximation of the unfiltered field. Structural models are generally superior to functional models because they do not have the isotropic assumption that most functional models have. Some examples of structural models are the scale-similarity model (SSM) and mixed model of Bardina et al. [4], the differential stress equation model (DSM) of Deardorff [5], and the approximate deconvolution model (ADM) of Stolz and Adams [6, 7]. In essence, the scale similarity hypothesis [4] assumes that the effect of the smallest resolved scales on the unresolved scales is similar to the effect of the largest resolved scales on the smallest resolved scales. Based on this similarity assumption, the SSM approximates the SGS stress tensor using the resolved velocity field and a second application of the spatial filter. Due to the filtering process this model allows for backscatter (i.e., energy transfer from the subgrid scales to the resolved scales). The DSM [5] uses a transport equation to model the subgrid stress tensor. For the ADM [6, 7] the unfiltered velocity is estimated by an approximate deconvolution operation, which uses an approximation of the inverse filter kernel. Like the SSM, the ADM does not have adequate dissipation of energy. In order to represent the energy transfer from the resolved to unresolved scales, an additional relaxation is included in the discrete equations. This is equivalent to an explicit filtering of the resolved velocity field at each time step in the evolution of the solution. As pointed out by Grinstein and Fureby [8], a principal difficulty with explicit SGS models is the need to separate the effects of explicit filtering and SGS reconstruction models from those due to discretization.

1.3 ILES Methods

In general, one could classify any LES method that uses numerical dissipation rather than an explicit model to represent the effect of the subgrid scales as an ILES method. According to Sagaut [9] any ILES approach is implicitly based on the following hypothesis: *The action of subgrid scales on the resolved scales is equivalent to a strictly dissipative action.* The numerical dissipative terms are produced when approximating the convective terms in the fluid dynamic equations. These terms are usually either introduced implicitly through an upwind scheme framework or explicitly when using a central difference scheme. The numerical dissipation plays several roles. One role is to ensure numerical stability. In the linear sense, assuming well-posedness and consistency, stability is a necessary and sufficient condition for convergence (Lax equivalence theorem, see Richtmyer and Morton [10]). It is not a sufficient condition to guarantee physically realizable solutions. To ensure a unique and physically meaningful solution the dissipation must also allow satisfaction of an entropy condition. Another role for dissipation is to prevent oscillations in the solution when extrema occur due to physical phenomena such as shock waves and contact discontinuities. There is, in general, a reduction in the approximation order (e.g., second-order schemes become first order) for the convective terms at discontinuities in order to enable discontinuity capturing without oscillations. Frequently, the distinction between upwind and central difference methods depends primarily on the nature of the limiting (or switching) that is imposed to change the order of approximation at discontinuities.

A subclass of ILES algorithms is the monotone integrated LES (MILES) schemes. To understand what methods can be placed in this category it is appropriate to provide some historical background and clarification. The MILES schemes are defined to be at least second-order accurate in smooth regions of the flow field. The classification of MILES was created in 1990 by Boris [11] in reference to the flux corrected transport (FCT) scheme introduced by Boris [12] in 1971 and generalized by Boris and Book [13]–[15]. It stems from the fact that the FCT scheme has a predictor-corrector

structure with the first approximate solution determined with a first-order monotone scheme. This initial approximation is then corrected by removing the large dissipative error with a limited anti-diffusion. Through the limiting process monotonicity and positivity conditions are imposed. The monotonicity constraint, which is the underlying FCT principle given in [12] and [13], ensures that no new extrema are created and that there is no growth of existing extrema. The positivity condition prevents positive definite physical quantities (e.g., density) from becoming negative. The resulting algorithm is at least second-order accurate in smooth regions, and it satisfies monotonicity-preserving and positivity-preserving properties. In addition, the algorithm is designed to satisfy the physical properties of global conservation, causality, and locality. Causality simply means that a fluid passing between two locations in a discrete domain must pass through all the cells in the flow path between those locations. Since the FCT scheme is conservative, causality must be satisfied. Locality requires the approximations to derivatives to be compact.

Boris classifies the FCT scheme as a monotone fluid dynamics algorithm. In [16] Boris lists other examples of monotone algorithms: monotone upstream-centered scheme for conservation laws (MUSCL) of van Leer [17] – [21]; piecewise parabolic method (PPM) of Woodward and Colella [22, 23]; total variation diminishing (TVD) schemes of Harten [24, 25], (TVD) schemes of Harten [24, 25], Sweby [26], Yee et al. [27]; and second-order Godunov methods of Colella [28] and Colella and Glaz [29]. Monotone schemes are monotonicity preserving and guarantee a monotone solution if the scheme converges. In addition, convergent monotone methods generate solutions that automatically satisfy an entropy condition. This means that if the scheme is consistent and conservative, then it not only generates a weak solution (Lax-Wendroff theorem [30]) but also a unique solution. Consequently, both smooth and discontinuous flow solutions are necessarily the physically correct solutions. We should also point out that these monotonicity-preserving schemes impose the total variation bounded (TVB) condition, which is a weaker condition than TVD. This is because TVD schemes are at most first-order accurate (see theorems of Godunov [31], Harten [32]).

There are several approaches to building schemes that preserve monotonicity. One is to start with a low-order monotonic scheme and introduce anti-diffusion that is limited to ensure local monotonicity (e.g., FCT scheme). Another approach is to use a monotone interpolation method (e.g., MUSCL) to determine the primitive variables for reconstruction of the fluxes at the cell interfaces. Limiting is applied to the slopes used in the interpolation to impose monotonicity. A third way is to blend low-order and high-order diffusive terms and choose appropriate coefficients to ensure that the scheme is positive; and thus, the scheme is local extremum diminishing (LED). The concept of LED was introduced by Jameson [33, 34] to provide a theoretical foundation for extending the non-oscillatory design principle (i.e., principle of nonincreasing maxima and nondecreasing minima) to multiple dimensions, since the TVD property is a one-dimensional concept. In all of these methods the limiter must satisfy certain properties. In general, these are natural averaging properties and the property to ensure satisfaction of local monotonicity (e.g., LED). These schemes are also designed to preserve positivity. In addition, by relaxing the LED property (i.e., essentially LED), these schemes can be made higher order even at smooth extrema. Although most of the theory for non-oscillatory algorithms has been developed using scalar equations and constant coefficient one-dimensional systems, these nonlinear high-resolution schemes have proved to be effective for the multidimensional nonlinear systems of fluid dynamics.

So far we have discussed primarily second-order non-oscillatory methods, with some limited reference to the third-order scheme called PPM, which is based on a piecewise quadratic representation of the solution. In general, higher order methods (order greater than two) rely upon techniques such as filtering and/or nonlinear coefficients (e.g., essentially non-oscillatory schemes) to prevent oscillations at extrema and to ensure stability (i.e., to prevent unbounded energy growth due to high-frequency error components). For example, Yee and Sjögren [35] developed a class of high-order central difference schemes that apply a multistep filter method that includes high-order linear and nonlinear filters. The linear filter consists of a product of a sensor and either a spectral-like filter or a high-order centered dissipative operator. The nonlinear filter consists of a product of a different sensor and either an artificial compression method indicator or a wavelet sensor and the dissipative

part of a high-resolution shock-capturing algorithm. Another high-order approach for preventing spurious oscillations at extrema includes the essentially non-oscillatory (ENO) and weighted essentially non-oscillatory (WENO) schemes (see Shu [36]). The ENO schemes are Godunov-type schemes that achieve high-order spatial accuracy in smooth regions by a piecewise polynomial approximation of the solution based on cell-averaged values. A nonlinear adaptive procedure is used to automatically choose the smoothest local approximation stencil, and thus, avoid the Gibbs phenomenon at discontinuities (i.e., generation of $O(1)$ spurious oscillations). Both the reconstruction and the resulting scheme are essentially non-oscillatory (i.e., almost TVD). The ENO schemes are essentially non-oscillatory because they allow small spurious oscillations that have size on the order of h^r , where h is the mesh spacing and r is the approximation order of the scheme. Instead of using the optimal stencil, the WENO schemes use a convex combination of the candidate stencils with nonlinear adaptive coefficients (weights). In practice, both the ENO and WENO schemes generally produce solutions without oscillations.

There are also hybrid high-order algorithms that use a WENO algorithm in the neighborhood of discontinuities and non-dissipative algorithms such as a tuned center difference method or spectral method (exponential convergence method) for smooth regions (e.g., Hill and Pullin [37], Costa and Don et al. [38]). Another type of high-order scheme that is frequently used is the compact scheme, which is based upon a Pade differencing operator. Examples of such schemes are the centered sixth-order and fourth-order schemes using five and three points, respectively, employed by Visbal and Rizzeta [39] and Visbal and Gaitonde [40]. They use a high-order low-pass spatial filtering technique to provide dissipation at the high modified wavenumbers (preventing energy build up at the high frequencies) when there are significant dispersion errors due to the spatial discretization. At discontinuities they use a Roe scheme with the MUSCL approach for reconstruction, which produces a third-order upwind-biased scheme in the case of uniform grids. Various types of detection mechanisms have been considered with these compact schemes, and they include: (1) Jameson-type pressure switch, (2) the artificial compression method, (3) multiresolution wavelets, and (4) WENO-type smoothness criteria.

At this point we have simply identified different types of ILES schemes. Now, we need to be more specific about which ILES schemes are appropriate for indirectly introducing a subgrid scale model. Grinstein and Fureby [8] have demonstrated that the leading order truncation error terms for a certain class of ILES methods (i.e., methods having a flux function determined by blending of low-order and high-order fluxes with an appropriate limiter function) provide implicit SGS models that are similar in form to conventional (explicit) mixed SGS models. While a general theory for the ILES approach is yet to be established, the results obtained for fundamental turbulence problems such as isotropic turbulence decay and Taylor-Green vortex problems provide some support to the validity of the approach. Nevertheless, general validity can only be established by directly connecting the ILES methodology to the physical behavior of small scale turbulence.

For both conventional LES (with explicit SGS models) and ILES (for which the SGS model is “implicitly” included through the numerical scheme), the magnitude of the numerical errors relative to the magnitude of the subgrid terms is critical in determining the accuracy of LES computations. There are two fundamental types of numerical errors: discretization (truncation) errors and aliasing errors. The truncation errors are determined by the order of approximation of the terms in the governing flow equations. Aliasing errors are caused by the interaction of nonlinear terms, resulting in high-frequency errors reappearing as low-frequency errors. For central differencing and pure upwind differencing the leading truncation error terms are dispersive and dissipative, respectively. Upwind biased schemes have both types of errors. In order to accurately represent the turbulent kinetic energy spectrum the difference approximation of convective terms must have low dissipation. At the same time, the dissipation should be sufficiently large to suppress oscillations and ensure numerical stability. In addition, there is a need to have appropriate dissipation for shock capturing. There is also a need to have low dispersion errors. For any scheme being used for LES, these numerical errors must be monitored and controlled to ensure that they are sufficiently small so that the dominant errors in the simulation are due to SGS modeling. Only then will it be possible to effec-

tively improve the models and obtain a simulation capability for a broad range of flow conditions. Since many existing schemes use upwind biased spatial differencing for shock capturing, there is clearly a need to investigate and validate these schemes for LES computations.

1.4 Related Work and Current Contribution

Garnier et al. [41] investigated six shock capturing schemes for LES computations. These methods included the following: Jameson scheme with scalar dissipation, Roe scheme with the MUSCL extrapolation procedure and two minmod limiter variations, and three different types of ENO schemes. Their spatial accuracy range was between second and fifth order, and either second-order or third-order TVD Runge-Kutta (RK) schemes were used for time integration. Each scheme was applied to decaying isotropic turbulence problems ignoring viscous effects, and Mach numbers were between 0.2 and 1.0. Simulations were performed for mesh resolutions of 64^3 and 128^3 . The effects of both implicit and explicit SGS models were discussed. Garnier et al. [41] considered a scheme suitable for LES if it satisfied one of the following two conditions: (1) numerical dissipation is much smaller than the physical SGS dissipation, or (2) numerical dissipation mimics that of a SGS model. They concluded that none of the schemes tested satisfied either of these two conditions.

Another study concerning the behavior of high-resolution and high-order methods for implicit LES was performed by Thornber et al. [42]. Their investigation, at low Mach number, was also done for homogeneous decaying turbulence. Computing on mesh densities between 32^3 and 256^3 , they considered seven different schemes with spatial accuracy ranging from second to ninth order. In all simulations the Euler equations were solved with finite-volume methods. For higher order spatial accuracy, cell interface variables were determined by either the MUSCL or WENO approach. Third-order RK schemes were used to advance the solution in time. With grids exceeding 32^3 or with numerical methods having spatial accuracy higher than third order, their results indicated that the growth of large scales and the dissipation of kinetic energy could be captured. Based on energy spectra, Thornber et al. also concluded that all the upwind-biased schemes evaluated were too dissipative at the high wavenumbers, resulting in an early onset of decay in the inertial range. We should point out that with this approach the question does arise concerning an appropriate representation of an inertial subrange in the absence of physical viscous effects (i.e., the physical effects when $Re = \infty$ are clearly not the same as for high Re). Thornber et al. also observed that due to differences in the effective cut-off wavenumber, methods with fifth-order or higher spatial accuracy performed better on a 128^3 grid than those with second-order accuracy on a 256^3 grid.

The primary objective of this report is to compare the behavior of representative second-order finite-volume schemes and high-order finite-difference WENO-based schemes when applied to the problem of isotropic decay of turbulence. The second-order schemes have either central or third-order upwind biased spatial differencing, and for each scheme second-order temporal differencing is used. Both explicit and implicit LES computations are performed with these methods. For the WENO schemes we investigate fifth-order, seventh-order, and ninth-order spatial accuracy for ILES. A RK scheme, which is third-order TVD, is used for time advancement. There is a recognition (Martin et al. [43], Taylor and Martin [44]) that the standard fifth-order WENO scheme with Lax-Friedrichs flux splitting is too dissipative at the higher wavenumbers, as clearly revealed in the energy spectrum. Here, the effect of increasing the order of approximation is discussed. In the simulations, the filtered Navier-Stokes equations are solved. Since the Kolmogorov scale is significantly smaller than the mesh size, Garnier et al. [41] and Thornber et al. [42] indicated either indirectly or directly that the viscous effects are negligible. However, in any practical simulation the viscous terms and their effects are present, regardless of the spatial resolution. This certainly suggests that including these terms is necessary to obtain an effective measure of the wave cut-off number in the energy spectrum. Moreover, as discussed by Ishihara [45], the turbulence statistics have significant Re dependencies, even at high values of Re .

In the initial part of the paper the governing equations are presented. Then the numerical methods are described. This is followed by the results section, which begins by describing the formulation of

the initial solution and providing definitions of the turbulence statistics. In the next part the results from LES simulations are presented. The turbulence results include kinetic energy, dissipation of energy, and skewness. Vorticity and Q-invariant contours are also shown. The initial peak of the energy dissipation during the energy redistribution process clearly reveals the improved accuracy achieved with the higher order WENO schemes. The computed energy spectrum is used to determine the dissipative behavior of the numerical methods over the frequency range. Results with the various numerical schemes are compared with each other. In addition, there are some comparisons with results from a spectral scheme.

2 Governing Equations

2.1 Direct Numerical Simulation (DNS)

Written in strong conservation form, the compressible form of the Navier-Stokes equations is:

$$\frac{\partial \rho}{\partial t} + \frac{\partial \rho u_k}{\partial x_k} = 0 \quad (1)$$

$$\frac{\partial \rho u_i}{\partial t} + \frac{\partial \rho u_i u_k}{\partial x_k} = -\frac{\partial p}{\partial x_i} + \frac{\partial}{\partial x_k} \left[\mu \left(\frac{\partial u_i}{\partial x_k} + \frac{\partial u_k}{\partial x_i} - \frac{2}{3} \delta_{ki} \frac{\partial u_j}{\partial x_j} \right) \right] \quad (2)$$

$$\frac{\partial \rho E}{\partial t} + \frac{\partial [(\rho E + p)u_k]}{\partial x_k} = \frac{\partial}{\partial x_k} \left(\kappa' \frac{\partial T}{\partial x_k} + \left[\mu \left(\frac{\partial u_i}{\partial x_k} + \frac{\partial u_k}{\partial x_i} - \frac{2}{3} \delta_{ki} \frac{\partial u_j}{\partial x_j} \right) \right] u_i \right) \quad (3)$$

where the coefficient of thermal conductivity κ' is taken to be $\kappa' = c_p \mu / \text{Pr}$, and the variable E represents the specific total energy $E = e + (u^2 + v^2 + w^2)/2$. For a perfect gas, $e = c_v T$, $c_v = R/(\gamma - 1)$, $\gamma = c_p/c_v$, and the equation of state is $p = \rho R T$, or:

$$p = (\gamma - 1) \left[\rho E - \frac{1}{2} \rho (u^2 + v^2 + w^2) \right] \quad (4)$$

By definition, DNS is a numerical computation of the Navier-Stokes equations that resolves *all* relevant spatial and temporal scales in a flow field. This means that the grid needs to be fine enough to resolve features on the order of the Kolmogorov dissipation length scale:

$$\eta = (\nu^3 / \varepsilon)^{\frac{1}{4}} \quad (5)$$

where ν is the kinematic viscosity and ε is the dissipation rate. Similarly, the time step needs to be fine enough to resolve temporal dynamics on the order of the Kolmogorov time scale:

$$\tau = (\nu / \varepsilon)^{\frac{1}{2}} \quad (6)$$

It is impossible today to achieve these resolutions at reasonably high Reynolds numbers. Successful low Reynolds number simulations require very low-dissipation schemes to resolve the smallest-scale features with good fidelity. The spatial order of accuracy of the scheme also influences grid requirements. Additional dissipation is required to stabilize some numerical schemes; for example, compact schemes are often stabilized through the use of additional filtering [46]. Note that an under-resolved DNS simulation can exhibit time-dependent features that *appear* to the eye like an adequate DNS simulation, but if the smallest space and time scales are not resolved, some flow physics are being omitted and its validity remains unclear.

2.2 Large Eddy Simulation (LES)

In LES, the Navier-Stokes equations are filtered via a low-pass filter defined as a convolution product:

$$\bar{\phi}(\vec{x}, t) = \int_{-\infty}^{+\infty} \int_{-\infty}^{+\infty} \phi(\vec{\xi}, t') G(\vec{x} - \vec{\xi}, t - t') dt' d^3\xi \quad (7)$$

where $\bar{\phi}(\vec{x}, t)$ is the resolved part of a space-time variable $\phi(\vec{x}, t)$. For the compressible Navier-Stokes equations, the equations contain both ordinary and Favre-filtered variables (see, e.g., Knight et al. [47]). The Favre filter is defined by:

$$\tilde{f} = \frac{\bar{\rho}f}{\bar{\rho}} \quad (8)$$

where the overbar denotes the ordinary spatially filtered variable, and the tilde denotes the Favre-filtered variable. After filtering, the compressible governing equations (Eqs. (1) - (3)) become:

$$\frac{\partial \bar{\rho}}{\partial t} + \frac{\partial \bar{\rho} \tilde{u}_k}{\partial x_k} = 0 \quad (9)$$

$$\frac{\partial \bar{\rho} \tilde{u}_i}{\partial t} + \frac{\partial \bar{\rho} \tilde{u}_i \tilde{u}_k}{\partial x_k} = -\frac{\partial \bar{p}}{\partial x_i} - \frac{\partial \mathcal{T}_{ik}}{\partial x_k} \quad (10)$$

$$\frac{\partial \bar{\rho} \tilde{E}}{\partial t} + \frac{\partial [(\bar{\rho} \tilde{E} + \bar{p}) \tilde{u}_k]}{\partial x_k} = \frac{\partial \mathcal{H}_k}{\partial x_k} \quad (11)$$

where the total stress tensor is $\mathcal{T}_{ik} \equiv \bar{\rho} \tau_{ik} - \bar{\sigma}_{ik}$, and the sum of the heat flux plus work done by the stresses is $\mathcal{H}_k \equiv Q_k + \kappa' \partial \bar{T} / \partial x_k + \mathcal{T}_{ik} \tilde{u}_i$ with κ' typically expressed as $c_p \mu / \text{Pr}$, and $\bar{\sigma}_{ik}$ approximated as:

$$\bar{\sigma}_{ik} = \mu \left(\frac{\partial \tilde{u}_i}{\partial x_k} + \frac{\partial \tilde{u}_k}{\partial x_i} - \frac{2}{3} \delta_{ik} \frac{\partial \tilde{u}_j}{\partial x_j} \right) \quad (12)$$

As a result of the filtering, the effect of the filtered stress kinetic energy ($k \equiv \tau_{ii}/2$) should be included in the definition of the total energy (Knight et al. [47]), that is, $\bar{\rho} \tilde{E} = \bar{\rho} \tilde{e} + \bar{\rho} (\tilde{u}^2 + \tilde{v}^2 + \tilde{w}^2)/2 + \bar{\rho} k$. Then, the equation of state becomes:

$$\bar{p} = (\gamma - 1) \left[\bar{\rho} \tilde{E} - \frac{1}{2} \bar{\rho} (\tilde{u}^2 + \tilde{v}^2 + \tilde{w}^2) - \bar{\rho} k \right] \quad (13)$$

However, for lower speed flows, the effect of k is usually negligible, and many researchers ignore it in the definition of energy and equation of state.

As a result of the filtering, two unknown quantities emerge: the subgrid scale stress τ_{ik} and the heat flux Q_k :

$$\tau_{ik} = \widetilde{u_i u_k} - \tilde{u}_i \tilde{u}_k \quad (14)$$

$$Q_k = -c_p \bar{\rho} \left(\widetilde{u_k T} - \tilde{u}_k \tilde{T} \right) \quad (15)$$

The quantities in Eqs. (14) and (15) must be modeled. As discussed in Sagaut [9], there are two basic methods: explicit modeling and implicit modeling. In explicit modeling, a subgrid model is explicitly introduced. In implicit modeling (ILES), no additional eddy viscosity is introduced into the governing equations, but the numerical method is selected such that the numerical error fulfills desired properties and effectively acts like a subgrid model. With no explicit model present, ILES appears to be functionally similar (from an implementation point of view) to under-resolved

DNS; neither method resolves the finest scales, and both require enough inherent dissipation in the numerical scheme to prevent the non-physical build-up of energy at the smallest resolved scales.

The commonly used Smagorinsky subgrid scale model [2] is an explicit SGS model, which utilizes the Boussinesq assumption for the SGS stress tensor:

$$\tau_{ik} = -2\nu_t \left(\overline{S}_{ik} - \frac{1}{3} \delta_{ik} \overline{S}_{jj} \right) + \frac{2}{3} \delta_{ik} k \quad (16)$$

where the ν_t in the Smagorinsky model is given by:

$$\nu_t = (c_s \overline{\Delta})^2 |\overline{S}| \quad (17)$$

with $|\overline{S}| = \sqrt{2\overline{S}_{ij}\overline{S}_{ij}}$, $\overline{S}_{ij} = (\partial\tilde{u}_i/\partial x_j + \partial\tilde{u}_j/\partial x_i)/2$, and $\overline{\Delta}$ is typically defined by some measure of the local grid spacing, such as $\overline{\Delta} = (\Delta x \Delta y \Delta z)^{(1/3)}$. The c_s term is a constant for the original Smagorinsky model, commonly set to approximately 0.1.

Note that in most subgrid scale models, neither the formal filter function nor the filter width are explicitly defined. Instead, the models have a built-in filter, related to the local grid spacing: for the Smagorinsky model it is $c_s \overline{\Delta}$. This built-in filter controls the size of the smallest locally resolved flow structures. It can be difficult to choose an optimum built-in filter width, which has been noted to be flow dependent. This difficulty has been one reason for the development and subsequent success of the widely used dynamic model of Germano et al. [3]. This model dynamically computes a variable c_s term, rather than setting it to a constant value.

For compressible flows, an SGS viscosity model for the subgrid-scale heat flux is (see Urbin and Knight [48]):

$$Q_k = \frac{\bar{\rho} c_p \nu_t}{\text{Pr}_t} \frac{\partial \tilde{T}}{\partial x_k} \quad (18)$$

3 Numerical Methods

For the current problem of decay of isotropic turbulence, two compressible CFD codes were employed, the NASA production computer code CFL3D [49] and an in-house NASA research code that employs the weighted essentially non-oscillatory (WENO) scheme [36]. Some of the characteristics of these numerical methods will be described next.

3.1 Upwinding and Central Differencing in CFL3D

The CFL3D code is a structured-grid upwind multi-zone CFD code that solves the generalized thin-layer or full Navier-Stokes equations [49]. The code can employ local time-step scaling, grid sequencing and multigrid to accelerate convergence to steady state. A second-order time-accurate mode (using standard backward differentiation formula (BDF)) is used in this study with pseudo-time stepping plus multigrid, and an implicit approximate factorization method to advance the solution to the next physical time step. For the current study, a 3-level W-cycle multigrid strategy was employed, along with 30 sub-iterations (pseudo-time steps) per time step. This number of subiterations was enough to drive the L_2 -norm of the subiteration density residual down approximately 14 orders of magnitude, to near machine zero for the current problem.

The CFL3D code employs a cell-centered finite-volume method. It uses the so-called ‘‘kappa scheme’’ in a MUSCL approach [50] for its spatial differencing for the convective and pressure terms, and second-order central differencing for the viscous terms. Roe’s flux difference-splitting (FDS) method [51] is used to obtain fluxes at the cell faces. In the kappa scheme, the reconstruction

at cell interfaces is accomplished via:

$$U_L = U_i + \frac{1}{4} [(1 - \bar{\kappa})(U_i - U_{i-1}) + (1 + \bar{\kappa})(U_{i+1} - U_i)] \quad (19)$$

$$U_R = U_{i+1} - \frac{1}{4} [(1 + \bar{\kappa})(U_{i+1} - U_i) + (1 - \bar{\kappa})(U_{i+2} - U_{i+1})] \quad (20)$$

where U_i is the state vector at cell center i , and the subscripts L and R refer to the left and right states for a local approximate Riemann solver. The ‘‘standard’’ scheme for CFL3D in RANS applications uses $\bar{\kappa} = 1/3$, which is a third-order upwind-biased stencil on a uniformly spaced Cartesian grid [52]. For the LES applications in the current paper, upwinding was believed to be too dissipative, so for most of the applications the central-differencing option $\bar{\kappa} = 1$ was used. When $\bar{\kappa} = 1$,

$$U_L = U_R = \frac{1}{2}(U_i + U_{i+1}) \quad (21)$$

The Roe-type numerical flux is written as

$$f_{i+1/2} = \frac{1}{2}(f_L + f_R) - \frac{1}{2} |A|_{i+1/2} (U_R - U_L) \quad (22)$$

Since $U_L = U_R$, the dissipative term in Eq. (22) vanishes, and the flux balance for a given cell yields a standard central difference approximation with second-order spatial accuracy. In general, central differencing with no additional dissipation can yield numerical problems such as odd-even point decoupling. However, for the particular case of isotropic turbulence decay considered here, the solutions on the grid sizes considered were stabilized sufficiently by the viscosity of the fluid (although not shown, computations attempted on a very fine grid with 256^3 cells did yield odd-even point decoupling behavior).

The standard Smagorinsky model has been coded into CFL3D, with the constant coefficient c_s specified by the user. When c_s is set to 0, the method becomes an ILES type, with no additional subgrid eddy viscosity model added.

3.2 Weighted Essentially Non-Oscillatory (WENO) Scheme

In this section, for completeness, we present the elements of the weighted essentially non-oscillatory (WENO) scheme and the implementation of this scheme in the present work. To simplify the description of the scheme, we consider a one-dimensional scalar conservation equation

$$\frac{\partial u}{\partial t} + \frac{\partial f(u)}{\partial x} = \frac{\partial f^v(u_x)}{\partial x} \quad (23)$$

where $u = u(x, t)$ is a conserved quantity, $f(u)$ and $f^v(u_x)$ are inviscid and viscous flux functions with u_x denoting the derivative $\partial u / \partial x$, and the independent variables x and t represent space and time, respectively. By taking this approach there is no compromise of the generality of the discussion since the same spatial approximation techniques can be applied in each coordinate direction of a multidimensional fluid dynamics problem. We obtain a semi-discrete form of Eq. (23) by considering a one-dimensional domain with uniform spacing Δx . The unknowns are located at the points $x_i = i\Delta x$, $i = 0, \dots, N$, and cell boundaries are at $x_{i+1/2} = x_i + \Delta x/2$. As seen in Fig. 1, the grid points are also cell centers. The semi-discrete form of Eq. (23) is given by

$$\frac{du_i(t)}{dt} = - \left. \frac{\partial f}{\partial x} \right|_{x=x_i} + \left. \frac{\partial f^v}{\partial x} \right|_{x=x_i} \quad (24)$$

where $u_i(t)$ is a numerical approximation of the point value $u(x_i, t)$. To construct a conservative difference scheme for this system of ordinary differential equations, the fluxes must be evaluated

at the interfaces of the cells to the desired order of accuracy. Since the fifth-order WENO scheme is frequently used in applications, we present the details of the discretization for the derivative of $f(u)$ using a fifth-order finite-difference form of this scheme, following the work of Shu [36], Jiang and Shu [53], Henrick et al. [54], and Borges et al. [55]. After discussing the approximation of convective term, we then consider different methods for discretizing the viscous (i.e., diffusion) term, giving the advantages and disadvantages of each method. Next, we provide a brief discussion of the extension to even higher order based on the paper by Balsara and Shu [56]. In the last part of this subsection we describe the time integration method.

3.2.1 Approximating the Inviscid Term

This section contain three parts. In the first part we consider the linear form of the discretization for the derivative of the convective (inviscid) flux function. This form is dominant in smooth regions of the domain, and it provides a natural foundation for the development of the nonlinear WENO scheme. The final part of this section discusses the flux splitting used to account for different signs of the flux Jacobian.

3.2.1a Linear Form of 5th Order WENO Scheme

Consider the inviscid flux function. One can satisfy the conservative property by defining a numerical flux function $h(x)$ implicitly as

$$f(x) = \frac{1}{\Delta x} \int_{x-\Delta x/2}^{x+\Delta x/2} h(\xi) d\xi \quad (25)$$

so that the spatial derivative of $f(x)$ is exact; and thus,

$$\left. \frac{\partial f}{\partial x} \right|_{x=x_i} = \frac{1}{\Delta x} (h_{i+1/2} - h_{i-1/2}) \quad (26)$$

where $h_{i\pm 1/2} = h(x_{i\pm 1/2})$. The numerical flux function $h_{i\pm 1/2}$ can be approximated by a flux function $\hat{f}_{i\pm 1/2}$ that is defined by a polynomial of sufficient degree to obtain the desired order of accuracy. Then

$$\left. \frac{\partial f}{\partial x} \right|_{x=x_i} \approx \frac{1}{\Delta x} (\hat{f}_{i+1/2} - \hat{f}_{i-1/2}) \quad (27)$$

and

$$\hat{f}_{i+1/2} = h(x_{i+1/2}) + O(\Delta x^r) \quad (28)$$

where r is the desired order of accuracy. The numerical flux function $\hat{f}_{i+1/2}$ depends on the discrete values of the physical flux f at the points which determine the stencil of the approximation.

For the WENO scheme a fifth-order accurate flux $\hat{f}_{i+1/2}$ is computed as a convex combination (i.e., weighted average) of possible third-order approximations. In Fig. 2 the three candidate stencils are shown. The weighted average of the third-order stencils can be expressed as

$$h_{i+1/2} \approx \hat{f}_{i+1/2} = \sum_{k=0}^{r-1} \omega_k \hat{f}_{i+1/2}^k \quad (29)$$

where $r = 3$ and ω_k is the weight corresponding to stencil S_k . To obtain the third-order approximations for each $\hat{f}^k(x)$, we represent each approximate numerical flux function with a second-degree polynomial, and thus

$$h(x) \approx \hat{f}(x) = a_0 + a_1 x + a_2 x^2 \quad (30)$$

with the undetermined coefficients a_k , $k = 0, 1, 2$. Substituting $\hat{f}(x)$ for $h(x)$ in Eq. (25) and integrating we obtain

$$\hat{f}(x) = a_0 + a_1x + a_2 \left(x^2 + \frac{\Delta x^2}{12} \right) \quad (31)$$

The coefficients a_k of the polynomial are determined from values of $f(x)$ at nodes of the grid. Consider the grid cell with boundaries at $x_{i-1/2}$ and $x_{i+1/2}$. To obtain the a_k so that the flux of Eq. (29) produces a fifth-order upstream-centered scheme at the interface $x_{i+1/2}$, the values of $f(x)$ are required at the following three sets of nodes: $\{x_{i-2}, x_{i-1}, x_i\}$, $\{x_{i-1}, x_i, x_{i+1}\}$, $\{x_i, x_{i+1}, x_{i+2}\}$. Evaluating the polynomial of Eq. (31) for each set of nodes gives three algebraic equations that must be solved to obtain the coefficients of the interpolating polynomial. For the evaluations the value of x_i is zero. The numerical flux functions for the three sets of points are

$$\begin{aligned} \hat{f}^0(x) &= \frac{-f_{i-2} + 2f_{i-1} + 23f_i}{24} + \left(\frac{f_{i-2} - 4f_{i-1} + 3f_i}{2\Delta x} \right) x + \left(\frac{f_{i-2} - 2f_{i-1} + f_i}{2\Delta x^2} \right) x^2 \\ \hat{f}^1(x) &= \frac{-f_{i-1} + 26f_i + f_{i+1}}{24} + \left(\frac{f_{i+1} - f_{i-1}}{2\Delta x} \right) x + \left(\frac{f_{i-1} - 2f_i + f_{i+1}}{2\Delta x^2} \right) x^2 \\ \hat{f}^2(x) &= \frac{(23f_i + 2f_{i+1} - f_{i+2})}{24} + \left(\frac{-3f_i + 4f_{i+1} - f_{i+2}}{2\Delta x} \right) x + \left(\frac{f_i - 2f_{i+1} + f_{i+2}}{2\Delta x^2} \right) x^2 \end{aligned} \quad (32)$$

At $i + 1/2$ ($x_{i+1/2} = \Delta x/2$) the fluxes of Eq. (32) become

$$\begin{aligned} \hat{f}_{i+1/2}^0 &= \frac{1}{6}(2f_{i-2} - 7f_{i-1} + 11f_i) \\ \hat{f}_{i+1/2}^1 &= \frac{1}{6}(-f_{i-1} + 5f_i + 2f_{i+1}) \\ \hat{f}_{i+1/2}^2 &= \frac{1}{6}(2f_i + 5f_{i+1} - f_{i+2}) \end{aligned} \quad (33)$$

One can easily show (see Henrick et al. [54]) that the fifth-order flux at $x_{i+1/2}$ for the upstream-centered scheme is given by

$$\hat{f}_{i+1/2} = \frac{1}{60}(2f_{i-2} - 13f_{i-1} + 47f_i + 27f_{i+1} - 3f_{i+2}) \quad (34)$$

Remark: The third-order fluxes of Eq. (33) and the fifth-order flux of Eq. (34) can also be determined by using Table 2.1 in the 1997 paper by Shu [36].

By substituting the third-order approximations of Eq. (33) into Eq. (29) and equating corresponding terms, we obtain the weights

$$\omega_0 = 1/10, \omega_1 = 6/10, \omega_2 = 3/10 \quad (35)$$

which give the desired fifth-order flux function in regions where the solution is smooth. The weights sum to unity, and they are called the ideal weights. To obtain the flux $\hat{f}_{i-1/2}$ for approximating the first derivative of the inviscid flux function f , the stencil for $\hat{f}_{i+1/2}$ is shifted to the left by one mesh point. Substituting for the fluxes in Eq. (27) gives

$$\begin{aligned} \frac{\partial f}{\partial x} \Big|_{x=x_i} &\approx \frac{1}{60\Delta x}(-2f_{i-3} + 15f_{i-2} - 60f_{i-1} + 20f_i + 30f_{i+1} - 3f_{i+2}) \\ &= f'(x) + O(\Delta x^5) \end{aligned} \quad (36)$$

Even though the fluxes at $x_{i-1/2}$ and $x_{i+1/2}$ are only fifth-order accurate and the flux balance of Eq. (27) is divided by Δx , the resulting flux derivative is fifth-order accurate because the two stencils approximating the fluxes only differ by a grid point shift, resulting in a canceling of the lowest order truncation error terms.

3.2.1b 5th Order Non-Oscillatory Weights

So far we have only considered a linear scheme. The approximation of the inviscid flux derivative given by Eq. (36) requires a smooth solution for high-order accuracy. If a discontinuity such as a shock wave occurs in the flow field, oscillations will occur in the discrete solution. The full nonlinear WENO scheme can be designed to give comparable high-order accuracy in smooth regions to that of the linear scheme and prevent spurious oscillations at discontinuities. This is accomplished by introducing appropriate nonlinear weights in Eq. (29) such that the weight of each stencil depends upon its smoothness. In the nonlinear scheme, stencils that cross a shock wave are automatically assigned an essentially zero weight, producing a one-sided upwind difference approximation. Such an approach is similar to what is done with second-order schemes, which use a limiter for shock capturing that produces a first-order upwind difference at shock waves. One can view the nonlinear weights of the WENO scheme as playing the role of a limiter, and by their action, the scheme is essentially non-oscillatory. In the neighborhood of a discontinuity the order of accuracy is reduced. That is, if r is the order of accuracy of the weighted fluxes, then in regions where the solution is smooth the order of accuracy of the scheme is $2r - 1$ and in the vicinity of a shock wave the order of accuracy is reduced to r .

Jiang and Shu [53] define the non-oscillatory weights as

$$\omega_k = \frac{\alpha_k}{\sum_{k=0}^{r-1} \alpha_k}, \quad \alpha_k = \frac{d_k}{(\beta_k + \varepsilon_w)^p} \quad (37)$$

where the α_k are normalized weights, d_k are the ideal weights, and the parameter ε_w is a small positive number used to bound the weights (i.e., to prevent division by zero). For $r = 3$ the exponent $p = 2$ is chosen, since it proves to be adequate to obtain essentially non-oscillatory approximations. The β_k is a smoothness measure of the flux function on the stencil S_k , and it is defined by

$$\beta_k = \sum_{l=1}^{r-1} \Delta x^{2l-1} \int_{x_{i-1/2}}^{x_{i+1/2}} \left(\frac{d^l \hat{f}^k}{dx^l} \right)^2 dx \quad (38)$$

Since $\hat{f}^k = a_0 + a_1 x + a_2 x^2$, the equation for β_k becomes

$$\beta_k = a_1^2 \Delta x^2 + \frac{13}{3} a_2^2 \Delta x^4 \quad (39)$$

when the stencils are centered around $x_i = 0$. Substituting for the coefficients a_1 and a_2 corresponding to each value of k we obtain the smoothness indicators

$$\begin{aligned} \beta_0 &= \frac{13}{12} (f_{i-2} - 2f_{i-1} + f_i)^2 + \frac{1}{4} (f_{i-2} - 4f_{i-1} + 3f_i)^2 \\ \beta_1 &= \frac{13}{12} (f_{i-1} - 2f_i + f_{i+1})^2 + \frac{1}{4} (f_{i+1} - f_{i-1})^2 \\ \beta_2 &= \frac{13}{12} (f_i - 2f_{i+1} + f_{i+2})^2 + \frac{1}{4} (3f_i - 4f_{i+1} + f_{i+2})^2 \end{aligned} \quad (40)$$

which have Taylor series expansions at x_i given by

$$\begin{aligned} \beta_0 &= f_i' \Delta x^2 + \left(\frac{13}{12} f_i''^2 - \frac{2}{3} f_i' f_i''' \right) \Delta x^4 - \left(\frac{13}{6} f_i'' f_i''' - \frac{2}{2} f_i' f_i'''' \right) \Delta x^5 + O(\Delta x^6) \\ \beta_1 &= f_i' \Delta x^2 + \left(\frac{13}{12} f_i''^2 + \frac{2}{3} f_i' f_i''' \right) \Delta x^4 + O(\Delta x^6) \\ \beta_2 &= f_i' \Delta x^2 + \left(\frac{13}{12} f_i''^2 - \frac{2}{3} f_i' f_i''' \right) \Delta x^4 + \left(\frac{13}{6} f_i'' f_i''' - \frac{2}{2} f_i' f_i'''' \right) \Delta x^5 + O(\Delta x^6) \end{aligned} \quad (41)$$

with the prime denoting differentiation (e.g., $f''' = d^3 f/dx^3$). Appropriate smoothness indicators have the following behavior. In regions where the solution is smooth, the β_k are small and about the same size, resulting in weights ω_k that are close to the ideal weights d_k . If the approximation stencil contains a discontinuity, then the associated smoothness measure β_k is $O(1)$, and the corresponding weight ω_k is small relative to the other weights.

When the solution is smooth, a requirement in choosing the appropriate β_k 's is that the corresponding ω_k 's approach the ideal weights at a sufficiently fast convergence rate. Henrick et al. [54] and Borges et al. [55] derive the necessary and sufficient conditions to ensure the design order of accuracy in smooth regions. These conditions are as follows:

$$\sum_{l=1}^{r-1} (\omega_k^\pm - d_k) = O(\Delta x^{2r}) \quad (42)$$

$$\sum_{l=1}^{r-1} A_k (\omega_k^+ - \omega_k^-) = O(\Delta x^r) \quad (43)$$

$$\omega_k^\pm - d_k = O(\Delta x^{r-1}) \quad (44)$$

where A_k is the coefficient (independent of Δx) of the leading term in a Taylor series expansion for $\hat{f}_{i\pm 1/2}^k$, and the superscript \pm refers to this flux function. As indicated by Borges et al. the first condition is always satisfied, since $\sum_{k=0}^{r-1} \omega_k^\pm = \sum_{k=0}^{r-1} d_k$. A sufficient condition for fifth-order convergence is given by

$$\omega_k^\pm - d_k = O(\Delta x^3) \quad (45)$$

Following the analysis of Henrick et al. for the smoothness indicator defined by Eq. (40), one can show that if β_k can be expressed as

$$\beta_k = D[1 + O(\Delta x^{r-1})] \quad (46)$$

where D is a non-zero constant independent of k , then $\omega_k = d_k + O(\Delta x^{r-1})$. When $r = 3$ we readily see from the Taylor series expansions for the β_k 's given in Eq. (41) that Eq. (46) is satisfied, and thus, $\omega_k = d_k + O(\Delta x^2)$. Borges et al. emphasize that the condition of Eq. (43) must be satisfied to achieve the design order of convergence.

At critical points, which are points where the first or higher derivatives of the function f vanish, these conditions are not necessarily satisfied using the β_k given in Eq. (40). For example, if $f' = 0$, we find from the Taylor series expansions of Eq. (41) that $\beta_k = D[1 + O(\Delta x)]$ for $k = 0, 2$, and thus, $\omega_k = d_k + O(\Delta x)$, resulting in third-order convergence. In order to overcome this deterioration in the convergence of the scheme due to critical points, Borges et al. introduced a different definition of the measures of smoothness β_k given by

$$\beta_k^z = \left(\frac{\beta_k + \varepsilon_w}{\beta_k + \tau_5 + \varepsilon_w} \right), \quad k = 0, 1, 2 \quad (47)$$

where $\tau_5 = |\beta_0 - \beta_2|$, and the superscript z indicates that the quantity, a smoothness measure in this case, is associated with the WENO-Z scheme of Borges et al. The corresponding weights ω_k^z are defined as

$$\omega_k^z = \frac{\alpha_k^z}{\sum_{k=0}^{r-1} \alpha_k^z}, \quad \alpha_k^z = \frac{d_k}{\beta_k^z} = d_k \left[1 + \left(\frac{\tau_5}{\beta_k + \varepsilon_w} \right)^q \right], \quad k = 0, 1, 2 \quad (48)$$

The exponent $q \geq 1$ increases the rate of convergence to the ideal weights for smooth regions of the solution, and it accelerates the convergence rate to zero in the vicinity of discontinuities.

In practice, the question arises as to whether or not the ω_k are sufficiently good approximations of the ideal weights for smooth parts of the solution. The appropriate scaling of the smoothness

indicators β_k is essential to ensure that they do not dominate the parameter ε_w in smooth regions and produce weights that will result in too much numerical dissipation. This suggests that a given scaling of β_k can have an effect on the proper choice of ε_w . At the same time, caution must be exercised to make certain that the choice of ε_w does not compromise the non-oscillatory behavior of the WENO scheme. In numerical computations we have observed that if the parameter ε_w is too small relative to the smoothness measures defined by either Eq. (40) or Eq. (47), the WENO scheme will have too much numerical dissipation. Other difficulties can also occur when ε_w is not sufficiently large. Shen and Zha [57] found that when ε_w is too small (e.g., 10^{-6}) relative to β_k , convergence and stability problems can occur due to small disturbances in the β_k . These disturbances result in oscillations of the nonlinear weights which prevent convergence to the ideal (optimal) weights in smooth regions. Thus, there are increases in the numerical dissipation. Shen and Zha considered a seventh-order accurate scheme with the smoothness indicators of Borges et al. [55] and solved either the two-dimensional Euler or Navier-Stokes equations for subsonic and transonic steady flows. By setting $\varepsilon_w = 10^{-2}$, Shen and Zha prevented convergence stall and showed improved accuracy.

Oscillations in the weights are not only caused by flow discontinuities. As pointed out by Shen and Zha [58], strong variations in the smoothness measures β_k can occur due to nonuniformities in the computational mesh. If ε_w is very small (e.g., 10^{-6}), the β_k will not always be less than ε_w , even in smooth regions of the flow field. Here again, by increasing the magnitude of ε_w one can avoid oscillations in the nonlinear weights.

In the present work we apply the weights of Eq. (47). For comparison purposes we also consider the weights of Eq. (37). The influence of the parameter ε_w on accuracy is shown in the results section.

3.2.1c Flux Splitting

Throughout the previous discussion we have assumed that the flux Jacobian ($\partial f/\partial u$) is positive. In general, there is a need to allow for a sign change in the flux Jacobian. This is usually done by splitting the flux into positive and negative parts. In the present formulation for the WENO scheme a global Lax-Friedrichs splitting is used. Thus,

$$f^\pm(u) = \frac{1}{2}(f(u) \pm \alpha u) \quad (49)$$

where $\alpha = \max|\partial f/\partial u|$, and the maximum is taken over the complete solution field. A local splitting has also been considered. For the decay of turbulence problem considered herein, the local splitting did not have any significant effect on the results.

3.2.2 Approximating the Viscous Term

Here we discuss the approximation of the physical diffusion terms in the Navier-Stokes equations by considering the derivative of the viscous flux function $f^v(u_x)$ in Eq. (23). The derivative of the viscous flux function is defined by

$$\frac{df^v(x)}{dx} = \frac{d}{dx} \left[a(x) \frac{du(x)}{dx} \right] \quad (50)$$

where in general, the coefficient $a(x) = a[u(x), x]$. Since we want to construct a conservative difference scheme, this derivative is approximated by

$$\frac{df^v(x)}{dx} \approx \frac{f_{i+1/2}^v - f_{i-1/2}^v}{\Delta x} \quad (51)$$

Thus, one needs to determine the interface approximations of $a(x)$ and $u(x)$ at $x_{i+1/2}$ and $x_{i-1/2}$. With the fifth-order WENO scheme, the diffusion term is approximated with a conservative fourth-

order finite difference. When evaluating possible ways to determine these discrete interface functions, consideration must be given to not only accuracy and stability but also damping of all error modes. We now consider two ways to compute $a_{i\pm 1/2}$ and $u_{i\pm 1/2}$.

One possible method of discretizing the diffusion term is to first compute the discrete $f^v(x)$ at the solution points. A fourth-order approximation of $f^v(x)$ at x_i , an interior point of the domain, is given by

$$(f^v)_i = \frac{a_i}{12\Delta x} [u_{i-2} - 8u_{i-1} + 8u_{i+1} - u_{i+2}] \quad (52)$$

Then the approximation for the derivative of $f^v(x)$ is evaluated when constructing the approximation for the derivative of $f(x)$. For the fifth-order linear form of the WENO scheme (i.e., ideal weights) we obtain

$$\begin{aligned} \left. \frac{df^v}{dx} \right|_{x=x_i} &\approx \frac{1}{60\Delta x} [-2(f^v)_{i-3} + 15(f^v)_{i-2} - 60(f^v)_{i-1} + 20(f^v)_i \\ &\quad + 30(f^v)_{i+1} - 3(f^v)_{i+2}] \\ &= \frac{1}{720\Delta x^2} [-2a_{i-3}u_{i-5} + (16a_{i-3} + 15a_{i-2})u_{i-4} \\ &\quad - (120a_{i-2} + 60a_{i-1})u_{i-3} + (-16a_{i-3} + 480a_{i-1} + 20a_i)u_{i-2} \\ &\quad + (2a_{i-3} + 120a_{i-2} - 160a_i + 30a_{i+1})u_{i-1} \\ &\quad - (15a_{i-2} + 480a_{i-1} + 240a_{i+1} + 3a_{i+2})u_i \\ &\quad + (60a_{i-1} + 160a_i + 24a_{i+2})u_{i+1} + (-20a_i + 240a_{i+1})u_{i+2} \\ &\quad - (30a_{i+1} + 24a_{i+2})u_{i+3} + 3a_{i+2}u_{i+4}] \end{aligned} \quad (53)$$

If $a(x)$ and $u(x)$ are smooth functions, then the approximation of Eq. (53) is fourth-order accurate. While this method for differencing the derivative is convenient for implementation and operation count, it does have the undesirable consequence that the π -mode is not damped. One can easily show this by treating the discrete product of $a(x)$ and $u(x)$ as a single variable, Fourier transforming the derivative, and evaluating the transformed discrete operator at a Fourier angle equal to π .

An alternative method that provides a compact difference stencil and ensures damping of the π -mode is given by Kamakoti and Pantano [59]. This approximation enforces discrete conservation. Let B be a matrix of stencil coefficients for approximating the viscous term. Then, the flux form is given by

$$\left. \frac{df^v(x)}{dx} \right|_{x=x_i} \approx \frac{1}{\Delta x^2} \sum_{m=-p}^p \sum_{n=-p}^p B_{m+p+1, n+p+1} a_{i+m} u_{i+n} = \frac{f_{i+1/2}^v - f_{i-1/2}^v}{\Delta x} \quad (54)$$

where

$$f_{i+1/2}^v = \frac{1}{\Delta x} \sum_{m=-p+1}^p \sum_{n=-p+1}^p M_{m+p, n+p} a_{i+m} u_{i+n} \quad (55)$$

with M denoting the matrix of the unknown coefficients for the viscous flux to construct the difference stencil. The widths of the flux stencil and the stencil for the variable coefficient second-order derivative are $2p$ and $2p + 1$, respectively. One uses Taylor series expansions to determine the elements of the matrix M .

If we expand Eq. (55) for a fourth-order approximation, we obtain after rearranging terms

$$\begin{aligned} f_{i+1/2}^v = \frac{1}{\Delta x} &[(M_{11}a_{i-1} + M_{21}a_i + M_{31}a_{i+1} + M_{41}a_{i+2})u_{i-1} + \\ &(M_{12}a_{i-1} + M_{22}a_i + M_{32}a_{i+1} + M_{42}a_{i+2})u_i + \\ &(M_{13}a_{i-1} + M_{23}a_i + M_{33}a_{i+1} + M_{43}a_{i+2})u_{i+1} + \\ &(M_{14}a_{i-1} + M_{24}a_i + M_{34}a_{i+1} + M_{44}a_{i+2})u_{i+2}] \end{aligned} \quad (56)$$

The stencil matrix M is given by

$$M = \begin{bmatrix} \frac{1}{8} & -\frac{1}{6} & \frac{1}{24} & 0 \\ -\frac{1}{6} & -\frac{3}{8} & \frac{2}{3} & -\frac{1}{8} \\ \frac{1}{8} & -\frac{2}{3} & \frac{3}{8} & \frac{1}{6} \\ 0 & -\frac{1}{24} & \frac{1}{6} & -\frac{1}{8} \end{bmatrix} \quad (57)$$

The resulting approximation of Eq. (54) for the viscous term is compact, requiring just five points for fourth-order accuracy. Thus, it has a reduced error relative to the approximation of Eq. (53), and it has the advantage that the π -mode is damped.

The discretization method used to obtain Eq. (53) was employed in the original ENO (Essentially Non-oscillatory) code of Atkins [60] that was modified by Balakumar et al. [61] to create a WENO version. While the π -mode will be damped when there is deviation between the WENO weights and the ideal weights, this mode may not be adequately damped in regions where the diffusion terms dominate or the ideal weights are recovered. For this reason, along with reducing the truncation error and ensuring that this error is purely dissipative, the discretization method for Eq. (53) should be replaced by that for Eq. (54).

In this initial work we have retained the discretization method for the diffusion terms used by Atkins [60] and Balakumar et al. [61]. For the WENO scheme the polynomial that interpolates $f^v(x)$ at the solution points to the cell interfaces requires the smoothness indicators of Eq. (40) to determine the appropriate non-oscillatory stencil weights. We should mention that periodic boundary conditions are imposed for the isotropic turbulence problem considered in this paper. This is accomplished in the WENO code by introducing additional points outside the physical domain.

3.2.3 Higher Order Schemes

Higher order WENO schemes can be derived by following the steps presented in the first two subsections of Section 3.2.1 for the fifth-order scheme, starting with Eq. (29) and the appropriate r . For the seventh-order and ninth-order schemes the fluxes in the summation are fourth-order and fifth-order, respectively. Thus, each flux $\hat{f}_{i+1/2}^k$ for the seventh-order and ninth-order schemes is determined by third-degree and fourth-degree polynomials, respectively. The stencils for these schemes that define the corresponding WENO flux $\hat{f}_{i+1/2}$, the ideal weights d_k , and the smoothness indicators β_k are presented in the paper by Balsara and Shu [56]. For completeness, these quantities are included in Appendix A. It should be noted that the smoothness indicators in Appendix A include the scaling that arises when using Eq. (38), whereas those of Balsara and Shu do not. For extremely small values of the ε_w in Eq. (37) and Eq. (48) this does not matter. However, it does have an effect for larger values of ε_w such as 10^{-2} .

For the seventh-order and ninth-order schemes the $f^v(x)$ of the diffusion term is discretized at interior points with sixth-order and eighth-order central differences, respectively. Stencils for these approximations can be obtained using Table 2.1 of Shu [36], which is supplemented by Table A1 in Appendix A to include eighth-order. The sixth-order approximation is given by

$$(f^v)_i = \frac{a_i}{60\Delta x} (-u_{i-3} + 9u_{i-2} - 45u_{i-1} + 45u_{i+1} - 9u_{i+2} + u_{i+3}) \quad (58)$$

and the eighth-order one is given by

$$(f^v)_i = \frac{a_i}{840\Delta x} (3u_{i-4} - 32u_{i-3} + 168u_{i-2} - 672u_{i-1} + 672u_{i+1} - 168u_{i+2} + 32u_{i+3} - 3u_{i+4}) \quad (59)$$

The interpolating polynomials for obtaining the viscous fluxes at the cell interfaces are constructed with the fluxes and WENO weights given in Appendix A.

3.2.4 Time-Stepping Scheme

To advance the solution in time, a third-order Runge-Kutta (RK) scheme that satisfies the total variation diminishing (TVD) property is used. A scheme is said to be TVD if

$$TV(u^{n+1}) \leq TV(u^n), \quad TV = \sum_i |u_{i+1} - u_i| \quad (60)$$

The RK scheme has three stages given by

$$\begin{aligned} u^{(1)} &= u^n + \Delta t \mathcal{L} u^n, \\ u^{(2)} &= \frac{1}{4}(3u^n + u^{(1)} + \Delta t \mathcal{L} u^{(1)}), \end{aligned} \quad (61)$$

$$\begin{aligned} u^{(3)} &= \frac{1}{3}(u^n + 2u^{(2)} + 2\Delta t \mathcal{L} u^{(2)}), \\ u^{n+1} &= u^{(3)} \end{aligned} \quad (62)$$

where \mathcal{L} is the discrete spatial operator, and the superscript n denotes time level (time $t = n\Delta t$).

4 Numerical Results

4.1 Problem Definition

4.1.1 Decay of Isotropic Turbulence (DOIT)

In the classical problem of decay of isotropic turbulence, an initial turbulent field is allowed to decay in a “box-like” domain with periodicity imposed on all six of its sides. The turbulent statistics are collected and compared with experiments or with other numerical studies. Particular focus is often placed on the decay of the total turbulent kinetic energy with time, the initial growth followed by subsequent decay of the total turbulent dissipation with time, and the energy spectrum at given instants in time.

This classical problem is a good discriminator for SGS models and numerical schemes: poor models or overly-dissipative schemes tend to diffuse the energy-containing structures, and consequently miss many of the characteristic behaviors that can be accurately captured by well-resolved DNS. See, for example, the experimental results of Compte-Bellot and Corrsin [62], and the numerical studies of Clark et al. [63], Vreman et al. [64], Mansour and Wray [65], Spyropoulos and Blaisdell [66], Seror et al. [67], Hughes et al. [68], Hansen et al. [69], and Thornber et al. [42].

In the current study, the domain uses side lengths of 2π . Various Cartesian grid sizes are employed, ranging from the coarsest with 33^3 grid points (32^3 grid cells) to the finest with 193^3 grid points (192^3 grid cells).

To evaluate the numerical solutions to this problem, we use DNS results computed with a spectral scheme. Spectral solutions provide a good measure of accuracy due to their low discretization errors. They have the additional advantage of much faster convergence than finite-difference or finite-volume methods (i.e., exhibiting exponential rather than algebraic convergence with mesh refinement). These computations were performed with the same spectral computer code used to obtain the results presented in the paper by Zang et al. [70]. The conditions of the problem considered in the present work are for one of the cases included in the paper of Zang et al. In the DNS computer code, the spatial discretization is Fourier collocation with evenly spaced points in all coordinate directions. The code employs a time-step splitting technique that allows sound waves to be integrated exactly in time [71]. The other terms are advanced with a third-order Runge-Kutta explicit time-stepping scheme. An isotropic truncation is applied at the end of each Runge-Kutta stage. This ensures that only the resolvable modes (i.e., $|\kappa| \leq N/2$ where κ is the Fourier wavenumber vector) are nonzero. The semi-implicit scheme provides important computational advantages. For example,

at small fluctuating Mach numbers it can allow the use of time steps several times larger than those possible with a fully explicit scheme.

4.1.2 Initial Solution

The method for creating the initial turbulent flowfield condition is taken directly from Erlebacher et al. [71, 72], and is similar to a method introduced by Passot and Pouquet [73]. Random fields in physical space are generated for density, velocity, and temperature ($\bar{\rho}$, \tilde{u} , and \tilde{T}). Subsequently the velocity field is decomposed in Fourier space into incompressible and compressible components:

$$\tilde{u}_0(x) = \tilde{u}_0^I(x) + \tilde{u}_0^C(x) \quad (63)$$

The $\tilde{u}_0^C(x)$ has mean value of zero by construction, and $\tilde{u}_0^I(x)$ is divergence free. These components are transformed back to physical space and re-scaled in order to impose a prescribed autocorrelation spectrum. The spectrum

$$E(\kappa) = (\kappa + 1)^4 \exp\left(-2\frac{(\kappa + 1)^2}{\kappa_0^2}\right), \quad \kappa \geq 1 \quad (64)$$

is imposed on each of the variables $\bar{\rho}$, \tilde{u}_0^I , \tilde{u}_0^C , and \tilde{T} (for $\kappa = 0$ $E(\kappa) = 0$). Also, the initial value for the ratio of the compressible kinetic energy to the total kinetic energy, which is often called χ , is set to 0.2 (see Zang et al. [70]). Note that Eq. (64) is slightly different than that reported in Zang et al. [70]. The reference pressure is chosen (based on a reference density, $\bar{\rho}_{ref}$, and reference velocity, \tilde{U}_{ref}) to be $\bar{p}_{ref} = \bar{\rho}_{ref} \tilde{U}_{ref}^2$, so the initial nondimensional pressure is:

$$\bar{p} = \frac{\bar{\rho} \tilde{T}}{\gamma M_{ref}^2} \quad (65)$$

The reference Mach number

$$M_{ref} = \frac{\tilde{U}_{ref}}{\sqrt{\gamma R \tilde{T}_{ref}}} \quad (66)$$

is taken to be $M_{ref} = 0.2$ for all the current simulations. The Reynolds number, which is defined as $Re = (\bar{\rho}_{ref} \tilde{U}_{ref} L_{ref}) / \mu_{ref}$, is taken to be 250, and the Prandtl number and ratio of specific heats have the standard values of $Pr = 0.72$ and $\gamma = 1.4$, respectively. The reference length L_{ref} in this case is unity.

The Taylor microscale Reynolds number is defined by:

$$Re_\lambda = \frac{\langle \bar{\rho} \rangle}{\langle \mu \rangle} \lambda \tilde{U}_{rms} \quad (67)$$

where the angle brackets indicate an average over all cells in the domain, and

$$\lambda = \frac{1}{3} (\lambda_x + \lambda_y + \lambda_z) \quad (68)$$

$$\lambda_x = \sqrt{\frac{\langle \tilde{u}^2 \rangle}{\langle (\frac{\partial \tilde{u}}{\partial x})^2 \rangle}} \quad \lambda_y = \sqrt{\frac{\langle \tilde{v}^2 \rangle}{\langle (\frac{\partial \tilde{v}}{\partial y})^2 \rangle}} \quad \lambda_z = \sqrt{\frac{\langle \tilde{w}^2 \rangle}{\langle (\frac{\partial \tilde{w}}{\partial z})^2 \rangle}} \quad (69)$$

$$\tilde{U}_{rms} = \sqrt{\langle \tilde{u}^2 + \tilde{v}^2 + \tilde{w}^2 \rangle} \quad (70)$$

For all the cases herein, the initial Re_λ is approximately 125. The x -, y -, or z -direction Taylor microscale Reynolds numbers can also be found. For example, the x -direction Taylor microscale Reynolds number is defined by:

$$Re_{\lambda,x} = \frac{\langle \bar{\rho} \rangle}{\langle \mu \rangle} \lambda_x \sqrt{\langle \tilde{u}^2 \rangle} \quad (71)$$

The initial $Re_{\lambda,x} = Re_{\lambda,y} = Re_{\lambda,z} \approx 75$.

4.1.3 Turbulence Statistics

This section defines some of the turbulence statistics. The total turbulent kinetic energy is:

$$k = \frac{1}{2} \sum_{cells} (\tilde{u}^2 + \tilde{v}^2 + \tilde{w}^2) \quad (72)$$

The total turbulent dissipation is:

$$\varepsilon = 2 \frac{\langle \mu \rangle}{\langle \bar{\rho} \rangle} \sum_{cells} \bar{S}_{ij} \bar{S}_{ij} \quad (73)$$

The skewness factor of the velocity derivative, which supplies a measure of the nonlinear vortex stretching, is given by:

$$S_k = \frac{1}{3} \left[\frac{\langle (\frac{\partial \tilde{u}}{\partial x})^3 \rangle}{[\langle (\frac{\partial \tilde{u}}{\partial x})^2 \rangle]^{3/2}} + \frac{\langle (\frac{\partial \tilde{v}}{\partial y})^3 \rangle}{[\langle (\frac{\partial \tilde{v}}{\partial y})^2 \rangle]^{3/2}} + \frac{\langle (\frac{\partial \tilde{w}}{\partial z})^3 \rangle}{[\langle (\frac{\partial \tilde{w}}{\partial z})^2 \rangle]^{3/2}} \right] \quad (74)$$

Some discussion about the skewness factor and its relationship to the numerical scheme is given in Appendix B.

The enstrophy is defined by:

$$\text{enstrophy} = \frac{1}{2} \langle |\nabla \times u|^2 \rangle \quad (75)$$

The turbulence spectra is computed as follows. Given (at an instant in time) the velocities everywhere in the field, a 3-D fast Fourier transform (FFT) is performed on each velocity component. The energy $E'(k)$ within each energy ‘‘bin’’ is computed by summing over the squares of all the Fourier indices that contribute to that energy level. Then, the result is normalized via:

$$E(\kappa) = \left[E'(\kappa) / \int_0^\infty E'(\kappa) d\kappa \right] \quad (76)$$

4.2 Results with Upwinding and Central Differencing

Table 1 summarizes the computer runs performed using CFL3D. Both upwinding and central differencing methods were employed, and the effects of grid size, time step, and Smagorinsky filter constant c_s were explored. The time step, Δt^* , was nondimensionalized using $\Delta t^* = \Delta t U_{ref} / L_{ref}$, where U_{ref} and L_{ref} are the reference velocity scale and reference length scale, respectively. This time scale is a measure of ‘‘eddy turnover time’’ in terms of mean flow quantities. Most of the runs were performed at a nondimensional time step of $\Delta t^* = 0.002$. As can be seen in the table, one run was performed at a time step that was one fourth the nominal time step. Although not shown, results using the two different time steps were essentially identical, so the larger time step, $\Delta t^* = 0.002$, was deemed to be fine enough to accurately capture the temporal development with the current scheme in CFL3D.

4.2.1 Implicit LES (No Subgrid Model)

Results using CFL3D with the upwind-biased $\bar{\kappa} = 1/3$ scheme are shown in Figs. 3(a)–(c) for four different grid cell sizes. Note that the k and ε were normalized by their initial values. All cases except the 192^3 were carried out to total time of $t^* = 10$. The main point to be made is that on the coarsest grid (32^3) the upwind result is very poor, particularly in the fact that it shows no increase at all in ε for $0 < t^* < \approx 1.5$. As will be shown later, ε should increase to a level of nearly 2 (near $t^* = 1.3$) before dropping off. This rise in ε occurs during the energy redistribution phase of the

Table 1. Summary of CFL3D Cases

$\bar{\kappa}$	Grid size (# cells)	Δt^*	c_s
1/3 (upwind)	32^3	0.002	0
1/3 (upwind)	64^3	0.002	0
1/3 (upwind)	128^3	0.002	0
1/3 (upwind)	192^3	0.002	0
1 (central)	32^3	0.002	0
1 (central)	64^3	0.002	0
1 (central)	128^3	0.002	0
1 (central)	192^3	0.002	0
1 (central)	32^3	0.002	0.2
1 (central)	64^3	0.002	0.2
1 (central)	128^3	0.002	0.2
1 (central)	32^3	0.002	0.1
1 (central)	32^3	0.002	0.4
1 (central)	32^3	0.0005	0.2

simulation. The skewness using upwind with no model ends up between about -0.2 and -0.5 . For incompressible flows the experimental value for isotropic turbulence is around -0.4 (Lesieur [74]), and the DNS value at $Re_\lambda = 40$ is -0.5 (Erlebacher [71]).

Isocontours of vorticity are shown at $t^* = 5$ on three of the grids in Fig. 4. (Contours on the 192^3 grid are not shown; visually there are more small scale structures than for the 128^3 grid, as expected. The entire cube, 2π on a side, is shown here along with the subdivisions used for parallel processing.) However, in the literature, the so-called Q-invariant or Q-criterion is often preferred for visualizing LES results. See, for example, Piomelli et al. [75] and Slomski and Chang [76]. The Q variable is the second invariant of the velocity gradient tensor:

$$Q = \frac{1}{2} (\Omega_{ij}\Omega_{ij} - S_{ij}S_{ij}) = -\frac{1}{2} \left(\frac{\partial u_i}{\partial x_j} \frac{\partial u_j}{\partial x_i} \right) \quad (77)$$

The Q-invariant is useful because it tends to highlight the smaller-scale structures. Figure 5 shows the Q-invariant plotted for the upwind results. It is evident that using upwind on the 32^3 grid there is little eddy content, whereas on finer grids there are additional smaller scale structures present.

Results using CFL3D with second-order central differencing ($\bar{\kappa} = 1$) and no SGS model ($c_s = 0$) are shown in Figs. 6(a)–(c) for four different grid sizes. These results can be thought of as under-resolved DNS computations because there is no numerical or SGS model dissipation, and the grids are too coarse for a second-order finite-volume scheme to resolve down to the Kolmogorov dissipation length scale. Comparing Fig. 6(b) with Fig. 3(b), the central differencing yielded better results for temporal development of ε on a given grid size (the peak level was closer to the expected value of approximately 2). This improvement is to be expected because upwinding is inherently more dissipative. For example, using central differencing, the peak normalized ε reached nearly 1.4 on the 64^3 grid, which was almost as good as the upwind result on the 128^3 grid. However, note that the skewness tended to be smaller in magnitude using central differencing compared to upwind. The reason for this underprediction is not known.

Isocontours of the Q-invariant using central differencing are shown at $t^* = 5$ on three of the grids in Fig. 7. Comparing to Fig. 5, it is easy to see that central differencing yielded greater eddy content than upwind differencing on a given grid size.

Figure 8 shows energy spectra for eight different results at $t^* = 5$. The theoretical slope of $\kappa^{-5/3}$ from Kolmogorov theory (known as the Kolmogorov $-5/3$ law) is also indicated in the plot.

In the inertial subrange where the energy cascade transfers energy from large to small scales, the spectrum should follow this slope. However, very high Reynolds numbers are required in order to see evidence of the inertial subrange. The current Reynolds number of 250 is far too low for a region with constant slope to emerge. See Appendix C for additional discussion. Nonetheless, in this and subsequent plots of the energy spectrum, the $\kappa^{-5/3}$ line will continue to be shown to help provide a reference for the spectrum. In all cases shown in Fig. 8, results with central difference were better than for upwind (less rapid drop-off in energy with increasing κ). The greater decay in the upwind result is a consequence of the increased numerical dissipation with the upwind differencing, which results in greater smearing of the small scale structures associated with the higher wavenumbers. However, the finer the grid, the closer the central and upwind results were to each other. Figure 9 shows the progression of the energy spectrum with eddy turnover time for central differencing (no SGS model) on the 128^3 grid.

4.2.2 Explicit LES with Smagorinsky Model

Central differencing was also used in conjunction with the Smagorinsky model, using CFL3D. Figs. 10(a)–(c) show the statistical information over time. Generally, the higher c_s , the worse the result (on the 32^3 grid). The best result was achieved using no model at all ($c_s = 0$). This conclusion is also reflected in the spectrum results at $t^* = 5$, which is shown in Fig. 11. The higher the c_s coefficient, the more the energy dropped off at the higher wavenumbers.

On finer grids, the effect of c_s was not as great, as seen in Figs. 12(a)–(c) and Fig. 13. For example, on the 128^3 grid, the energy spectrum result using $c_s = 0.2$ is only slightly worse than the result with $c_s = 0$. Isocontours of the Q-invariant using central differencing with the Smagorinsky model and $c_s = 0.2$ are shown at $t^* = 5$ in Fig. 14.

Upwind was not run in conjunction with the Smagorinsky model ($c_s > 0$), because the combination would yield even more dissipative results than upwind ILES ($c_s = 0$).

4.3 Implicit LES Results with WENO and WENO-L

The focus in this section is on the effect of higher order accuracy on the turbulence statistics. Fifth-order, seventh-order, and ninth-order schemes are all considered. To ensure that the best possible results are obtained with the higher order approximations, we have switched off the nonlinear part of the WENO scheme for the initial set of computations. The linear scheme is designated WENO-L. In the second part of this section we investigate the nonlinear scheme, which is simply designated as WENO. The two ways of computing the nonlinear weights, ω_k , and smoothness measure, β_k , described in Section 3.2.1, are considered. In addition, the effect of the parameter ε_w is also evaluated and discussed. It is demonstrated by numerical testing that nearly the same solutions can be obtained with the nonlinear WENO scheme as for the WENO-L scheme if a sufficiently large value for ε_w in the non-oscillatory weights is chosen. For all high-order schemes the effect of mesh resolution on the computed solutions is examined. The grid density varied from 32^3 to 192^3 ; these are the same grids used for all results in the previous section. Results obtained with the WENO schemes are also compared with the second-order central ($c_s = 0$ and $c_s = 2$) and third-order upwind biased schemes. In addition, they are compared with those from the spectral scheme of Zang et al. [70]. For all simulations a $\Delta t^* = 0.002$ was used. Reducing the time step by a factor of four, which reduces temporal error by a factor of 64, produced essentially the same numerical results. All of the WENO and WENO-L calculations were performed without an explicit SGS model.

4.3.1 Linear WENO Scheme

Figures 15–17 show the turbulence quantities computed using the WENO-L scheme with different orders of spatial accuracy. Comparing the decay in the turbulent kinetic energy of the dissipative higher order schemes with that of the nondissipative central scheme, which was shown in Fig. 6(a),

Table 2. Normalized Dissipation Peak

Scheme	Order	Grid size (# cells)	Dissipation Peak
Central	2	32^3	1.10
Central	2	64^3	1.40
Central	2	128^3	1.64
Central	2	192^3	1.75
Upwind	3	32^3	1.00
Upwind	3	64^3	1.10
Upwind	3	128^3	1.46
Upwind	3	192^3	1.65
WENO-L	5	32^3	1.00
WENO-L	5	64^3	1.37
WENO-L	5	128^3	1.75
WENO-L	5	192^3	1.87
WENO-L	7	32^3	1.08
WENO-L	7	64^3	1.56
WENO-L	7	128^3	1.84
WENO-L	7	192^3	1.91
WENO-L	9	32^3	1.17
WENO-L	9	64^3	1.69
WENO-L	9	128^3	1.96
WENO-L	9	192^3	2.02

we observe that the dissipative schemes approach the solution on the 192^3 grid from below while the nondissipative scheme approaches from above, as expected. Moreover, it is evident that the fifth-order scheme is highly dissipative on the coarser meshes, especially on the 32^3 mesh. In (b) of Figs. 15–17, we see that the peak value of the normalized dissipation, which occurs during the energy redistribution phase of the simulation, increases both with grid refinement and with order of accuracy. The peak values for the different approximation orders and the range of mesh densities are given in Table 2, along with results from the earlier central ($c_s = 0$) and upwind computations. These results are also shown in Fig. 18. The largest energy dissipation (ε) peaks, obtained with the seventh-order and ninth-order schemes on mesh densities 128^3 and 192^3 , are roughly in the range of 1.8 to 2.0 and occur at $t^* \approx 1.30$. On the 128^3 grid, the peak value in ε is about 20% larger than the one computed with second-order central differencing. Like the third-order upwind biased scheme, the fifth-order WENO-L scheme does not exhibit any dissipation peak on the 32^3 grid, even though its dissipation is somewhat smaller (as seen by comparing the turbulent kinetic energy levels in Figs. 3(a) and 15(a)). Even the seventh-order scheme only has a very small peak on this grid, and this peak is about the same size as that for the central difference scheme. The peak in dissipation for the fifth-order scheme exceeds 1.8 on the 192^3 grid, whereas for the seventh-order and ninth-order schemes it is greater than 1.8 on the 128^3 grid. These results indicate that the resolution on the 32^3 grid is not adequate for any of the schemes. The numerical viscosity is not sufficiently small on such a coarse grid.

We now consider the skewness factor (S_k) plots in Figs. 15–17. On the finest mesh the quasi-equilibrium value is between -0.5 and -0.6 for the different approximation orders of the WENO-L scheme. It is nearly -0.6 using the ninth-order scheme on the 192^3 grid. This is about the same S_k

obtained with the third-order upwind biased scheme on the finest mesh.

In Fig. 19, the energy spectra are shown for computations with different orders of accuracy and grid sizes. The fifth-order results are comparable to those obtained with the third-order upwind biased scheme, although the fifth-order results are more dissipative at the highest frequencies. In comparing the spectra for the higher order schemes with the fifth-order scheme, we observe roughly an order of magnitude less drop in the energy decay at the the cut-off wavenumber ($N/2$, where N is the number of mesh points), reflecting the reduced dissipation of the small scales. Figure 20 clearly shows how the high-frequency content improves with increasing mesh density for the ninth-order scheme. In Fig. 21, we see that the spectra obtained on the 128^3 grid with the ninth-order WENO and the second-order central ($c_s = 0$) schemes are nearly the same. The fifth-order WENO and third-order upwind spectra are also similar to each other

Figure 22 displays the isocontours of the nondimensional Q-invariant for the ninth-order WENO-L scheme computations for various grid sizes. Comparing with the corresponding contours obtained with second-order central differencing ($c_s = 0$) in Fig. 7, we note that in these plots the two schemes appear to have similar eddy content on the 128^3 grid. However, comparing with the explicit LES scheme with central differencing and $c_s = 0.2$ (see Fig. 14), we observe that there is a significant increase in the eddy content for ninth-order over the range of meshes.

4.3.2 Nonlinear WENO Scheme

Appropriate determination of the nonlinear weights is essential since these weights allow non-oscillatory shock capturing and determine the rate at which the nonlinear WENO scheme returns to a linear form. We first evaluate the two methods for computing the nonlinear weights, ω_k , and smoothness measures, β_k . Figure 23 compares the two methods discussed in Section 3.2.1. In the figure, α_1 refers to the method of Jiang and Shu (Eqs. (37) and (38)), and α_2 refers to the method of Borges et al., Eq. (48)). For each method, two values of ε_w , the parameter for ensuring that β_k is bounded, are considered. The computational results are for the fifth-order and seventh-order schemes on the 128^3 grid. We observe in the figure a slight improvement in the prediction of the peak value of ε with the method of Borges et al. (α_2). For the larger $\varepsilon_w = 10^{-2}$, the energy spectrum shows that the WENO scheme is dissipative at the highest frequencies, whereas there is some energy buildup at the highest frequencies for the smaller $\varepsilon_w = 10^{-6}$. This behavior is most prominent for the fifth-order scheme.

In Fig. 24, the method of Borges et al. is considered, and the effect of varying ε_w on the turbulence statistics using a 64^3 grid is shown. The WENO and WENO-L results are nearly the same when $\varepsilon_w = 10^{-1}$. However, such a large value could easily adversely affect the nonlinear behavior (i.e., shock capturing properties) of the WENO scheme. Shen and Zha [57, 58] have demonstrated for transonic fluid dynamics problems with shock waves that a value of $\varepsilon_w = 10^{-2}$ is satisfactory. It still remains, however, to show that this value of ε_w is suitable for a wide range of flow problems with various levels of complexities and Mach numbers. To reduce the possibility of energy buildup at the highest frequencies that can result in instability, the method of Borges et al. with $\varepsilon_w = 10^{-2}$ will be used for all subsequent results.

Figure 25 compares the dissipation computed with the WENO-L and WENO schemes for different grids and orders of discrete approximation. In general, the linear and nonlinear results are quite close, with the greatest difference occurring on the coarsest (32^3) grid. A similar comparison is shown in Fig. 26 for the energy spectrum. There is no discernible difference between the linear and nonlinear results.

We now consider how the ninth-order WENO scheme compares with other previously presented LES schemes. Figure 27 displays the turbulence statistics for the ninth-order WENO ILES scheme, second-order central scheme with the Smagorinsky SGS model ($c_s = 0.2$), and the third-order upwind biased ILES scheme. Results are given for the 64^3 and 128^3 grids. The largest differences in the turbulent kinetic energy (k) decay for the two grids occur with the upwind scheme. With the WENO scheme the k decay for the 64^3 grid closely tracks that for the 128^3 grid. When comparing

the dissipation (ε) peaks, we see that the peak on the 128^3 grid with WENO scheme is significantly larger than the peaks for the lower-order LES schemes. Furthermore, the ε peak on the 64^3 grid with the WENO scheme is approximately 8% and 15% higher than the peaks on the 128^3 grid with the central and upwind schemes, respectively. These results indicate that more than an order of magnitude increase in the grid density would be required to produce similar ε peaks with the lower order LES schemes. In Fig. 27(c) a comparison of the LES schemes is given for the energy spectrum at $t^* = 5$. The WENO result for the 64^3 grid follows the fine grid energy spectrum until between $\kappa = 15$ and $\kappa = 20$, where it begins to show a more rapid decrease in the energy with increasing κ . As expected, the lower order LES schemes exhibit a much earlier departure (roughly $\kappa = 5$) from the fine grid result with WENO.

A comparison of the turbulence statistics at $t^* = 2$ for the ninth-order WENO ILES scheme, second-order central scheme ($c_s = 0$), and a spectral scheme is presented in Fig. 28. In the absence of numerical dissipation (either through discretization or filtering) and an explicit SGS model, the central scheme relies on the dissipative effect of the physical viscous terms for stability. Thus, the computation with the central scheme is essentially an under-resolved DNS. One could view this solution as representing a bound on the best possible result with a second-order scheme for an explicit SGS model (i.e., in the limit as $c_s \rightarrow 0$). The results for the spectral scheme are from DNS computations with the computer code of Zang et al. [70]. In Fig. 28a, we observe a similar decay rate of the turbulent kinetic energy for all schemes. Figure 28(b) shows that the peak dissipation for the ninth-order WENO scheme on the 192^3 grid is approximately 4% high compared with the DNS, whereas the second-order central scheme is approximately 10% low. Although not shown, a simulation on a 384^3 grid was performed to determine if there is any further increase in the peak dissipation with the WENO scheme. Essentially the same peak value was obtained on the finer grid. In Fig. 28c, we observe fairly good agreement between the energy spectra computed with the WENO and spectral schemes, except at the highest frequencies where the WENO scheme exhibits a faster decay in κ due to dissipative effects. There is also some difference at the lowest frequencies. The source of this difference appeared to be a consequence of variations in the methods used for the two schemes to determine the spectrum from the simulation data. The second-order central scheme on the 192^3 grid exhibits less energy content at the highest wave numbers than the ninth-order WENO scheme, and thus, has poorer agreement with the DNS spectrum.

The computational cost of the WENO scheme with increasing approximation order is especially important due to the high operation count of the scheme. A comparison of the results for the ninth-order and fifth-order schemes indicates that the ninth-order scheme requires half as many grid points in each coordinate direction as the fifth-order scheme to obtain comparable resolution. We compared the computational (CPU) times of these schemes for the isotropic turbulence decay simulation using the 64^3 grid for the ninth-order scheme and the 128^3 grid for the fifth-order scheme. All of the simulations were performed with parallel processing. To have approximately the same parallel efficiency for both schemes, we used more processors for the fifth-order scheme on the 128^3 grid than for the ninth-order scheme on the 64^3 grid (i.e., 64 and 16 processors, respectively). This comparison showed that the ninth-order scheme required about 17% less computing time than the fifth-order scheme for comparable resolution. We should point out that Shi et al. [77] showed that for problems with discontinuities and complex solution structures (e.g., double Mach reflection and Rayleigh-Taylor instability problems) that a ninth-order WENO scheme required half as many mesh points in each coordinate direction to obtain comparable resolution (i.e., similar numerical viscosity) as the fifth-order scheme. Furthermore, they showed that with parallel processing that the ninth-order scheme could reduce the CPU time between 66% and 80% with their implementation of the WENO scheme. Their results suggest that it may be possible to significantly improve the present implementation of the WENO scheme, especially since no attempt was made to optimize it. In addition, their results emphasize the capability of the high-order WENO schemes to capture small scale structures of complicated flows that would require much finer grids with lower order schemes. This is especially important in the simulation of turbulence.

4.3.3 Future Work: Improved WENO Scheme

As we have seen in the previous section, the conventional fifth-order WENO scheme of Shu [36] with either the weights of Jiang and Shu [53] or Borges et al. [55] is too dissipative. In addition, there is no energy stability proof (guaranteeing all eigenvalues lie in the left half of the complex plane) for the conventional WENO scheme. To improve this situation Yamaleev and Carpenter [78] – [80] have introduced energy stable modifications for existing WENO schemes. Such modified schemes are called energy stable WENO (ESWENO) schemes. By modifying the nonlinear weights of the conventional WENO schemes, Yamaleev and Carpenter achieved a reduction of the nonlinear dissipation in the neighborhood of discontinuities, while retaining an energy stability of the spatial discretization. With their systematic methodology (see [78] and [80]) they have constructed ESWENO schemes for both upwind biased and centered finite differences. Thus, stable higher order central difference schemes can be used in smooth regions of the flow field, eliminating the dissipation in these regions.

An essential constraint in minimizing numerical errors produced by dissipation is to enhance the stability of the spatial discretization. For a given order of approximation, one approach that can lead to not only reduction of numerical dissipation but also minimization of aliasing error is to use a skew-symmetric form of the convective operator (e.g., see Kravchenko and Moin [81]). This form of the convective operator is defined by a linear combination of the conservative (divergence) and non-conservative operators using a central difference discretization. Such a discrete operator is conservative (i.e., can be expressed in terms of telescopic fluxes), and in the absence of external forces and dissipation, it produces a kinetic-energy preserving scheme. With kinetic energy conservation, one can show that the scheme is energy stable, which means that without dissipation the energy of the discrete system cannot increase (with dissipation the energy decreases). Moreover, in conserving kinetic energy there is no spurious production or dissipation of kinetic energy due to the discretization of the nonlinear convection. Some examples of papers with schemes based on a skew-symmetric operator are those by Lilly [82], Ducros et al. [83], Verstappen and Veldman [84], Feiereisen et al. [85], and Kok [86].

While the ESWENO formulation and alternative convective operators can significantly reduce numerical dissipation, and thus, improve the representation of the entire energy spectrum, the dispersion errors still need to be controlled. As Ghosal [87] has demonstrated, even a centered scheme with eighth-order accuracy requires some technique such as prefiltering to effectively remove such errors so that the modeling errors dominate. One possible approach for minimizing the numerical dispersion errors at high wavenumbers is to construct a central difference approximation with the dispersion-relation preserving (DRP) scheme of Tam and Webb [88]. The DRP scheme uses a larger stencil than necessary for a given order of approximation to create an additional degree of freedom to allow minimization of dispersion.

In future work, we plan to consider both an ESWENO scheme and the skew-symmetric form of the convective operator. For the viscous terms we will replace the current discretization with the compact approximation of Kamakoti and Pantano [59], which ensures damping of the π -mode. We will also consider minimization of dispersion error.

5 Concluding Remarks

Numerical simulations of decaying homogeneous isotropic turbulence have been performed with both low-order and high-order spatial discretization schemes. Second-order central and third-order upwind biased differencing have been used for the low-order schemes. The WENO framework has been applied to obtain fifth-order, seventh-order, and ninth-order discretizations. Large eddy simulation results have been presented for the various schemes on four grids, ranging from 32^3 to 192^3 . Turbulence statistics, such as kinetic energy, dissipation, and skewness, along with the energy spectra from simulations of the decaying turbulence problem have been used to examine and

compare the schemes.

Through the simulation results for the fifth-order WENO scheme and the second-order central scheme, with or without the Smagorinsky SGS model ($c_s \leq 0.2$), we have shown that the fifth-order WENO is too dissipative on the coarsest grid considered (32^3). While the fifth-order WENO was still too dissipative on the 64^3 grid when compared with the central scheme without a SGS model, this was not the case when compared with the central scheme with a SGS model and $c_s \geq 0.2$. On the coarser grids, the fifth-order WENO scheme was somewhat less dissipative than the third-order upwind biased scheme. Comparisons of the fifth-order WENO scheme with the lower order LES schemes have indicated that the fifth-order WENO has reasonable levels of dissipation on the finer grids (128^3 and 192^3).

With the seventh-order and ninth-order WENO schemes, we have observed a significant improvement in accuracy relative to the lower order schemes, as revealed by the computed peak in the energy dissipation variation with eddy turnover time. The ninth-order WENO scheme has shown the best overall results when comparing with the other LES schemes (i.e., second-order central scheme with Smagorinsky SGS model and third-order upwind biased scheme). Moreover, it was indicated (comparing results from 64^3 and 128^3 grids) that the other LES schemes would require more than an order of magnitude increase in mesh density to produce a similar dissipation peak to that obtained with the ninth-order WENO Scheme. The ninth-order WENO scheme, which is an ILES scheme, has also been compared with a spectral scheme for DNS. Similar results were obtained for the turbulent kinetic energy and turbulent dissipation. Generally, the energy spectrum of the WENO scheme closely tracked that of the DNS spectral scheme, except at the highest frequencies, where the WENO scheme exhibited some numerical dissipation effects.

The computational cost of the WENO scheme is high. However, current simulation results have provided indications that for the ninth-order scheme this additional cost relative to conventional lower order LES schemes (such as those based on central differencing with the Smagorinsky model and third-order upwind biased differencing) as well as fifth-order WENO is compensated by improved resolution. In addition, as revealed by Shi et al. [77], the ninth-order WENO scheme has the additional advantage of capturing small scale structures of complex flows that can include shock waves with significantly coarser meshes than required by much lower order schemes.

Although we have observed improved accuracy with the upwind biased higher order schemes, there is still a need to reduce the numerical dissipation, as revealed by the computed energy spectra. Recent developments for WENO schemes such as ESWENO suggest that this can be done while retaining appropriate shock capturing capability. In addition, these schemes could possibly be designed so that they have low dispersion errors and preserve properties such as kinetic energy. Such schemes would then have sufficiently low numerical errors that the dominant errors in a simulation would be due to modeling, allowing a better understanding of SGS modeling effects that can lead to improved LES results.

References

1. Piomelli, U., “Large Eddy and Direct Simulation of Turbulent Flows,” von Kàrmàn Institute for Fluid Dynamics Lecture Series, *Introduction to Turbulence Modeling*, March 22–26, 2004.
2. Smagorinsky, J., “General Circulation Experiments with the Primitive Equations,” *Monthly Weather Review*, Vol. 91, No. 3, 1963, pp. 99–164.
3. Germano, M., Piomelli, U., Moin, P., and Cabot, W. H., “A Dynamic Subgrid-Scale Eddy-Viscosity Model,” *Physics of Fluids A*, Vol. 3, No. 7, 1991, pp. 1760–1765.
4. Bardina, J., Ferziger, J. H., and Reynolds, W. C., “Improved Subgrid Scale Models for Large Eddy Simulations,” AIAA Paper 80-1357, Jan. 1980.
5. Deardorff, J. W., “The Use of Subgrid Transport Equations in a Three-Dimensional Model of Atmospheric Turbulence,” *Journal of Fluids Engineering Transactions*, Vol. 95, 1973, pp. 429–438.
6. Adams, N. A. and Stolz, S., “Deconvolution Methods for Subgrid Scale Approximation in LES,” *Modern Simulation Strategies for Turbulent Flow*, editor: B. J. Geurts, R. T. Edwards, Inc., Philadelphia, 2001, pp. 21–44.
7. Stolz, S. and Adams, N. A., “On the Approximate Deconvolution Procedure for LES,” *Physics of Fluids*, Vol. 11, 1999, pp. 1699–1701.
8. Grinstein, F. F. and Fureby, C., “Recent Progress on Flux-Limiting Based Implicit Large Eddy Simulation,” *European Conference on Computational Fluid Dynamics (ECCOMAS CFD) 2006*, editors: P. Wesseling, E. Oñate, J. Pèriaux, TU Delft, Delft The Netherlands, 2006.
9. Sagaut, P., *Large Eddy Simulation for Incompressible Flows*, Third Edition, Springer, Berlin, 2006.
10. Richtmyer, R. D. and Morton, K. W., *Difference Methods for Initial Value Problems*, John Wiley & Sons, 1967.
11. Boris, J. P., “On Large Eddy Simulation Using Subgrid Turbulence Models,” *Whither Turbulence? Turbulence at the Crossroads*, Ed.: J. L. Lumley, New York: Springer-Verlag, 1990, pp. 344–353.
12. Boris, J. P., “A Fluid Transport Algorithm that Works,” *Computing as a Language of Physics*, Vienna: International Atomic Energy Agency, 1971, pp. 171–189.
13. Boris, J. P. and Book, D. L. “Flux-Corrected Transport I: SHASTA – A Fluid Transport Algorithm that Works,” *Journal of Computational Physics*, Vol. 11, 1973, pp. 38–69.
14. Boris, J. P., Book, D. L., and Hain, K. “Flux-Corrected Transport II: Generalizations of the Method,” *Journal of Computational Physics*, Vol. 18, 1975, pp. 248–283.
15. Boris, J. P. and Book, D. L. “Flux-Corrected Transport III: Minimal-Error FCT Algorithms,” *Journal of Computational Physics*, Vol. 20, 1976, pp. 397–431.
16. Grinstein, F. F., Margolin, L. G., and Rider, W. J. (editors), *Implicit Large Eddy Simulation*, Cambridge University Press, 2007.
17. van Leer, B. “Towards the Ultimate Conservative Difference Scheme. I. The Quest of Monotonicity,” *Lecture Notes in Physics*, Vol. 18, editors: E. Cabannes and R. Temam, Springer-Verlag, 1973, pp. 163–168.

18. van Leer, B. "Towards the Ultimate Conservative Difference Scheme II. Monotonicity and Conservation Combined in a Second-Order Scheme," *Journal of Computational Physics*, Vol. 14, 1974, pp. 361–370.
19. van Leer, B. "Towards the Ultimate Conservative Difference Scheme III. Upstream-Centered Finite-Difference Schemes for Ideal Compressible Flow," *Journal of Computational Physics*, Vol. 23, 1977, pp. 263–275.
20. van Leer, B. "Towards the Ultimate Conservative Difference Scheme IV. A New Approach to Numerical Convection," *Journal of Computational Physics*, Vol. 23, 1977, pp. 276–299.
21. van Leer, B. "Towards the Ultimate Conservative Difference Scheme V. A Second-Order Sequel to Godunov's Method," *Journal of Computational Physics*, Vol. 32, 1979, pp. 101–136.
22. Colella, P. and Woodward, P. R., "The Piecewise Parabolic Method (PPM) for Gas-Dynamical Simulations," *Journal of Computational Physics*, Vol. 54, 1984, pp. 174–201.
23. Woodward, P. R. and Colella, P., "Numerical Simulation of Two-Dimensional Fluid Flow with Strong Shocks," *Journal of Computational Physics*, Vol. 54, 1984, pp. 115–173.
24. Harten, A., "High Resolution Schemes for Hyperbolic Conservation Laws," *Journal of Computational Physics*, Vol. 49, 1983, pp. 357–393.
25. Harten, A., Engquist, B., Osher, S., and Chakravarthy, S., "Uniformly High-Order Accurate Essentially Non-oscillatory Schemes, III," *Journal of Computational Physics*, Vol. 71, 1987, pp. 231–303.
26. Sweby, P. K., "High-Resolution Schemes Using Flux Limiters for Hyperbolic Conservation Laws," *SIAM Journal of Numerical Analysis*, Vol. 21, 1984, pp. 995–1011.
27. Yee, H., Warming, R. F., and Harten, A., "Implicit Total Variation Diminishing (TVD) Schemes for Steady-State Calculations," *Journal of Computational Physics*, Vol. 57, 1985, pp. 327–360.
28. Colella, P., "A Direct Eulerian MUSCL Scheme for Gas Dynamics," *SIAM Journal of Scientific Statistical Computing*, Vol. 6, 1985, pp. 104–117.
29. Colella, P. and Glaz, H. M., "Efficient Solution Algorithms for the Riemann Problems for Real Gases," *Journal of Computational Physics*, Vol. 59, 1985, pp. 264–289.
30. Lax, P. and Wendroff, B., "Systems of Conservation Laws," *Communications on Pure and Applied Mathematics*, Vol. 13, 1960, pp. 217–237.
31. Godunov, S. K., "A Finite-Difference Method for the Numerical Computation and Discontinuous Solutions of the Equations of Fluid Dynamics," *Matematicheskii Sbornik*, Vol. 47, 1959, pp. 271–306.
32. Harten, A., Hyman, J. M., and Lax, P. D. (with Appendix by B. Keyfitz), "On Finite-Difference Approximations and Entropy Conditions for Shocks," *Communications on Pure and Applied Mathematics*, Vol. 29, 1976, pp. 297–322.
33. Jameson, A., "Analysis and Design of Numerical Schemes for Gas Dynamics 1: Artificial Diffusion, Upwind Biasing, Limiters and Their Effect on Accuracy and Multigrid Convergence," *International Journal of Computational Fluid Dynamics*, Vol. 4, 1995, pp. 171–218.
34. Jameson, A., "Analysis and Design of Numerical Schemes for Gas Dynamics 2: Artificial Diffusion and Discrete Shock Structure," *International Journal of Computational Fluid Dynamics*, Vol. 5, 1995, pp. 1–38.

35. Yee, H. C. and Sjögren, B., “Development of Low Dissipative High Order Filter Schemes for Multiscale Navier-Stokes/MHD Systems,” *Journal of Computational Physics*, Vol. 225, 2007, pp. 910–934.
36. Shu, C.-W., “Essentially Non-oscillatory and Weighted Essentially Non-oscillatory Schemes for Hyperbolic Conservation Laws,” Institute for Computer Applications in Science and Engineering (ICASE) Report No. 97-65 (NASA/CR-97-206253), Nov. 1997.
37. Hill, D. J. and Pullin, D. I., “Hybrid Tuned Center-Difference-WENO Method for Large Eddy Simulations in the Presence of Strong Shocks,” *Journal of Computational Physics*, Vol. 194, 2004, pp. 435–450.
38. Costa, B. and Don, W. S., “Multi-domain Hybrid Spectral-WENO Methods for Hyperbolic Conservation Laws,” *Journal of Computational Physics*, Vol. 224, 2007, pp. 970–991.
39. Visbal, M. R. and Rizzeta, D. P., “Large-Eddy Simulation on Curvilinear Grids Using Compact Differencing and Filtering Schemes,” *Journal of Fluids Engineering*, Vol. 124, 2002, pp. 836–847.
40. Visbal, M. R. and Gaitonde, D. V., “Shock Capturing Using Compact-Differencing-Based Methods,” AIAA Paper 2005-1265, Jan. 2005.
41. Garnier, E., Mossi, M., Saugaut, P., Comte, P., and Deville, M., “On the Use of Shock-Capturing Schemes for Large-Eddy Simulation,” *Journal of Computational Physics*, Vol. 153, 1999, pp. 273–311.
42. Thornber, B., Mosedale, A., and Drikakis, D., “On the Implicit Large Eddy Simulations of Homogeneous Decaying Turbulence,” *Journal of Computational Physics*, Vol. 226, 2007, pp. 1902–1929.
43. Martin, M. P., Taylor, E. M., Wu, M., and Weirs, V. G., “A Bandwidth-Optimized WENO Scheme for the Effective Direct Numerical Simulation of Compressible Turbulence,” *Journal of Computational Physics*, Vol. 220, 2006, pp. 270–289.
44. Taylor, E. M. and Martin, M. P., “Stencil Adaptation Properties of a WENO Scheme in Direct Numerical Simulations of Compressible Turbulence,” *Journal of Scientific Computing*, Vol. 30, No. 3, 2007, pp. 533–554.
45. Ishihara, T., Gotoh, T., and Kaneda, Y., “Study of High-Reynolds Number Isotropic Turbulence by Direct Numerical Simulation,” *Annual Review of Fluid Mechanics*, Vol. 41, 2009, pp. 165–180.
46. Gaitonde, D., Shang, J., and Young, J., “Practical Aspects of Higher-Order Numerical Schemes for Wave Propagation Phenomena,” *International Journal for Numerical Methods in Engineering*, Vol. 45, 1999, pp. 1849–1869.
47. Knight, D., Yan, H., and Zheltovodov, A., “Large Eddy Simulation of Supersonic Turbulent Flow in Expansion-Compression Corner,” *DNS/LES - Progress and Challenges, Proceedings of the Third AFOSR International Conference on DNS/LES*, edited by C. Liu, L. Sakell, and T. Beutner, Greyden Press, Columbus, 2001, pp. 183–194.
48. Urbin, G. and Knight, D., “Large-Eddy Simulation of a Supersonic Boundary Layer Using an Unstructured Grid,” *AIAA Journal*, Vol. 39, No. 7, 2001, pp. 1288–1295.
49. Krist, S. L., Biedron, R. T., and Rumsey, C. L., “CFL3D User’s Manual (Version 5.0),” NASA TM-1998-208444, June 1998.

50. Anderson, W. K., Thomas, J. L., and van Leer, B., "Comparison of Finite Volume Flux Vector Splittings for the Euler Equations," *AIAA Journal*, Vol. 24, No. 9, 1986, pp. 1453–1460.
51. Roe, P. L., "Approximate Riemann Solvers, Parameter Vectors, and Difference Schemes," *Journal of Computational Physics*, Vol. 43, 1981, pp. 357–372.
52. Koren, B., "Upwind Schemes for the Navier-Stokes Equations," *Proceedings of the Second International Conference on Hyperbolic Problems*, Aachen. Vieweg: Braunschweig, 1988.
53. Jiang, G. S. and Shu, C.-W., "Efficient Implementation of Weighted ENO Schemes," *Journal of Computational Physics*, Vol. 126, 1996, pp. 202–228.
54. Henrick, A. K., Aslam, T. D., and Powers, J. M., "Mapped Weighted Essentially Non-oscillatory Schemes: Achieving Optimal Order near Critical Points," *Journal of Computational Physics*, Vol. 207, 2005, pp. 542–567.
55. Borges, R., Carmona, M., Costa, B., and Don, W. S., "An Improved Weighted Essentially Non-oscillatory Scheme for Hyperbolic Conservation Laws," *Journal of Computational Physics*, Vol. 227, 2008, pp. 3191–3211.
56. Balsara, D. S. and Shu, C.-W., "Monotonicity Preserving Weighted Essentially Non-oscillatory Schemes with Increasingly High Order of Accuracy," *Journal of Computational Physics*, Vol. 160, 2000, pp. 405–452.
57. Shen, Y. and Zha, G., "Improved Seventh-order WENO Scheme," AIAA Paper 2010-1451, Jan. 2010.
58. Shen, Y. and Zha, G., "Improvement of Stability and Accuracy for Weighted Essentially Nonoscillatory Scheme," *AIAA Journal*, Vol. 47, No. 2, 2009, pp. 331–344.
59. Kamakoti, R. and Pantano, C., "High-Order Narrow Stencil Finite-Difference Approximations of Second-Order Derivatives Involving Variable Coefficients," *SIAM Journal of Scientific Computing*, Vol. 31, No. 6, 2009, pp. 4222–4243.
60. Atkins, H. L., "High-Order ENO Methods for the Unsteady Compressible Navier-Stokes Equations," AIAA Paper 1991-1557, June 1991.
61. Balakumar, P., Zhao, H., and Atkins, H., "Stability of Hypersonic Boundary Layers over a Compression Corner," AIAA Paper 2002-2848, June 2002.
62. Compte-Bellot, G. and Corrsin, S., "Simple Eulerian Time Correlation of Full- and Narrow-Band Velocity Signals in Grid-Generated, Isotropic Turbulence," *Journal of Fluid Mechanics*, Vol. 48, Part 2, 1971, pp. 273–337.
63. Clark, R. A., Ferziger, J. H., and Reynolds, W. C., "Evaluation of Subgrid-Scale Models Using an Accurately Simulated Turbulent Flow," *Journal of Fluid Mechanics*, Vol. 91, Part 1, 1979, pp. 1–16.
64. Vreman, A. W., Geurts, B. J., Kuerten, J. G. M., and Zandbergen, P. J., "A Finite Volume Approach to Large Eddy Simulation of Compressible, Homogeneous, Isotropic, Decaying Turbulence," *International Journal for Numerical Methods in Fluids*, Vol. 15, 1992, pp. 799–816.
65. Mansour, N. N. and Wray, A. A., "Decay of Isotropic Turbulence at Low Reynolds Number," *Physics of Fluids*, Vol. 6, No. 2, 1994, pp. 808–814.
66. Spyropoulos, E. T. and Blaisdell, G. A., "Evaluation of the Dynamic Model for Simulations of Compressible Decaying Isotropic Turbulence," *AIAA Journal*, Vol. 34, No. 5, 1996, pp. 990–998.

67. Seror, C., Sagaut, P., Bailly, C., and Juve, D., "Subgrid-Scale Contribution to Noise Production in Decaying Isotropic Turbulence," *AIAA Journal*, Vol. 38, No. 10, 2000, pp. 1795–1803.
68. Hughes, T. J. R., Mazzei, L., and Oberai, A. A., "The Multiscale Formulation of Large Eddy Simulation: Decay of Homogeneous Isotropic Turbulence," *Physics of Fluids*, Vol. 13, No. 2, 2001, pp. 505–512.
69. Hansen, A., Sorensen, N. N., Johansen, J., and Michelsen, J. A., "Detached-Eddy Simulation of Decaying Homogeneous Isotropic Turbulence," AIAA Paper 2005-885, Jan. 2005.
70. Zang, T. A., Dahlburg, R. B., and Dahlburg, J. P., "Direct and Large-Eddy Simulations of Three-Dimensional Compressible Navier-Stokes Turbulence," *Physics of Fluids A*, Vol. 4, No. 1, 1992, pp. 127–140.
71. Erlebacher, G., Hussaini, M. Y., Speziale, C. G., and Zang, T. A., "Toward the Large-eddy Simulation of Compressible Turbulent Flows," *Journal of Fluid Mechanics*, Vol. 238, 1992, pp. 155–185.
72. Erlebacher, G., Hussaini, M. Y., Kreiss, H. O., and Sarkar, S., "The Analysis and Simulation of Compressible Turbulence," *Theoretical Computational Fluid Dynamics*, Vol. 2, 1990, pp. 73–95.
73. Passot, T. and Pouquet, A., "Numerical Simulation of Compressible Homogeneous Flows in the Turbulent Regime," *Journal of Fluid Mechanics*, Vol. 181, 1987, pp. 441–466.
74. Lesieur, M., *Turbulence in Fluids*, 2nd ed., Kluwer Academic, Norwell, MA, 1990.
75. Piomelli, U., Radhakrishnan, S., and de Prisco, G., "Turbulent Eddies in the RANS/LES Transition Region," in *Advances in Hybrid RANS-LES Modeling*, editors: S.-H. Peng and W. Haase, Springer, Berlin, 2008, pp. 21–36.
76. Slomski, J. F. and Chang, P. A., "Synthesis and Advection of Isotropic Turbulence to a Target Intensity and Spectrum," AIAA Paper 2008-547, Jan. 2008.
77. Shi, J., Zhang, Y.-T., and Shu, C.-W., "Resolution of High Order WENO schemes for complicated flow structures," *Journal of Computational Physics*, Vol. 186, 2003, pp. 690–696.
78. Yamaleev, N. K. and Carpenter, M. H., "High-Order Energy Stable WENO Schemes," AIAA Paper 2009-1135, Jan. 2009.
79. Yamaleev, N. K. and Carpenter, M. H., "Third-Order Energy Stable WENO Scheme," *Journal of Computational Physics*, Vol. 228, No. 8, 2009, pp. 3025–3047.
80. Yamaleev, N. K. and Carpenter, M. H., "A Systematic Methodology for Constructing High-Order Energy Stable WENO Schemes," *Journal of Computational Physics*, Vol. 228, 2009, pp. 4248–4272.
81. Kravchenko, A. G. and Moin, P., "On the Effect of Numerical Errors in Large Eddy Simulations of Turbulent Flows," *Journal of Computational Physics*, Vol. 131, 1997, pp. 310–322.
82. Lilly, D. K., "On the Computational Stability of Numerical Solutions of Time-Dependent Non-Linear Geophysical Fluid Dynamics Problems," *Monthly Weather Review*, Vol. 93, No. 1, 1965, pp. 11–26.
83. Ducros, F., Laporte, F., Soulères, T., Guinot, V., Moinat, P., and Caruelle, B., "High-Order Fluxes for Conservative Skew-Symmetric-Like Schemes in Structured Meshes: Application to Compressible Flows," *Journal of Computational Physics*, Vol. 161, 2000, pp. 114–139.

84. Verstappen, R. W. C. P. and Veldman, A. E. P., "Symmetry-Preserving Discretization of Turbulent Flow," *Journal of Computational Physics*, Vol. 187, 2003, pp. 343–368.
85. Feiereisen, W. J., Reynolds, W. C., and Ferziger, J. H., "Numerical Simulation of a Compressible Homogeneous, Turbulent Shear Flow," Rep. TF-13, Thermosci. Div., Department of Mech. Eng., Stanford University, 1981.
86. Kok, J. C., "A High-Order Low-Dispersion Symmetry-Preserving Finite-Volume Method for Compressible Flow on Curvilinear Grids," *Journal of Computational Physics*, Vol. 228, 2009, pp. 6811–6832.
87. Ghosal, S., "An Analysis of Numerical Errors in Large-Eddy Simulations of Turbulence," *Journal of Computational Physics*, Vol. 125, 1996, pp. 187–206.
88. Tam, C. K. W. and Webb, J. C., "Dispersion-Relation-Preserving Finite Difference Schemes for Computational Acoustics," *Journal of Computational Physics*, Vol. 107, 1993, pp. 262–281.
89. Batchelor, G. K., *The Theory of Homogeneous Turbulence*, Cambridge University Press, Cambridge, 1953.
90. Tsinober, A., *An Informal Introduction to Turbulence*, Kluwer Academic Publishers, Dordrecht, 2001.
91. Reid, W. H. and Harris, D. L., "Similarity Spectra in Isotropic Turbulence," *Physics of Fluids*, Vol. 2, 1959, pp. 139–146.
92. Kraichnan, R. H., "The Structure of Isotropic Turbulence at Very High Reynolds Numbers," *Journal of Fluid Mechanics*, Vol. 5, 1959, pp. 497–543.
93. Smith, L. M. and Reynolds, W. C., "The Dissipation Range Spectrum and the Velocity Derivative Skewness in Turbulent Flows," *Physics of Fluids A*, Vol. 3, 1991, pp. 992–994.

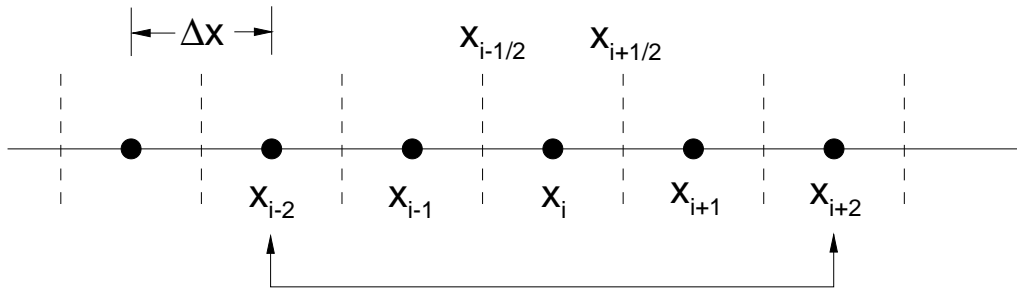


Figure 1. Uniform computational grid for WENO scheme.

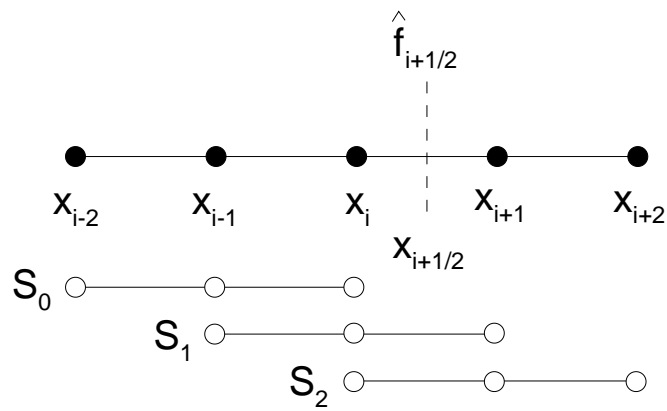


Figure 2. The five point WENO stencil constructed from three-point stencils S_0 , S_1 , and S_2 .

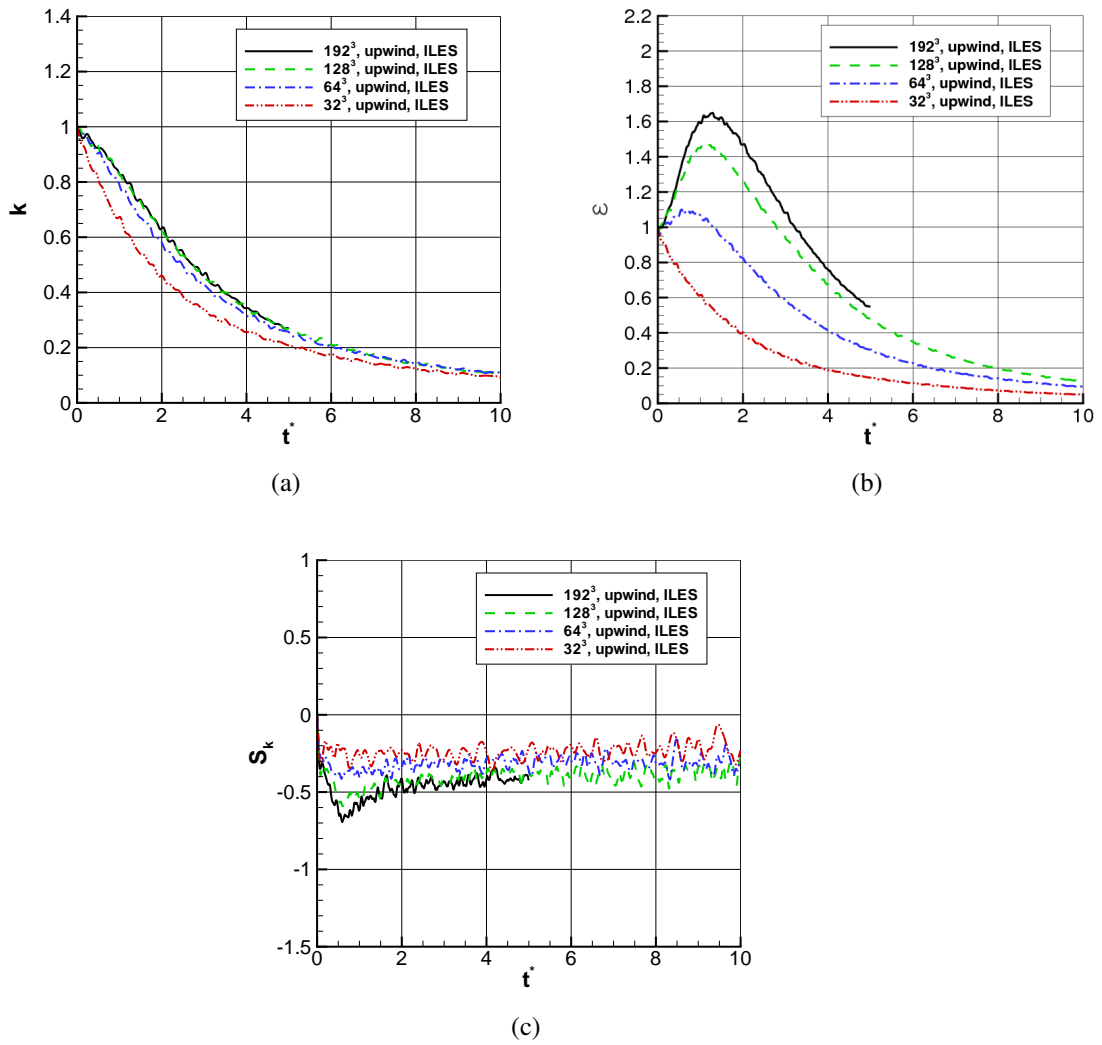


Figure 3. Time history of various statistics for upwind ILES for various grid sizes; (a) normalized kinetic energy, (b) normalized dissipation, (c) skewness.

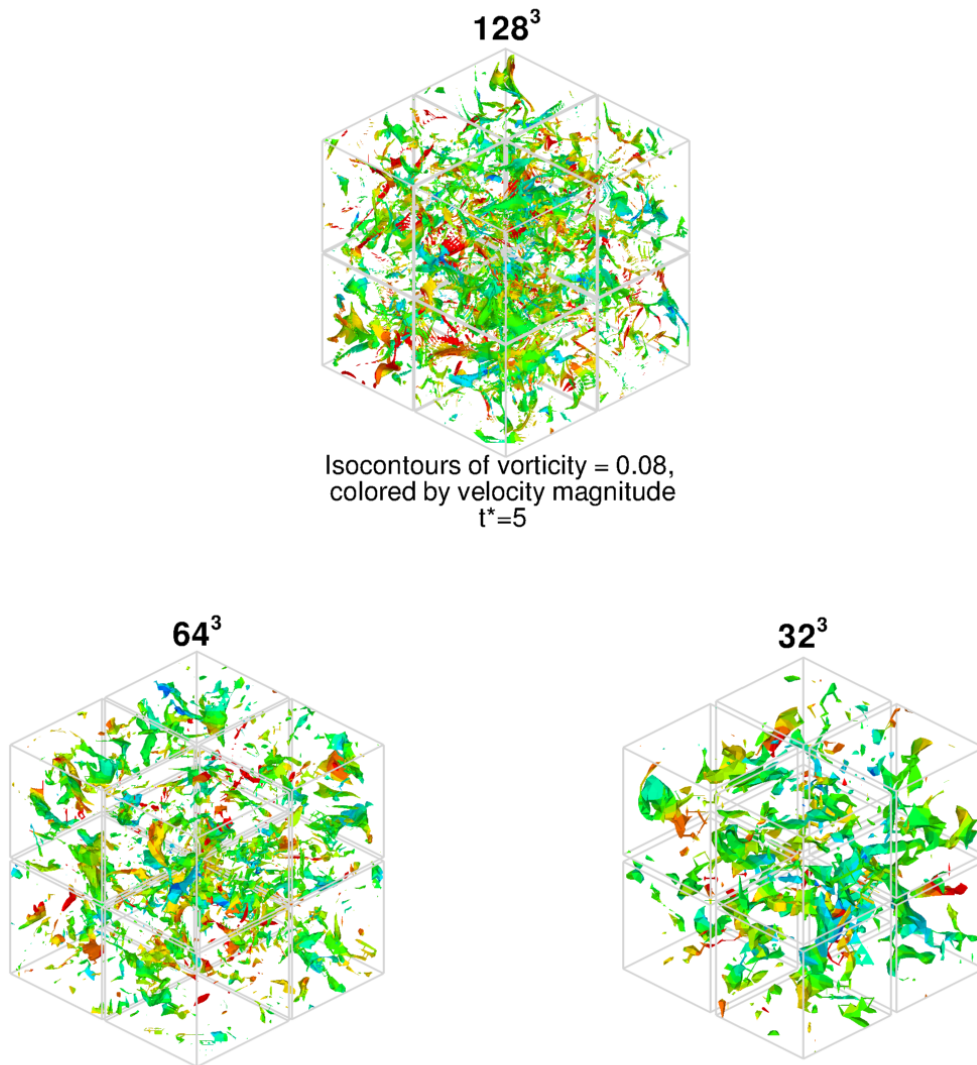


Figure 4. Isocontours of nondimensional vorticity for upwind ILES for various grid sizes, at $t^* = 5$.

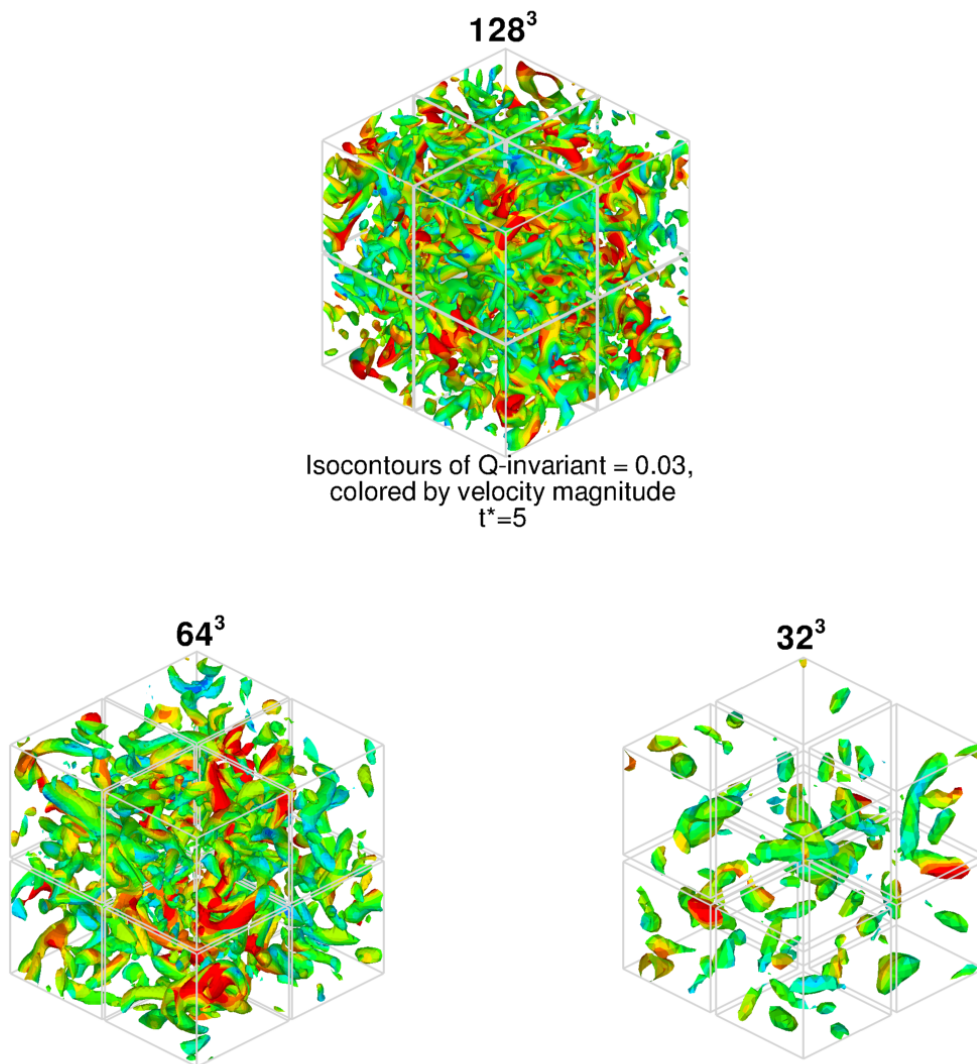


Figure 5. Isocontours of nondimensional Q-invariant for upwind ILES for various grid sizes, at $t^* = 5$.

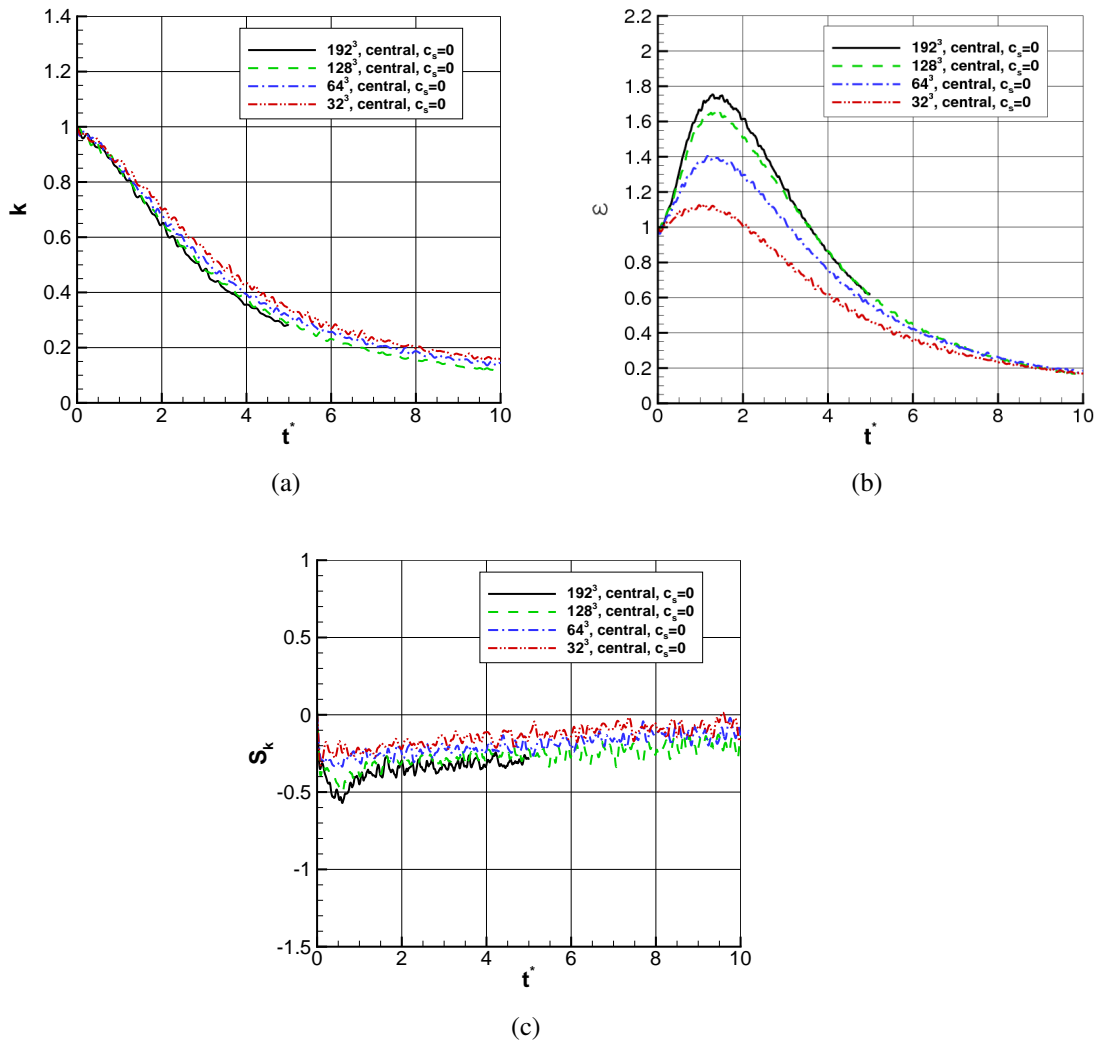


Figure 6. Time history of various statistics for central ($c_s = 0$) for various grid sizes; (a) normalized kinetic energy, (b) normalized dissipation, (c) skewness.

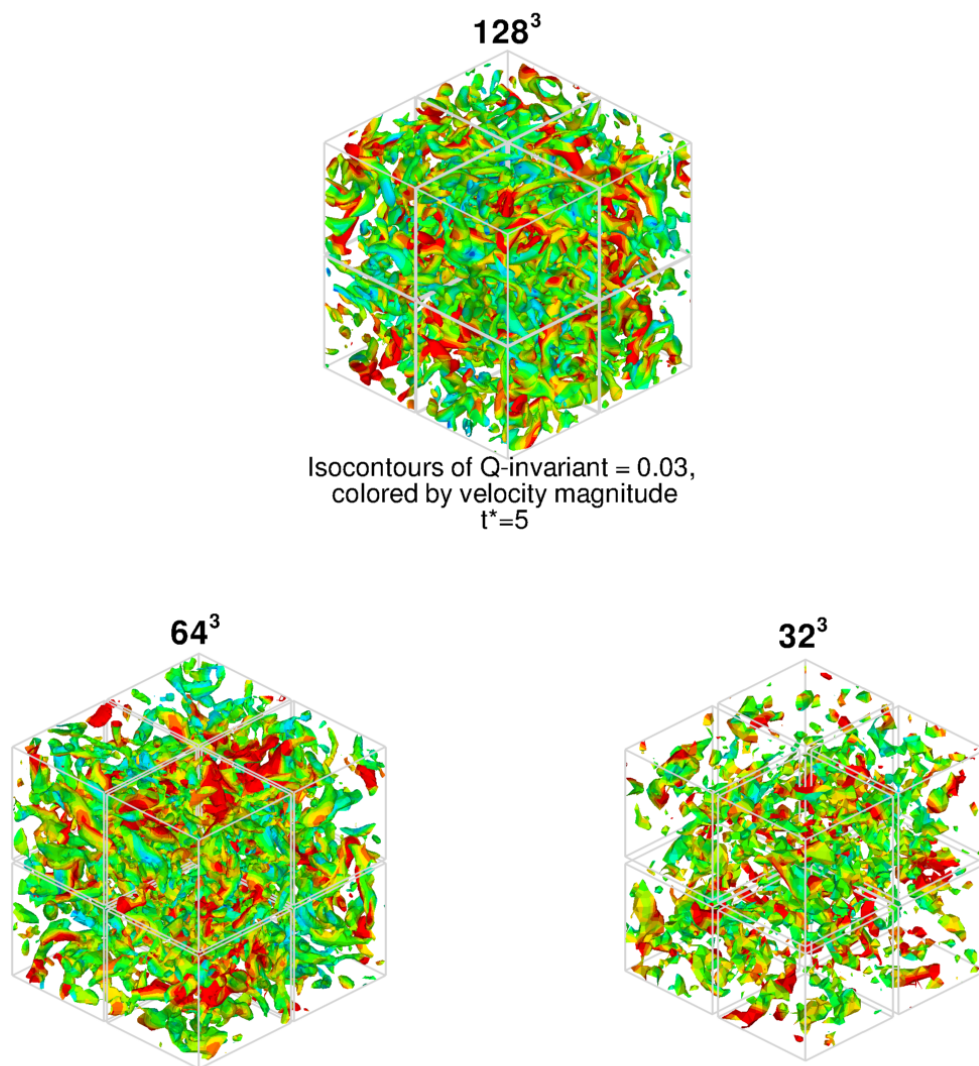


Figure 7. Isocontours of nondimensional Q-invariant for central ($c_s = 0$) for various grid sizes, at $t^* = 5$.

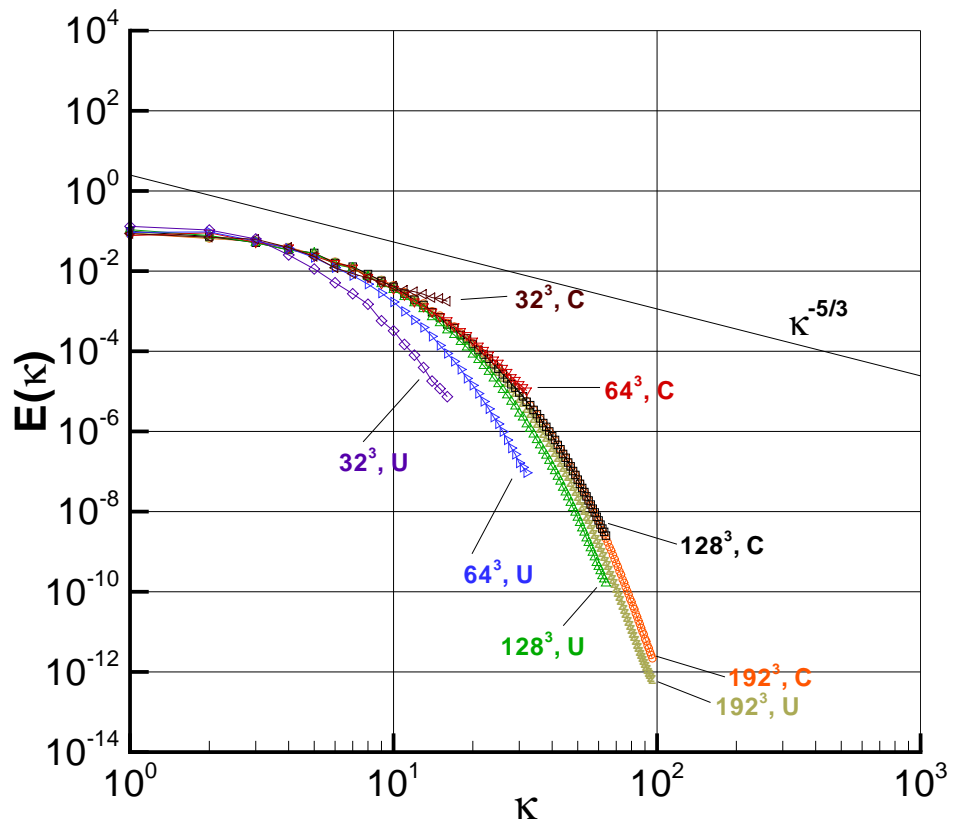


Figure 8. Energy spectrum for upwind ILES and central ($c_s = 0$), at $t^* = 5$; U indicates upwind, C indicates central.

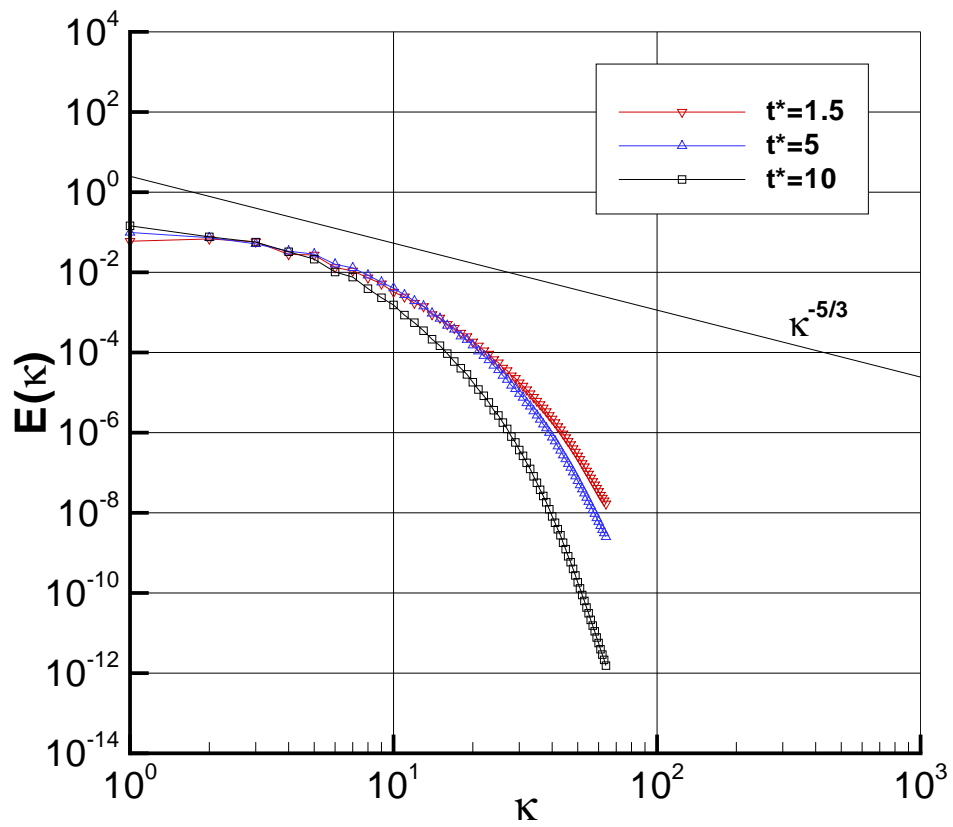


Figure 9. Energy spectrum at three different times for central ($c_s = 0$), 128^3 grid.

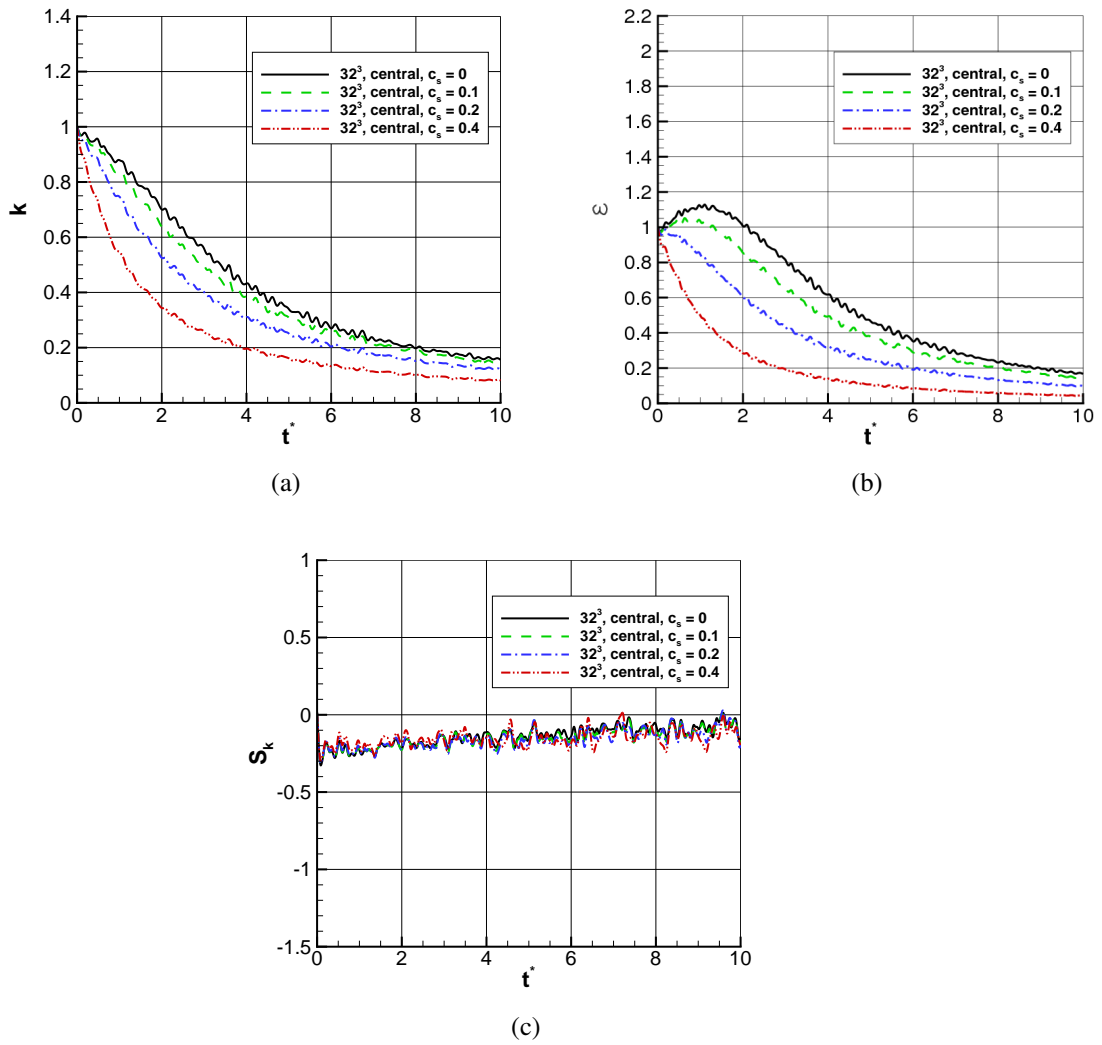


Figure 10. Time history of various statistics for central differencing with the Smagorinsky model on 32^3 for various c_s values; (a) normalized kinetic energy, (b) normalized dissipation, (c) skewness.

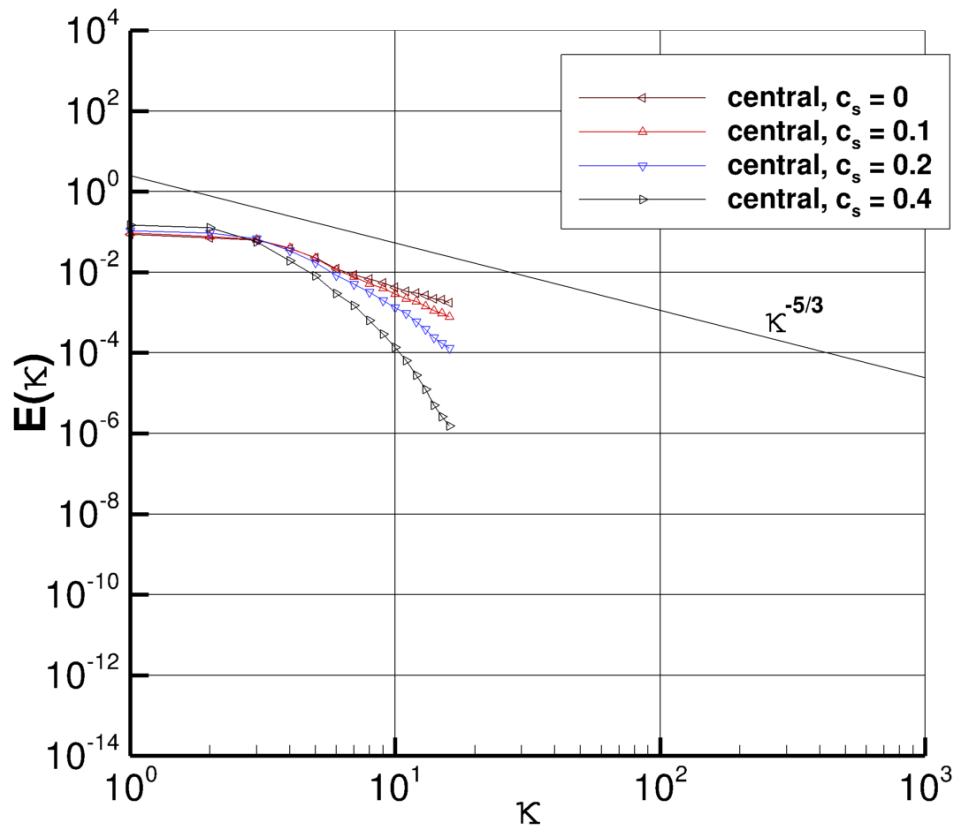


Figure 11. Energy spectrum for the Smagorinsky model with different values of c_s , 32^3 , central differencing, at $t^* = 5$.

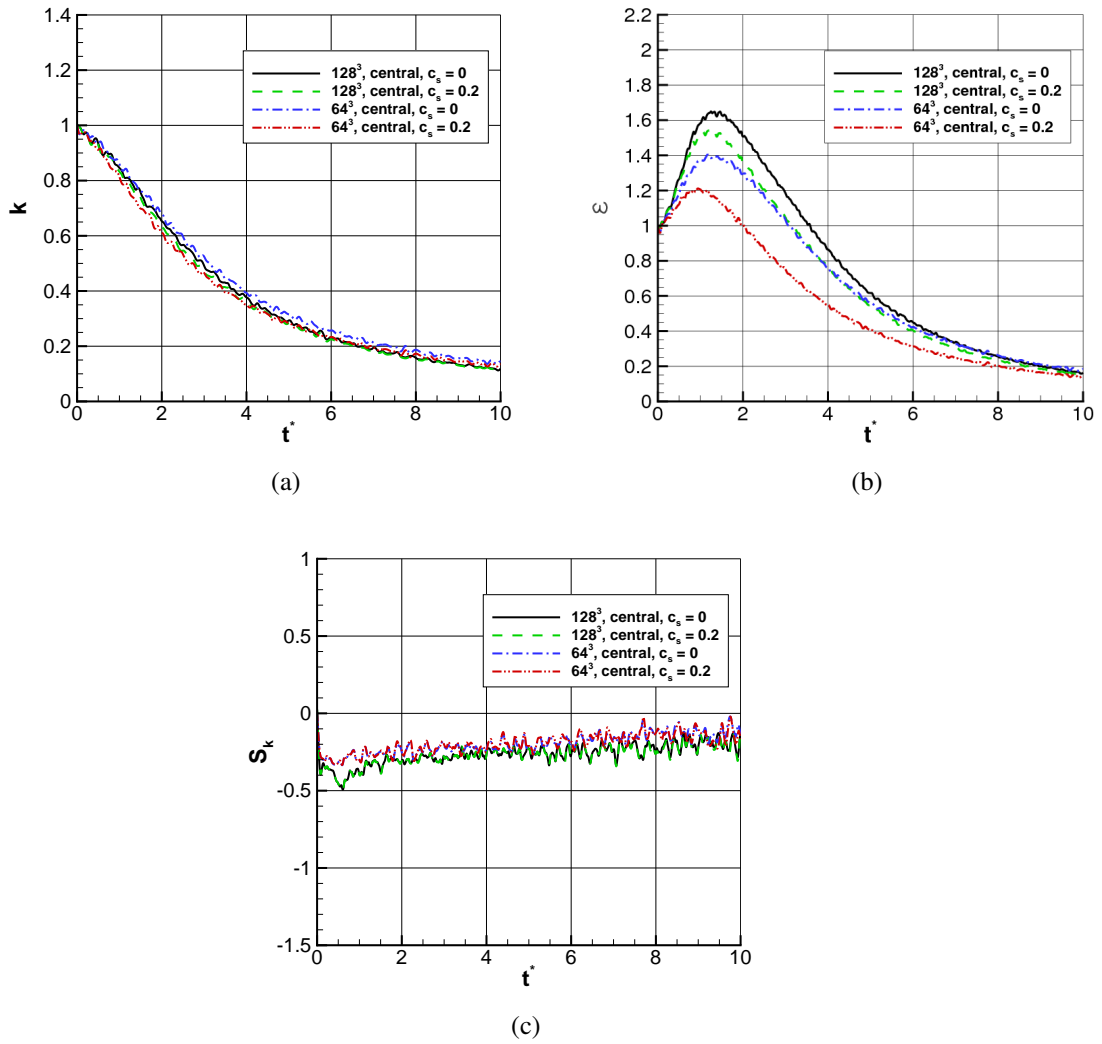


Figure 12. Time history of various statistics for central differencing with the Smagorinsky model with different values of c_s on 64^3 and 128^3 ; (a) normalized kinetic energy, (b) normalized dissipation, (c) skewness.

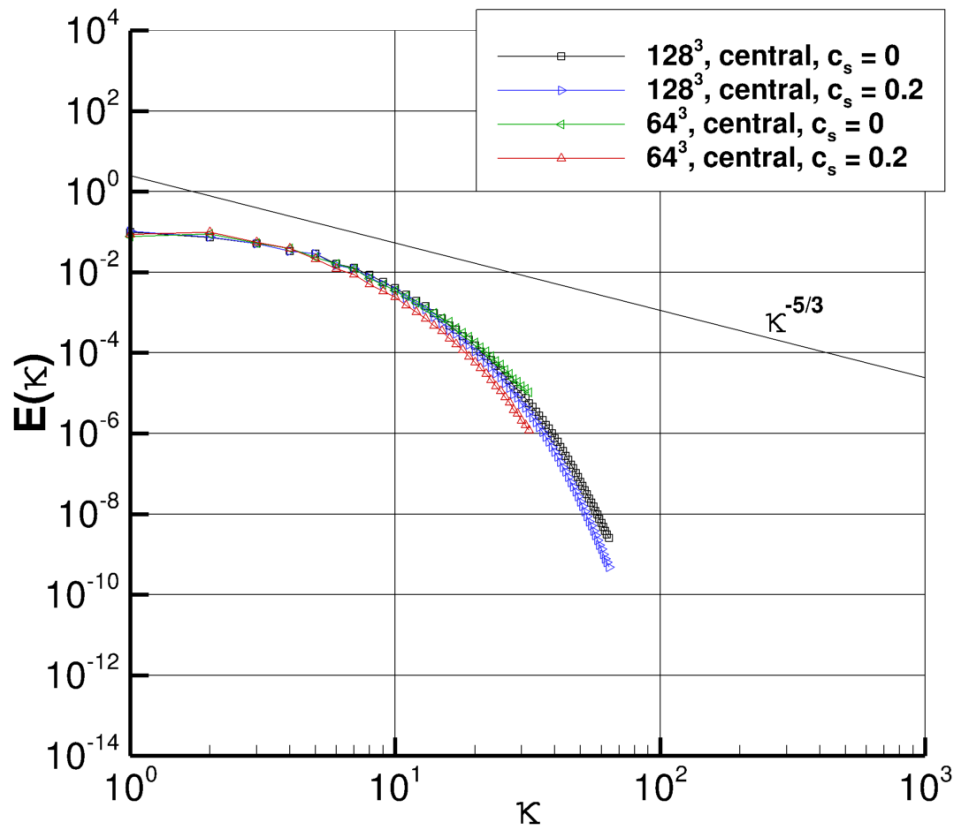


Figure 13. Energy spectrum for the Smagorinsky model with different values of c_s on two finer grid sizes, central differencing, at $t^* = 5$.

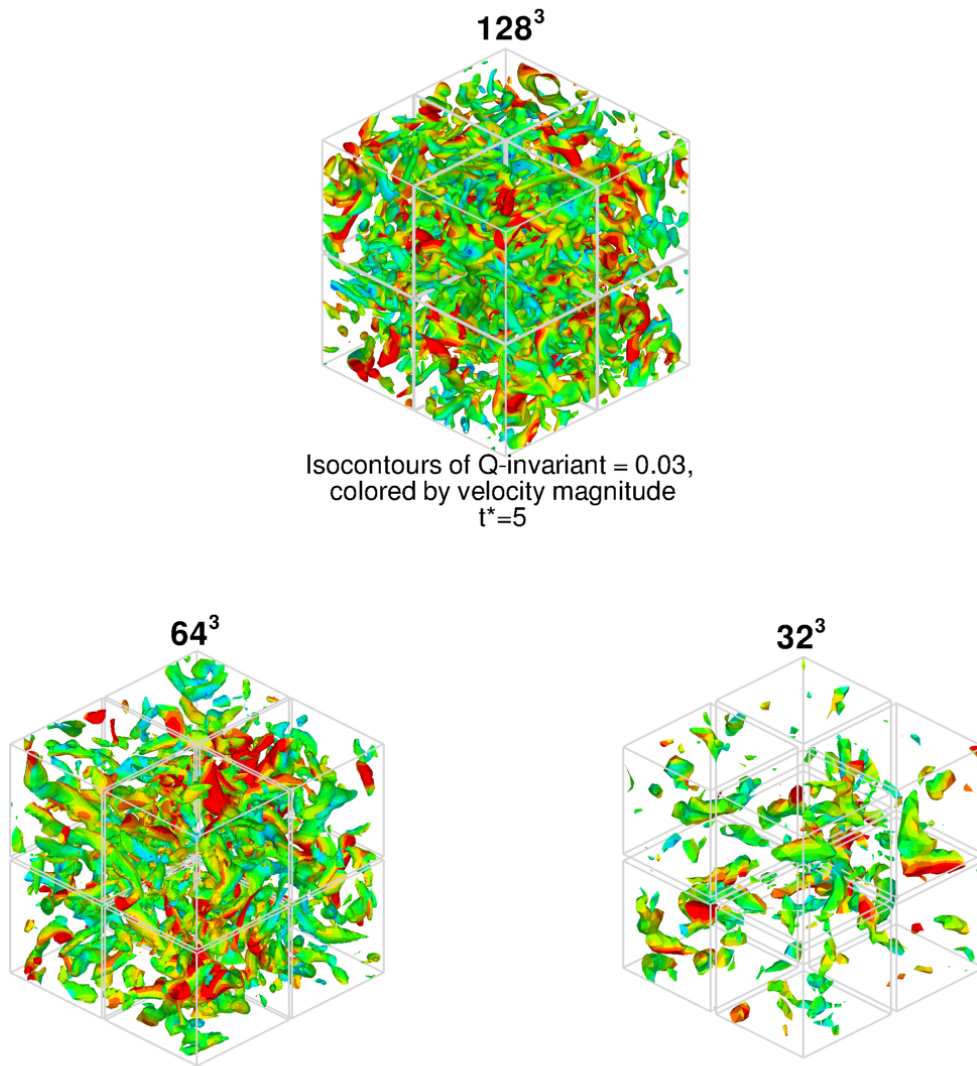


Figure 14. Isocontours of nondimensional Q-invariant for central differencing (Smagorinsky model with $c_s = 0.2$) for various grid sizes, at $t^* = 5$.

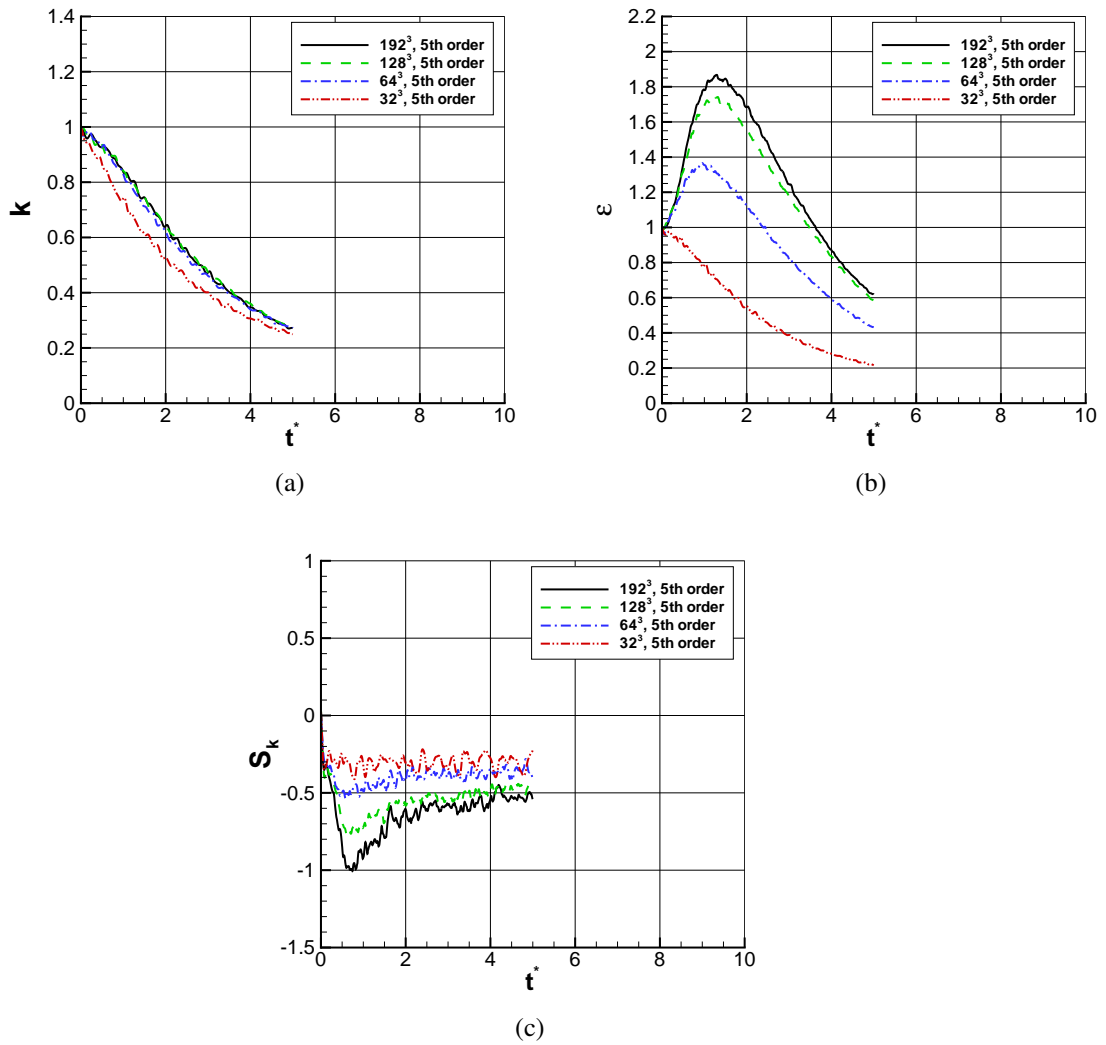


Figure 15. Time history of various statistics on different grid sizes using 5th order WENO-L ILES scheme; (a) normalized kinetic energy, (b) normalized dissipation, (c) skewness.

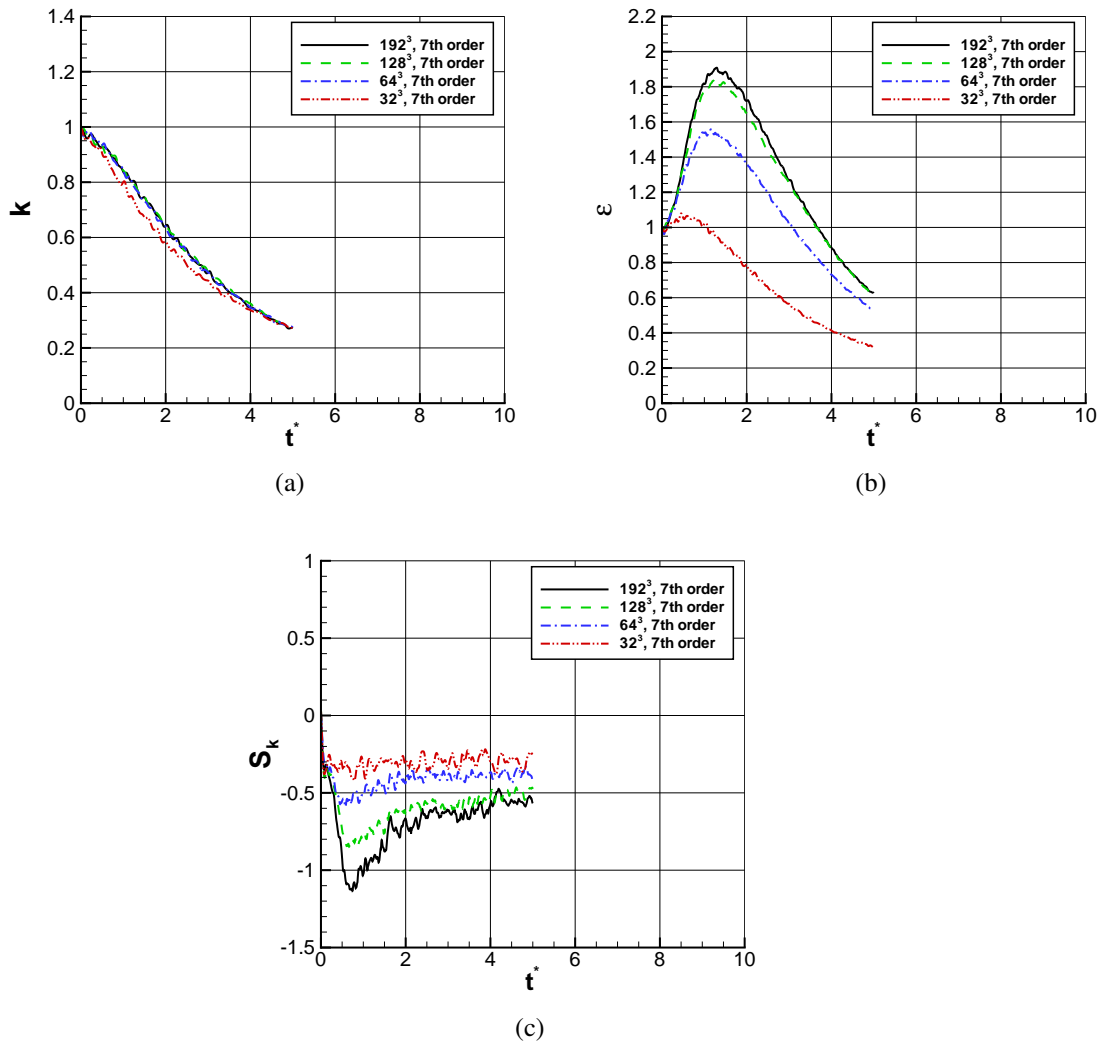


Figure 16. Time history of various statistics on different grid sizes using 7th order WENO-L ILES scheme; (a) normalized kinetic energy, (b) normalized dissipation, (c) skewness.

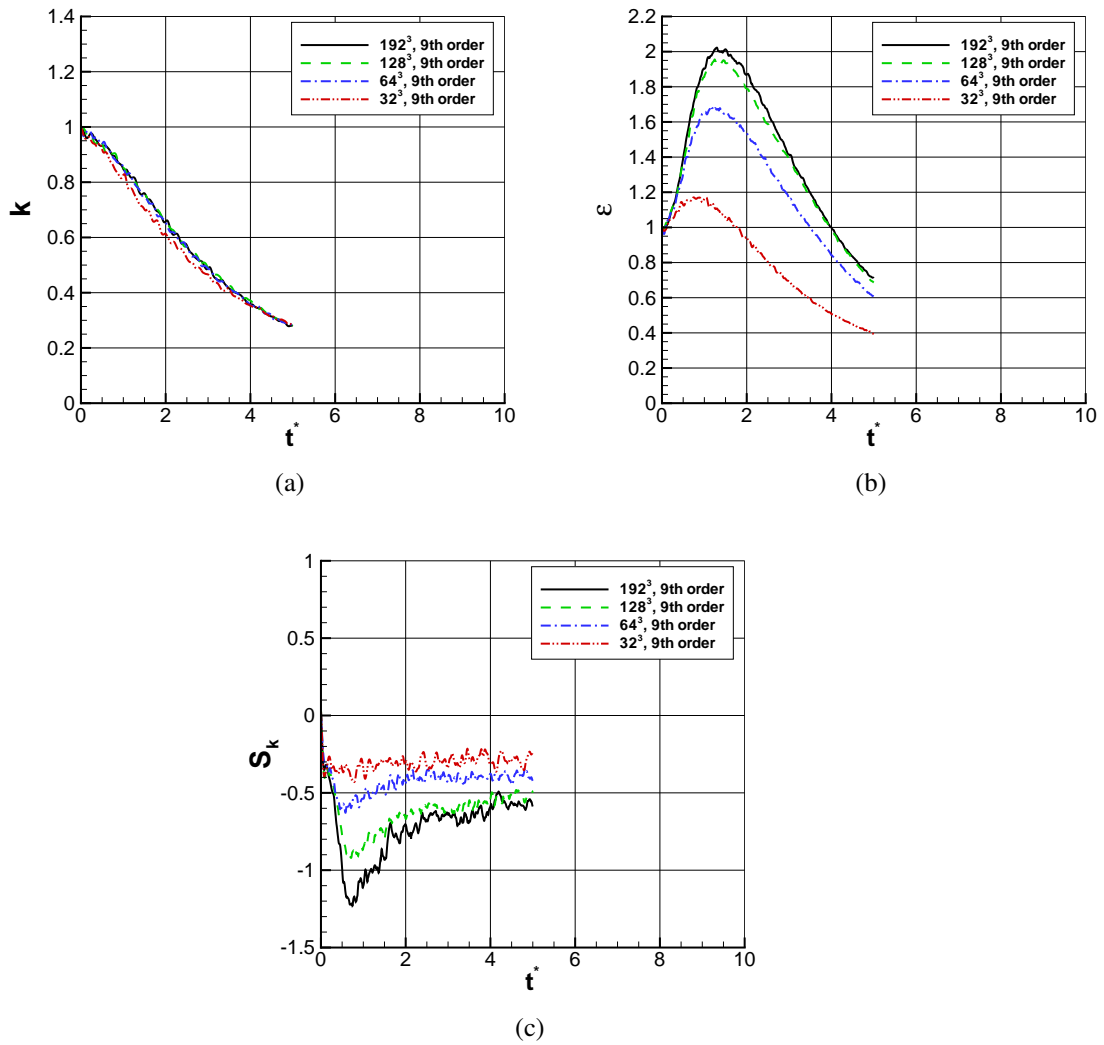


Figure 17. Time history of various statistics on different grid sizes using 9th order WENO-L ILES scheme; (a) normalized kinetic energy, (b) normalized dissipation, (c) skewness.

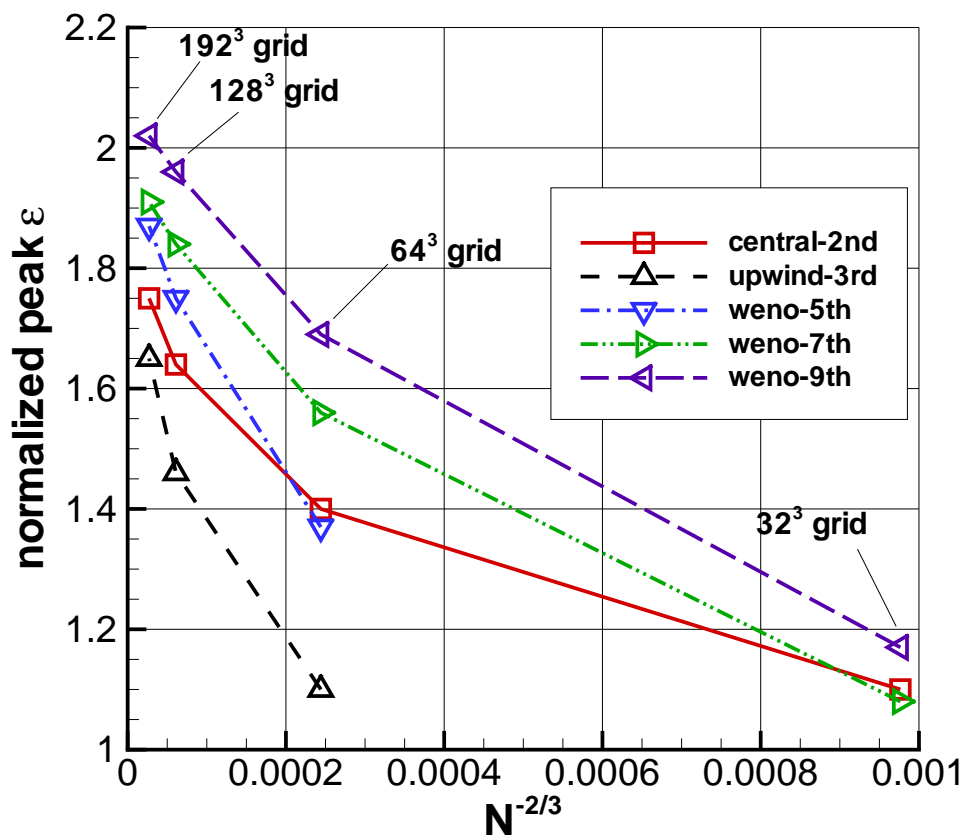


Figure 18. Normalized peak ε as a function of grid spacing squared.

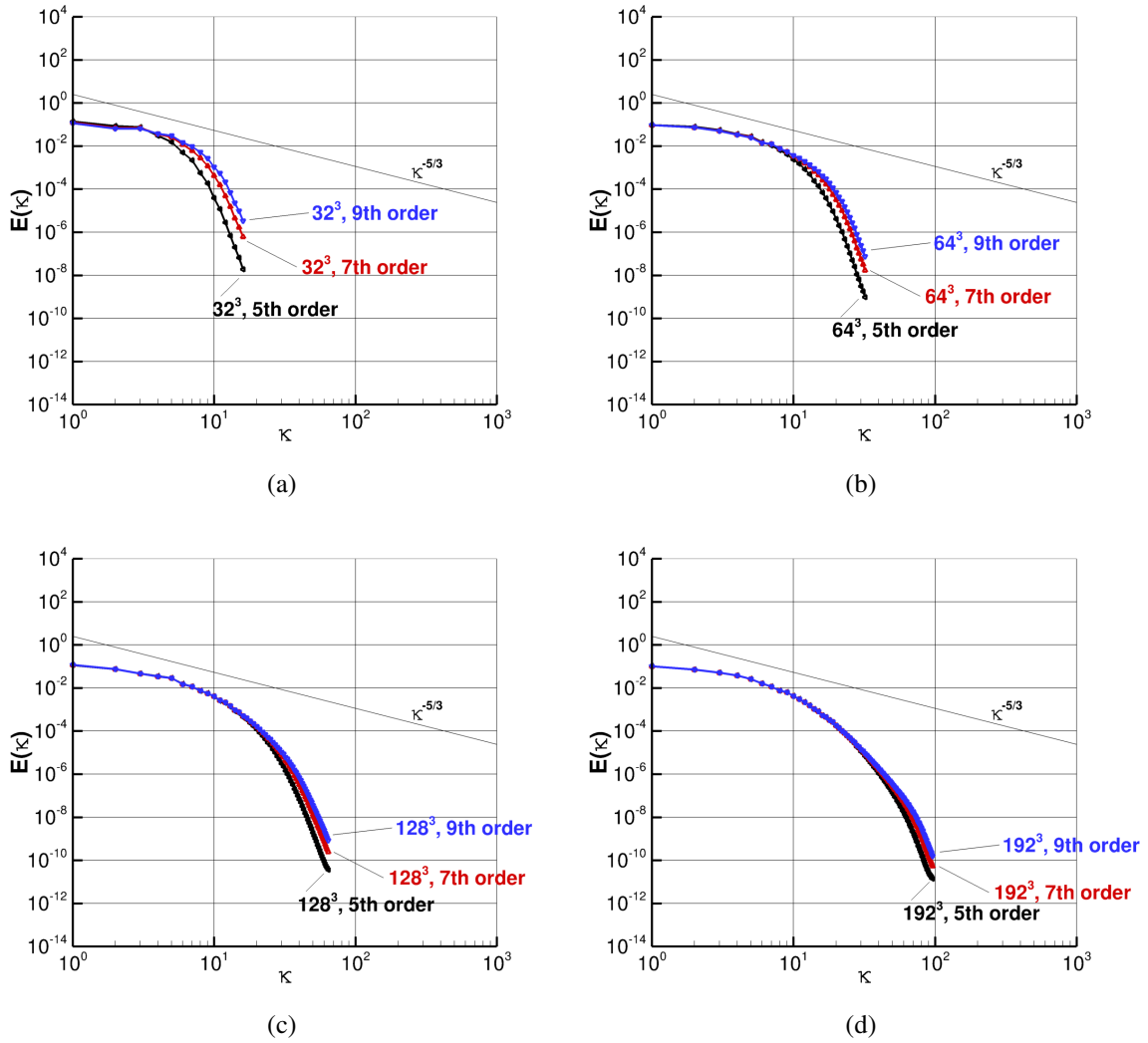


Figure 19. Energy spectrum for 5th-order, 7th-order, and 9th-order WENO-L ILES on four different grids at $t^* = 5$; (a) 32^3 , (b) 64^3 , (c) 128^3 , (d) 192^3 .

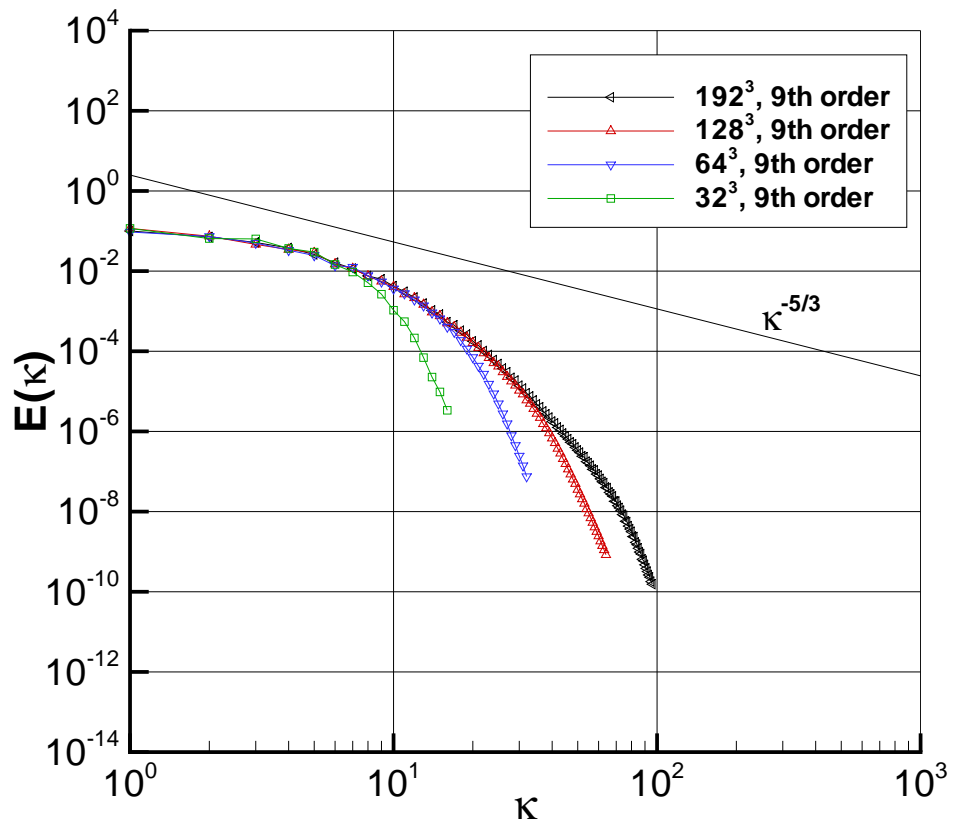


Figure 20. Energy spectrum for 9th-order WENO-L ILES at $t^* = 5$

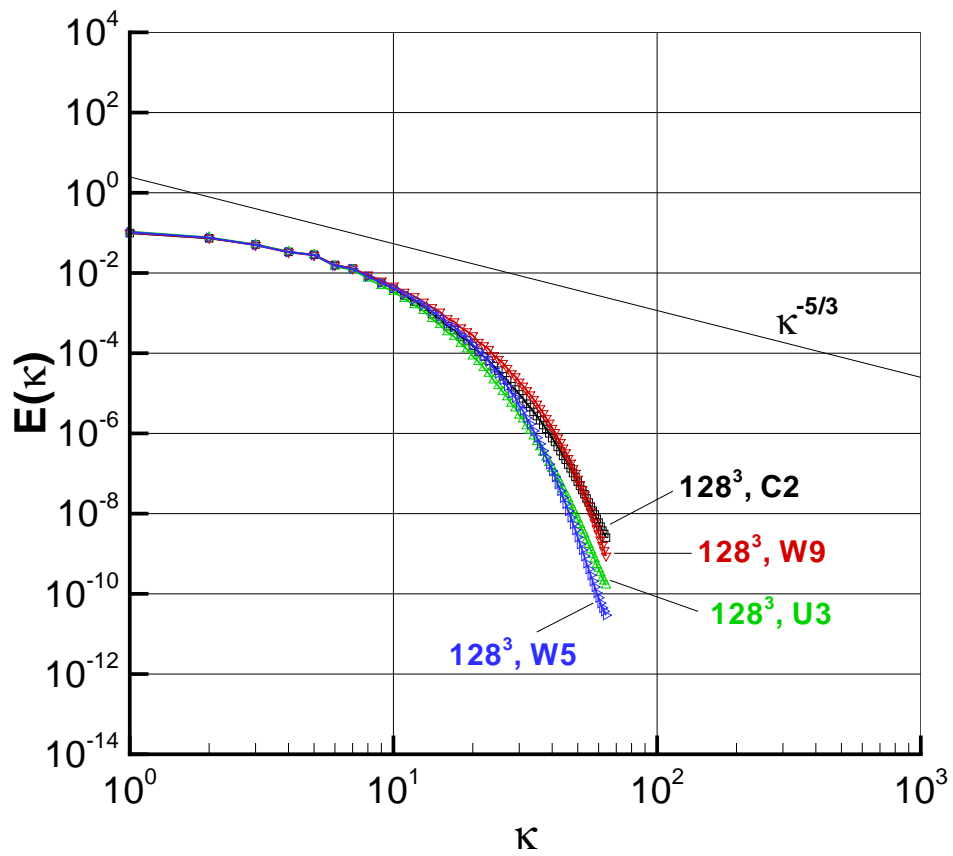


Figure 21. Energy spectrum for C2 = central 2nd order, $c_s = 0$ (CFL3D), U3 = upwind 3rd order ILES (CFL3D), W9 = WENO-L 9th order, and W5 = WENO-L 5th order ILES on same 128^3 grid, at $t^* = 5$.

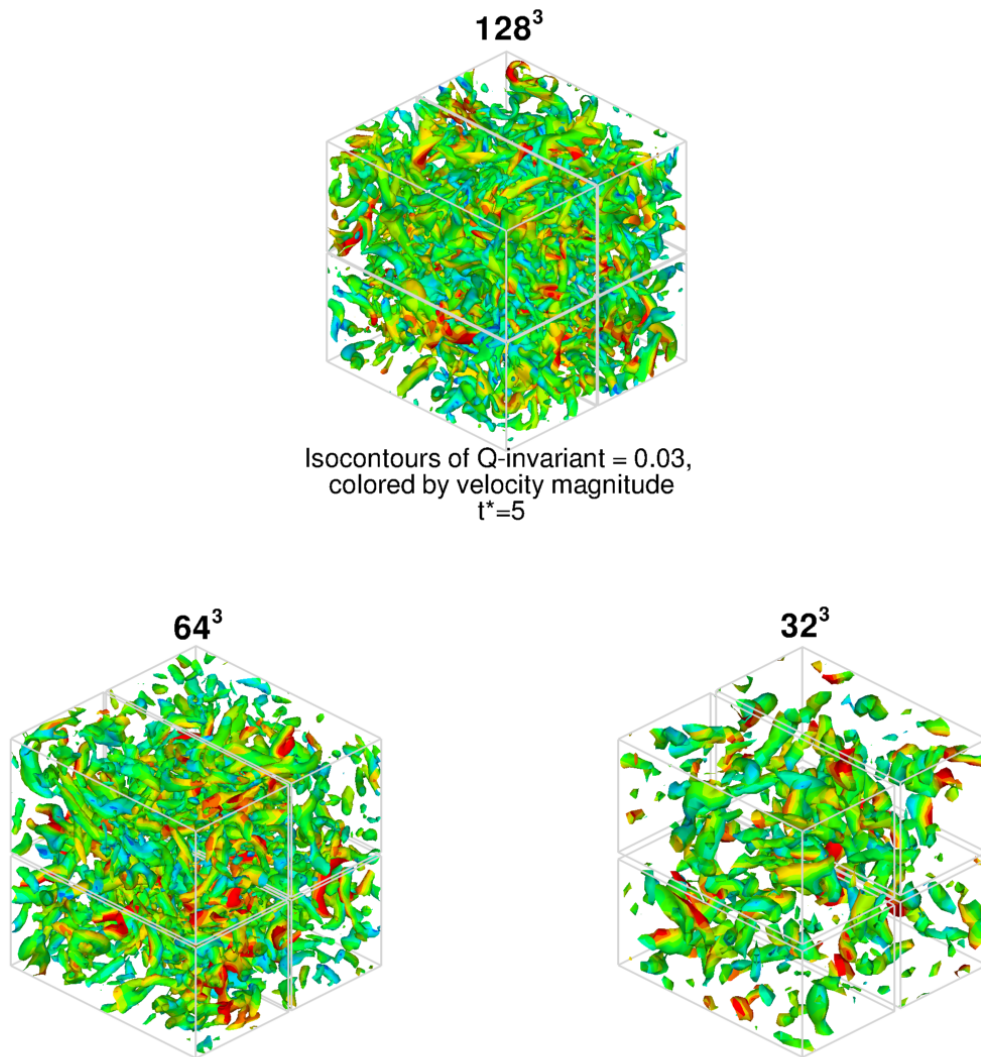


Figure 22. Isocontours of nondimensional Q-invariant for 9th-order WENO-L for various grid sizes, at $t^* = 5$.

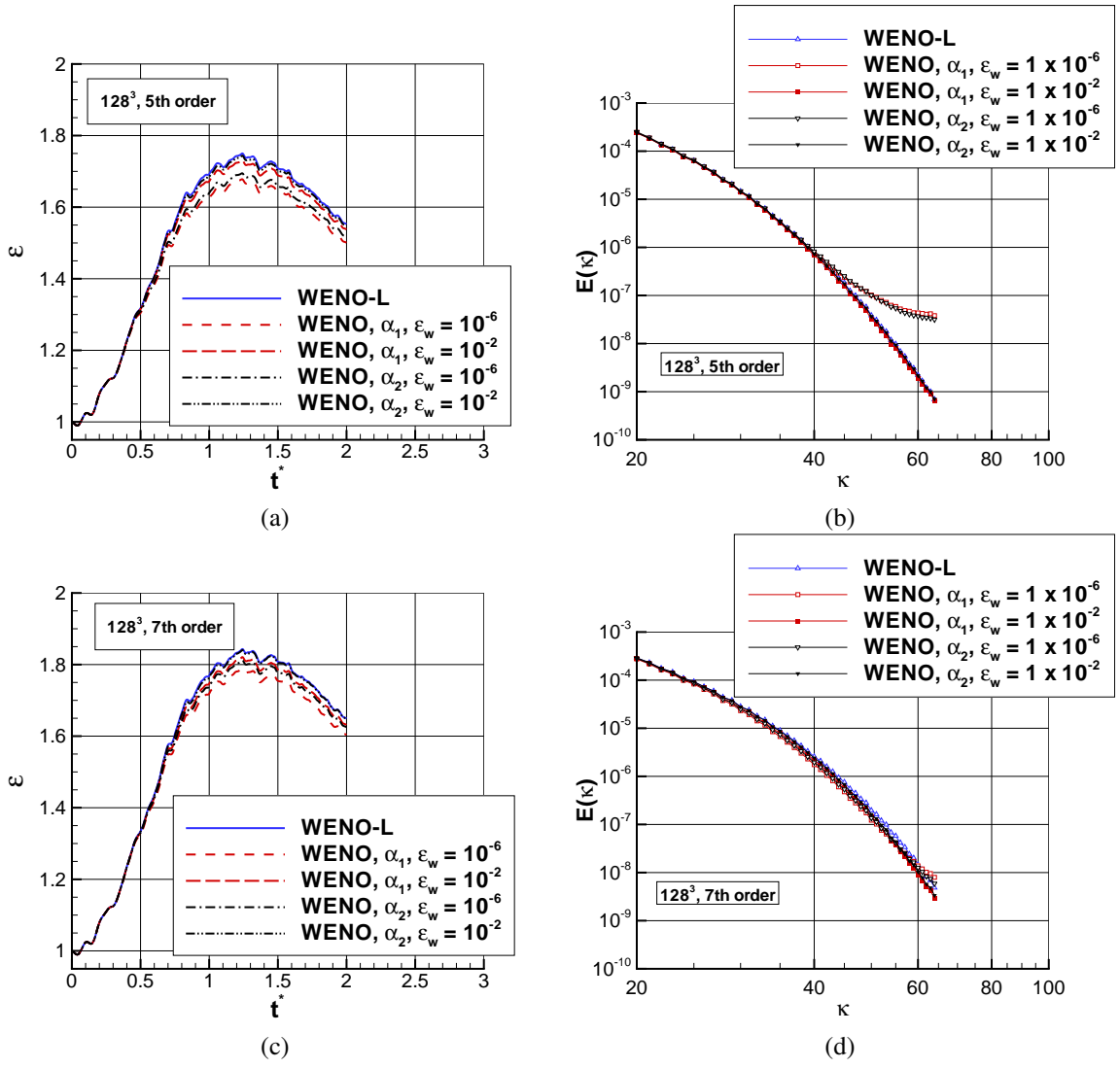


Figure 23. Effect of two different ways of computing nonlinear WENO weights on the normalized dissipation and energy spectrum (128^3); (a) dissipation, 5th order, (b) spectrum at $t^* = 2$, 5th order (c) dissipation, 7th order (d) spectrum at $t^* = 2$, 7th order.

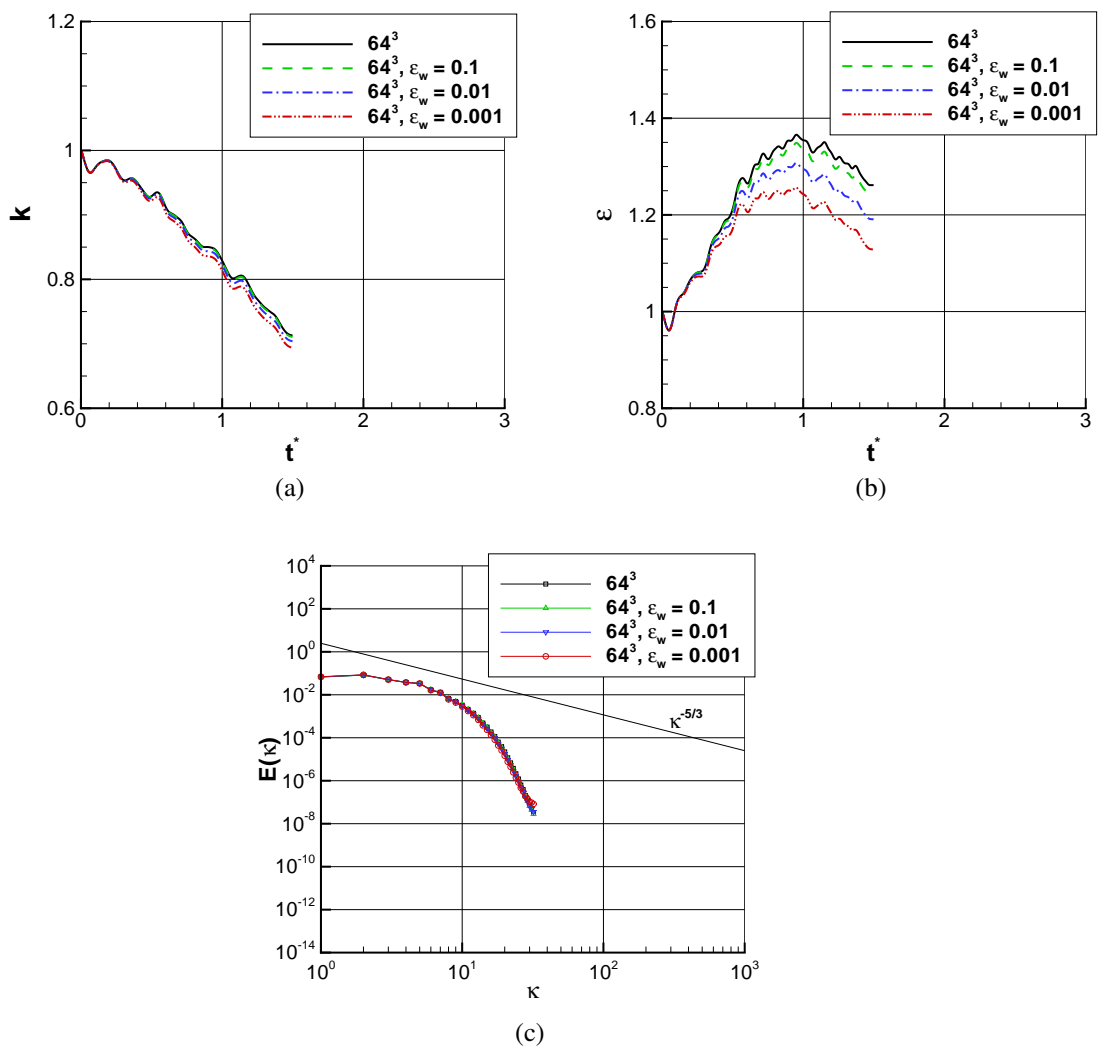


Figure 24. Time history of statistics and energy spectrum comparison for 5th-order WENO (64^3) with $\epsilon_w = 0.1$, $\epsilon_w = 0.01$, $\epsilon_w = 0.001$; (a) normalized kinetic energy, (b) normalized dissipation, (c) energy spectrum at $t^* = 1.5$.

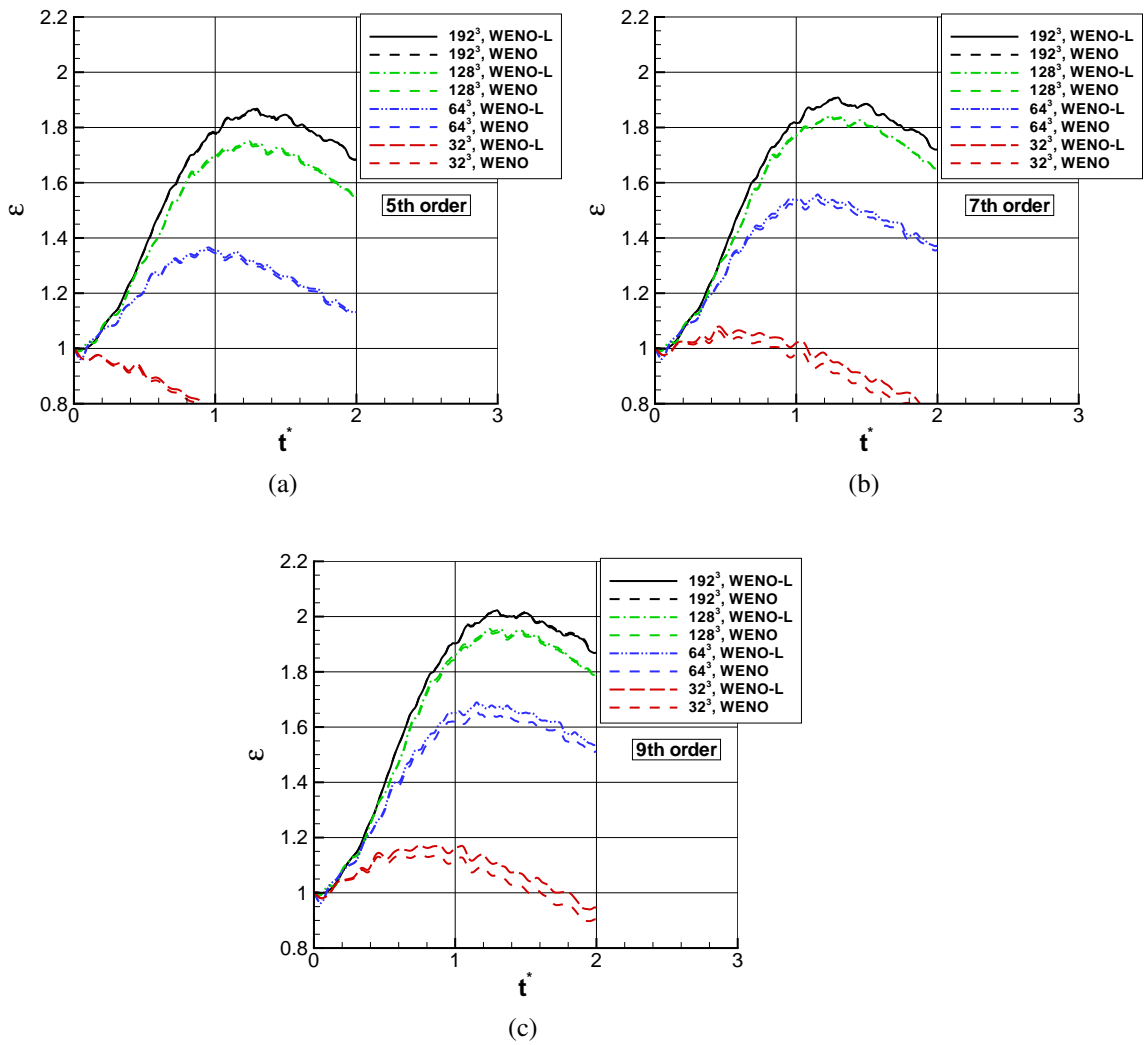


Figure 25. Comparison of normalized dissipation computed with WENO-L and WENO; (a) 5th order, b) 7th order, (c) 9th order.

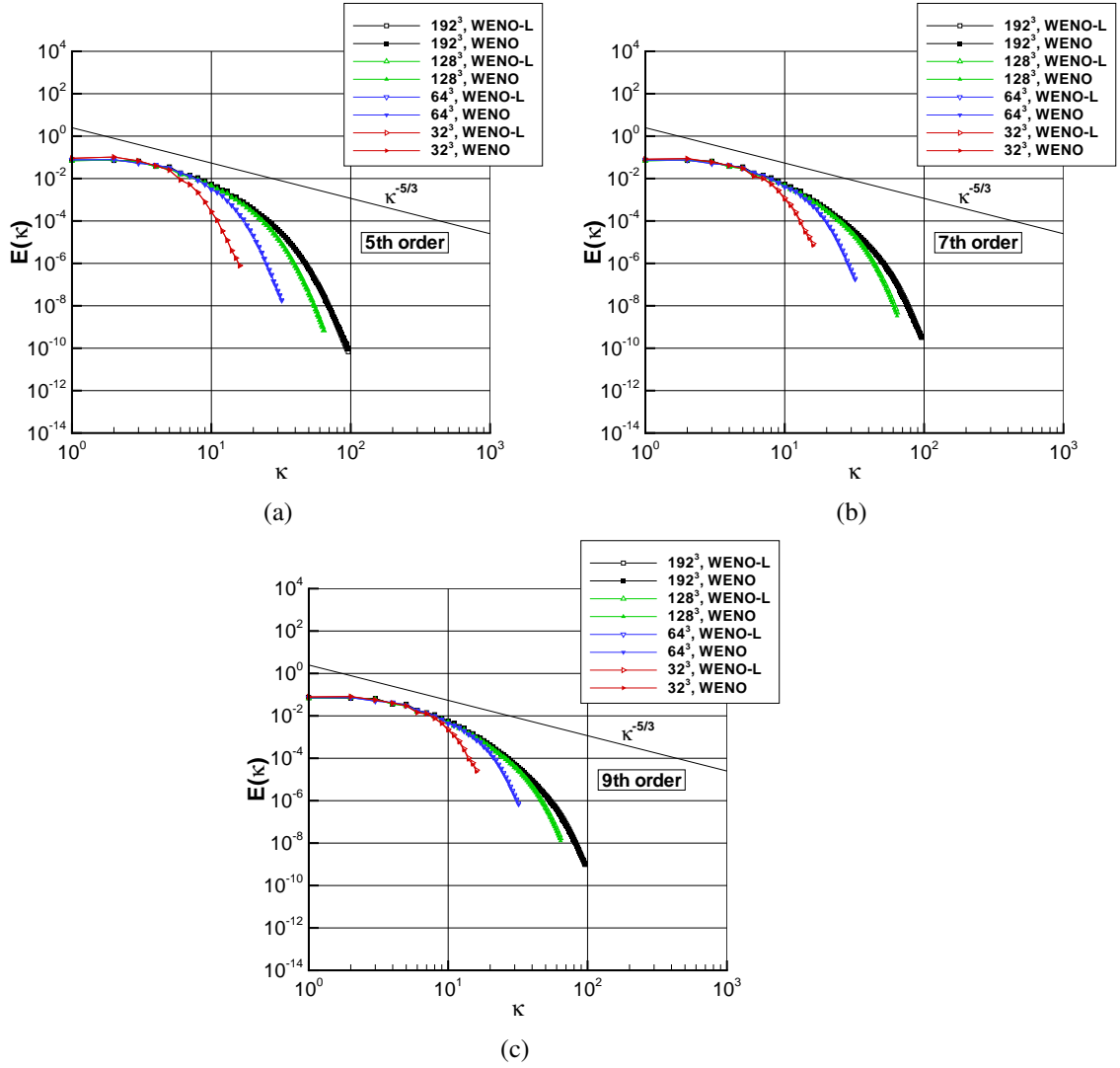


Figure 26. Comparison of energy spectrum computed with WENO-L and WENO, $t^* = 2$; (a) 5th order, b) 7th order, (c) 9th order.

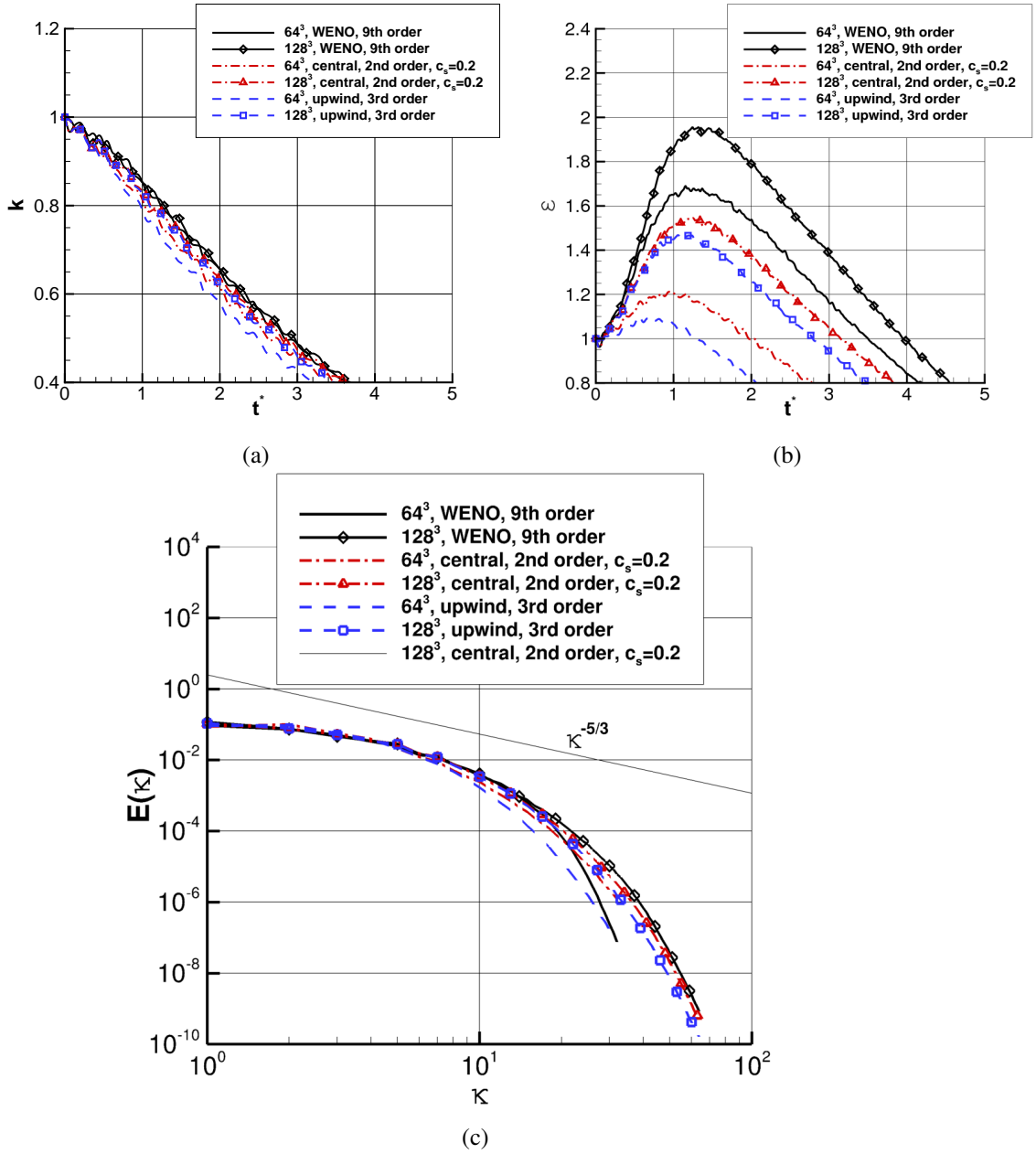


Figure 27. Time history of statistics and energy spectrum comparison for 9th-order WENO, 2nd-order central with Smagorinsky SGS model ($c_s = 0.2$), and 3rd-order upwind biased; (a) normalized kinetic energy, (b) normalized dissipation, (c) energy spectrum at $t^* = 5$.

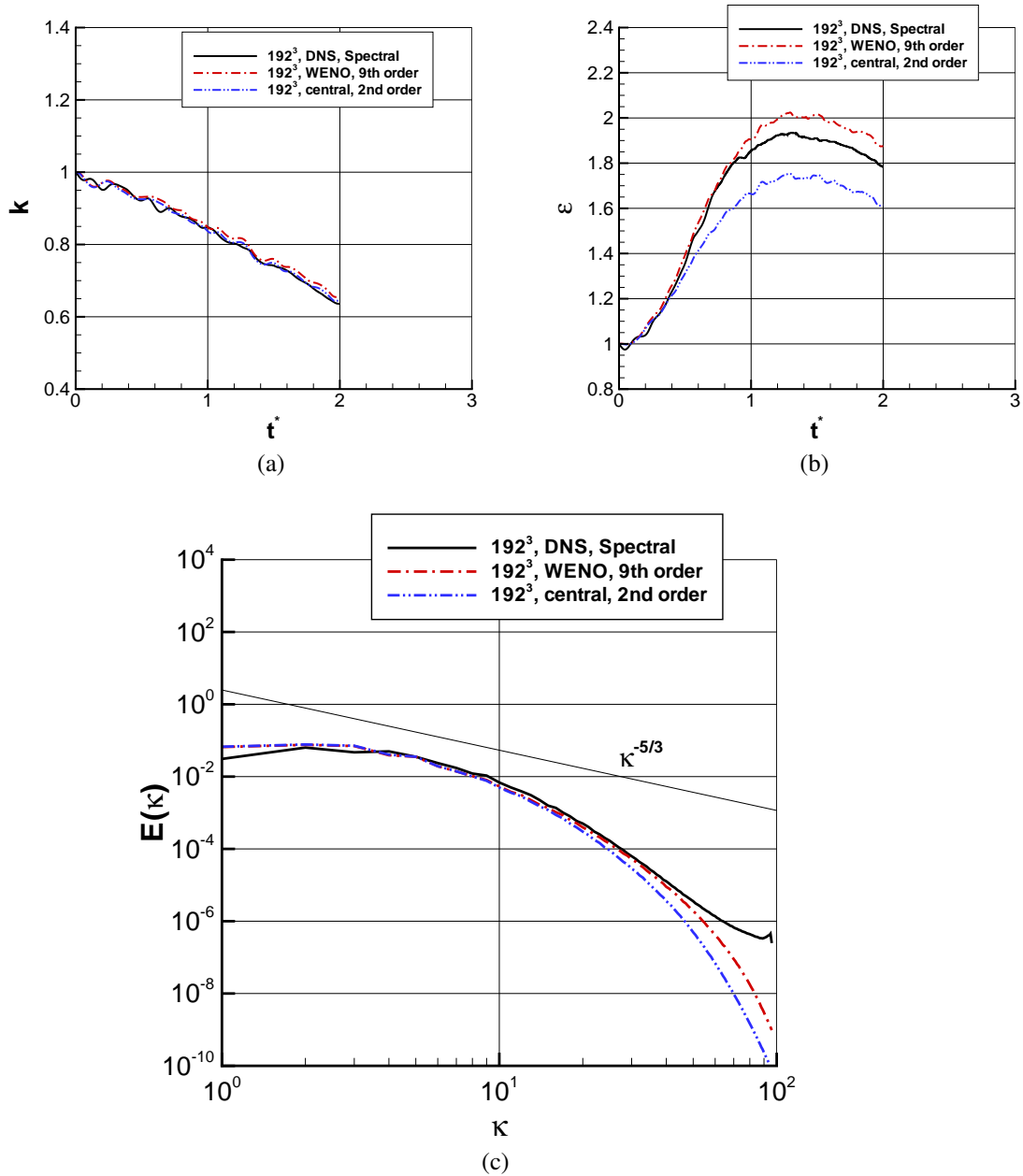


Figure 28. Time history of statistics and energy spectrum comparison for 9th-order WENO, 2nd-order central ($c_s = 0$), and spectral DNS; (a) normalized kinetic energy, (b) normalized dissipation, (c) energy spectrum at $t^* = 2$.

Appendix A

For the seventh-order WENO scheme, the fourth-order fluxes at $x_{i+1/2}$ are as follows:

$$\begin{aligned}\hat{f}_{i+1/2}^0 &= \frac{1}{12}(-3f_{i-3} + 13f_{i-2} - 23f_{i-1} + 25f_i), \\ \hat{f}_{i+1/2}^1 &= \frac{1}{12}(f_{i-2} - 5f_{i-1} + 13f_i + 3f_{i+1}), \\ \hat{f}_{i+1/2}^2 &= \frac{1}{12}(-f_{i-1} + 7f_i + 7f_{i+1} - f_{i+2}), \\ \hat{f}_{i+1/2}^3 &= \frac{1}{12}(3f_i + 13f_{i+1} - 5f_{i+2} + f_{i+3}),\end{aligned}$$

The corresponding ideal weights are as follows:

$$\omega_0 = 1/35, \quad \omega_1 = 12/35, \quad \omega_2 = 18/35, \quad \omega_3 = 4/35. \quad (\text{A1})$$

Then, substituting the $\hat{f}_{i+1/2}^k$ and the ideal weights into Eq. (29), we obtain the seventh-order flux at $x_{i+1/2}$, which is given by

$$\hat{f}_{i+1/2} = \frac{1}{420}(-3f_{i-3} + 25f_{i-2} - 101f_{i-1} + 319f_i + 214f_{i+1} - 38f_{i+2} + 4f_{i+3}). \quad (\text{A2})$$

Using Eq. (38) and the coefficients of the third-degree interpolating polynomials, the smoothness indicators for the nonlinear weights of the seventh-order scheme are found to be

$$\begin{aligned}\bar{\beta}_0 &= f_{i-3}(547f_{i-3} - 3882f_{i-2} + 4642f_{i-1} - 1854f_i) \\ &\quad - f_{i-2}(7042f_{i-2} - 17246f_{i-1} + 7042f_i) \\ &\quad + f_{i-1}(11003f_{i-1} - 9042f_i) + 2107f_i^2 \\ \bar{\beta}_1 &= f_{i-2}(267f_{i-2} - 1642f_{i-1} + 1602f_i - 494f_{i+1}) \\ &\quad - f_{i-1}(2843f_{i-1} - 5966f_i + 1922f_{i+1}) \\ &\quad + f_i(3443f_i - 2522f_{i+1}) + 547f_{i+1}^2 \\ \bar{\beta}_2 &= f_{i-1}(547f_{i-1} - 2522f_i + 1922f_{i+1} - 494f_{i+2}) \\ &\quad - f_i(3443f_i - 5966f_{i+1} + 1602f_{i+2}) \\ &\quad + f_{i+1}(2843f_{i+1} - 1642f_{i+2}) + 267f_{i+2}^2 \\ \bar{\beta}_3 &= f_i(2107f_i - 9402f_{i+1} + 7042f_{i+2} - 1854f_{i+3}) \\ &\quad - f_{i+1}(11003f_{i+1} - 17246f_{i+2} + 4642f_{i+3}) \\ &\quad + f_{i+2}(7043f_{i+2} - 3882f_{i+3}) + 547f_{i+3}^2\end{aligned} \quad (\text{A3})$$

and $\beta_k = \bar{\beta}_k/240$ for $k = 0, \dots, 3$.

For the ninth-order WENO scheme, the fifth-order fluxes at $x_{i+1/2}$ are as follows:

$$\begin{aligned}
\hat{f}_{i+1/2}^0 &= \frac{1}{60}(12f_{i-4} - 63f_{i-3} + 137f_{i-2} - 163f_{i-1} + 137f_i), \\
\hat{f}_{i+1/2}^1 &= \frac{1}{60}(-3f_{i-3} + 17f_{i-2} - 43f_{i-1} + 77f_i + 12f_{i+1}), \\
\hat{f}_{i+1/2}^2 &= \frac{1}{60}(2f_{i-2} - 13f_{i-1} + 47f_i + 27f_{i+1} - 3f_{i+2}), \\
\hat{f}_{i+1/2}^3 &= \frac{1}{60}(-3f_{i-1} + 27f_i + 47f_{i+1} - 13f_{i+2} + 2f_{i+3}), \\
\hat{f}_{i+1/2}^4 &= \frac{1}{60}(12f_i + 77f_{i+1} - 43f_{i+2} + 17f_{i+3} - 3f_{i+4}),
\end{aligned} \tag{A4}$$

The corresponding ideal weights are as follows:

$$\omega_0 = 1/126, \quad \omega_1 = 10/63, \quad \omega_2 = 10/21, \quad \omega_3 = 20/63, \quad \omega_4 = 5/126. \tag{A5}$$

Then, substituting the $\hat{f}_{i+1/2}^k$ and the ideal weights into Eq. (29), we obtain the ninth-order flux at $x_{i+1/2}$, which is given by

$$\begin{aligned}
\hat{f}_{i+1/2} &= \frac{1}{7560} [12f_{i-4} - 123f_{i-3} + 597f_{i-2} - 1923f_{i-1} + 5637f_i \\
&\quad + 4125f_{i+1} - 915f_{i+2} + 165f_{i+3} - f_{i+4}]
\end{aligned} \tag{A6}$$

Using Eq. (38) and the coefficients of the fourth-degree interpolating polynomials, the smoothness indicators for the nonlinear weights of the ninth-order scheme are found to be

$$\begin{aligned}
\bar{\beta}_0 &= f_{i-4}(22658f_{i-4} - 20850f_{i-3} + 364863f_{i-2} - 288007f_{i-1} + 86329f_i) \\
&\quad - f_{i-3}(482963f_{i-3} - 1704396f_{i-2} + 1358458f_{i-1} - 411487f_i) \\
&\quad + f_{i-2}(1521393f_{i-2} - 2462076f_{i-1} + 758823f_i) \\
&\quad + f_{i-1}(1020563f_{i-1} - 649501f_i) + 107918f_i^2 \\
\bar{\beta}_1 &= f_{i-3}(6908f_{i-3} - 60871f_{i-2} + 99213f_{i-1} - 70237f_i + 18079f_{i+1}) \\
&\quad - f_{i-2}(138563f_{i-2} - 464976f_{i-1} + 337018f_i - 88297f_{i+1}) \\
&\quad + f_{i-1}(406293f_{i-1} - 611976f_i + 165153f_{i+1}) \\
&\quad + f_i(242723f_i - 140251f_{i+1}) + 22658f_{i+1}^2 \\
\bar{\beta}_2 &= f_{i-2}(6908f_{i-2} - 51001f_{i-1} + 67923f_i - 38947f_{i+1} + 8209f_{i+2}) \\
&\quad - f_{i-1}(104963f_{i-1} - 299076f_i + 179098f_{i+1} - 38947f_{i+2}) \\
&\quad + f_i(231153f_i - 299076f_{i+1} + 67923f_{i+2}) \\
&\quad + f_{i+1}(104963f_{i+1} - 51001f_{i+2}) + 6908f_{i+2}^2 \\
\bar{\beta}_3 &= f_{i-1}(22658f_{i-1} - 140251f_i + 165153f_{i+1} - 88297f_{i+2} + 18079f_{i+3}) \\
&\quad - f_i(242723f_i - 611976f_{i+1} + 337018f_{i+2} - 70237f_{i+3}) \\
&\quad + f_{i+1}(406293f_{i+1} - 464976f_{i+2} + 99213f_{i+3}) \\
&\quad + f_{i+2}(138563f_{i+2} - 60871f_{i+3}) + 6908f_{i+3}^2 \\
\bar{\beta}_4 &= f_i(107918f_i - 649501f_{i+1} + 758823f_{i+2} - 411487f_{i+3} + 86329f_{i+4}) \\
&\quad - f_{i+1}(1020563f_{i+1} - 2462076f_{i+2} + 1358458f_{i+3} - 233007f_{i+4}) \\
&\quad + f_{i+2}(1521393f_{i+2} - 1704396f_{i+3} + 364863f_{i+4}) \\
&\quad + f_{i+3}(482963f_{i+3} - 208501f_{i+4}) + 22658f_{i+4}^2
\end{aligned} \tag{A7}$$

and $\beta_k = \bar{\beta}_k/5040$ for $k = 0, \dots, 4$.

Table A1. The constants c_{rj} for 8th order.

r	$j = 0$	$j = 1$	$j = 2$	$j = 3$	$j = 4$	$j = 5$	$j = 6$	$j = 7$
-1	761/280	-1479/280	2441/280	-8357/840	6343/840	-613/168	171/168	-1/8
0	1/8	481/280	-499/280	481/280	-1007/840	463/840	-25/168	1/56
1	-1/56	15/56	341/280	-219/280	131/280	-167/840	43/840	-1/168
2	1/168	-11/168	73/168	743/840	-307/840	113/840	-9/280	1/280
3	-1/280	29/840	-139/840	533/840	533/840	-139/840	29/840	-1/280
4	1/280	-9/280	113/840	-307/840	743/840	73/168	-11/168	1/168
5	-1/168	43/840	-167/840	131/280	-219/280	341/280	15/56	-1/56
6	1/56	-25/168	463/840	-1007/840	481/280	-499/280	481/280	1/8
7	-1/8	171/168	-613/168	6343/840	-8357/840	2441/280	-1479/280	761/280

This eighth-order table is an amendment to Table 2.1 of Shu [36]. As in Table 2.1, the c_{rj} are weights of interpolating polynomials; k and r denote the order of approximation and the number of grid points to the left of point x_i , respectively.

Appendix B

Measurements generally give values for the velocity derivative skewness of $S_k \approx -0.5$ (note that sometimes the skewness is defined with opposite sign, giving $S_k \approx +0.5$). Whether or not the skewness depends on Reynolds number is still debated. Velocity derivative skewness is related to *vortex stretching*, the basic mechanism of production of small scales in turbulence is as follows: The spectral evolution equation for homogeneous isotropic turbulence [89] is

$$\partial E(\kappa, t)/\partial t = P(\kappa, t) - T(\kappa, t) - D(\kappa, t) \quad (\text{B1})$$

where $E(\kappa, t)$ is the energy spectrum, $P(\kappa, t)$ is a production spectrum, $T(\kappa, t)$ is the nonlinear transfer, and $D(\kappa, t) = 2\nu\kappa^2 E(\kappa, t)$ is the dissipation spectrum. The second moment of this equation is the enstrophy balance [89]

$$\int_0^\infty d\kappa \kappa^2 \partial E(\kappa, t)/\partial t = \int_0^\infty d\kappa \kappa^2 [P(\kappa, t) - T(\kappa, t) - D(\kappa, t)]$$

If, as is usual, production is concentrated at large scales, then

$$\int_0^\infty d\kappa \kappa^2 P(\kappa, t) \approx 0$$

Writing the energy transfer as $T(\kappa, t) = \partial \mathcal{F}(\kappa, t)/\partial \kappa$, where \mathcal{F} is the energy flux,

$$-\int_0^\infty d\kappa \kappa^2 T(\kappa) = \int_0^\infty d\kappa \kappa \mathcal{F}(\kappa)$$

so that $-\int_0^\infty d\kappa \kappa^2 T(\kappa) \geq 0$ if the energy flux is from large to small scales. Thus, in the approximate enstrophy balance

$$\int_0^\infty d\kappa \kappa^2 \partial E(\kappa, t)/\partial t = -\int_0^\infty d\kappa [\kappa^2 T(\kappa, t) + \kappa^2 D(\kappa, t)] \quad (\text{B2})$$

The first term on the right side is a source term that generates enstrophy. Elementary considerations relate this term to vortex stretching [89].^{B1} The Kolmogorov theory asserts that the small scales in any turbulent flow are approximately isotropic and homogeneous, thus, this special analysis for homogeneous isotropic turbulence is believed to apply in much greater generality.

One of the first results of Taylor's statistical theory of turbulence [91] is

$$S_k = \frac{3}{14} \sqrt{30} \frac{\int_0^\infty d\kappa \kappa^2 T(\kappa)}{\left[\int_0^\infty d\kappa \kappa^2 E(\kappa) \right]^{3/2}} \quad (\text{B3})$$

Then, in view of Eq. (B2), velocity derivative skewness S_k is a dimensionless measure of the production of enstrophy, hence of the generation of small scales. The skewness also measures the strength of the nonlinearity: For example, it vanishes in a Gaussian random field. The Batchelor skewness relation

$$-\int_0^\infty d\kappa \kappa^2 T(\kappa, t) = \int_0^\infty d\kappa 2\nu\kappa^4 E(\kappa, t)$$

^{B1}That vortex stretching is in fact positive was demonstrated experimentally by Taylor, who doubted von Kármán's suggestion that vortex stretching vanishes [90].

permits an evaluation of the skewness in terms of integrals over the energy spectrum alone: since

$$\int_0^\infty d\kappa \kappa^2 E(\kappa) = \frac{\epsilon}{\nu},$$

$$S_k = -\frac{3}{14} \sqrt{30} \frac{\int_0^\infty d\kappa 2\nu\kappa^4 E(\kappa)}{\left[\int_0^\infty d\kappa k^2 E(\kappa)\right]^{3/2}} = -\frac{3}{14} \sqrt{30} \left(\frac{\nu}{\epsilon}\right)^{3/2} \int_0^\infty d\kappa 2\nu\kappa^4 E(\kappa) \quad (\text{B4})$$

Explicit evaluation requires knowing the exact energy spectrum, but the trends can be assessed by assuming a model spectrum of the form

$$E(\kappa) = C_K \begin{cases} \epsilon^{2/3} \kappa^{-5/3} & \kappa \leq \kappa_d \\ \epsilon^{2/3} \kappa_d^{-5/3} f(\kappa/\kappa_d) & \kappa \geq \kappa_d \end{cases} \quad (\text{B5})$$

where $\kappa_d = \alpha(\epsilon/\nu^3)^{1/4}$ is proportional to the Kolmogorov microscale and $C_K \approx 1.5$ is the Kolmogorov constant. Experimental and numerical data support the dissipation range form

$$f(\kappa/\kappa_d) = \left(\frac{\kappa}{\kappa_d}\right)^b \exp[a(1 - \kappa/\kappa_d)]$$

Direct interaction approximation (DIA) predicts this form with $b = 2$ and $a \approx 4$. [92]. Assuming the general expression Eq. (B5),

$$S_k = -\frac{3}{14} \sqrt{30} \alpha^{10/3} C_K \left(\frac{3}{5} + 2e^a \int_1^\infty dx x^{4+b} e^{-ax} \right) \quad (\text{B6})$$

Ignoring the dissipation range contribution would result in $S_k \approx -\alpha^{10/3}$.

The most important conclusion is that the result is dominated by the small scales because of the dependence on the parameter α , which determines the scale at which dissipation becomes significant, and the spectrum in the dissipation range.^{B2} However, the value of κ_d itself does not enter Eq. (B6). In this analysis, then, the skewness is independent of Reynolds number; while it remains uncertain whether this conclusion is supported by experimental data, we note that Reynolds number dependence would require a departure from the Kolmogorov spectrum.

The value of the velocity derivative skewness is often taken as a figure of merit to validate numerical schemes; the connection of the skewness to vortex stretching and generation of small scales certainly makes this reasonable. The previous analysis is easily applied to the case of the “numerical turbulence” generated by a finite-difference scheme on a lattice with uniform isotropic spacing h . Following Vreman et al. [64], such numerical turbulence is characterized by the multipliers l_j that express the action of the finite-difference operator D_j on “plane wave” exponential functions,

$$D_j e^{i\kappa \cdot \mathbf{x}} = il_j e^{i\kappa \cdot \mathbf{x}}$$

Vreman et al. gives several examples. We cite the simplest one: the “vertex centered” operator for which

$$l_j = \frac{\sin(\kappa_j h)}{h}$$

The previous analysis can be repeated essentially *verbatim*, replacing wavevector κ and its corresponding wavenumber magnitude $\kappa = |\kappa|$ by \mathbf{l} and $l = |\mathbf{l}|$. The result is a type of regularization of the Navier-Stokes equation in which the lattice spacing h enters as a new parameter. The spectral evolution equation remains valid, but the constant flux Kolmogorov spectrum will be modified

^{B2}Compare Smith and Reynolds [93], although their conclusion that the dissipation range should depend on $e^{-\kappa^2}$ instead of $e^{-\kappa}$ is not supported by data or theory.

by the regularization for scales k near the lattice spacing h : how near depends on the difference scheme. The value of the skewness will depend on the behavior of the numerical spectrum, and a value close to $S_k \approx -0.5$ must not be expected unless the Kolmogorov spectrum can extend to scales significantly larger than h . On the other hand, the sensitive dependence of the skewness to small scale details justifies caution in making positive or negative claims for difference schemes on this basis alone.

Appendix C

Inertial Subrange

A turbulent flow field contains (vortical) structures, which are generally called eddies. There are multiple length scales associated with the eddies of various sizes, starting with the largest eddies having a length scale proportional to the characteristic length of the field and terminating with the small eddies with a length scale proportional to the Kolmogorov length scale. Nonlinear interactions among eddies with a comparably large length scale (i.e., small wavenumber κ) are approximately inviscid in nature and can result in eddies with smaller length scales (i.e., higher wavenumbers). One may view this process as large scale structures breaking up into smaller scale structures.

There is a fluctuating velocity associated with each eddy; and thus, there is a certain kinetic energy corresponding to each eddy. Each fluctuating velocity has a frequency. The largest eddies correspond to low frequencies, and the smallest correspond to high frequencies. Consider a turbulent flow field that is statistically homogeneous with respect to time. Then, the turbulent kinetic energy of an eddy can be represented by a full range of wavenumbers. An ideal energy spectrum for homogeneous isotropic turbulence is displayed in Fig. C1. The spectrum shows that during the initial increase of the wavenumber κ the energy increases, due to the largest eddies in the domain, to a peak level, where the eddies have an integral length scale that is an $O(1)$ fraction of the large scales. Interactions between the eddies with an integral scale start an energy cascade process. The energy decreases as the frequencies of the spectrum increases. It decreases with a slope of $-5/3$, and this part of the energy spectrum which is characterized by the Taylor microscale is often called the Kolmogorov inertial subrange. To have a well defined inertial subrange there must be a sufficiently large Taylor microscale Reynolds number. This regime of the energy spectrum is followed by a region where the smallest eddies are dissipated.

It is difficult to establish an inertial subrange with $\kappa^{-5/3}$ behavior in decaying isotropic turbulence. As indicated by Ishihara [45], a Taylor microscale Reynolds number $Re_\lambda \geq 200$ is required to have an inertial subrange. In order to produce a significant inertial subrange and to investigate the physics of the small scales of isotropic turbulence, an alternative simulation approach is frequently considered. With this approach, a forcing function is introduced to emulate the energy transfer to the inertial subrange from the larger energy containing eddies. Thus, in a simulation the large scales are modeled and the small scales are resolved, and higher Re_λ can be realized, which can result in a sufficiently wide inertial subrange. Due to the steady forcing the turbulence becomes statistically steady.

Since the Taylor microscale Reynolds number for the case being considered is relatively low, and there is no forcing function, we should observe at most a very small inertial subrange. Nevertheless, as a reference, we include the inertial subrange curve which has a $-5/3$ slope. This facilitates comparing with results from other investigators who include this curve.

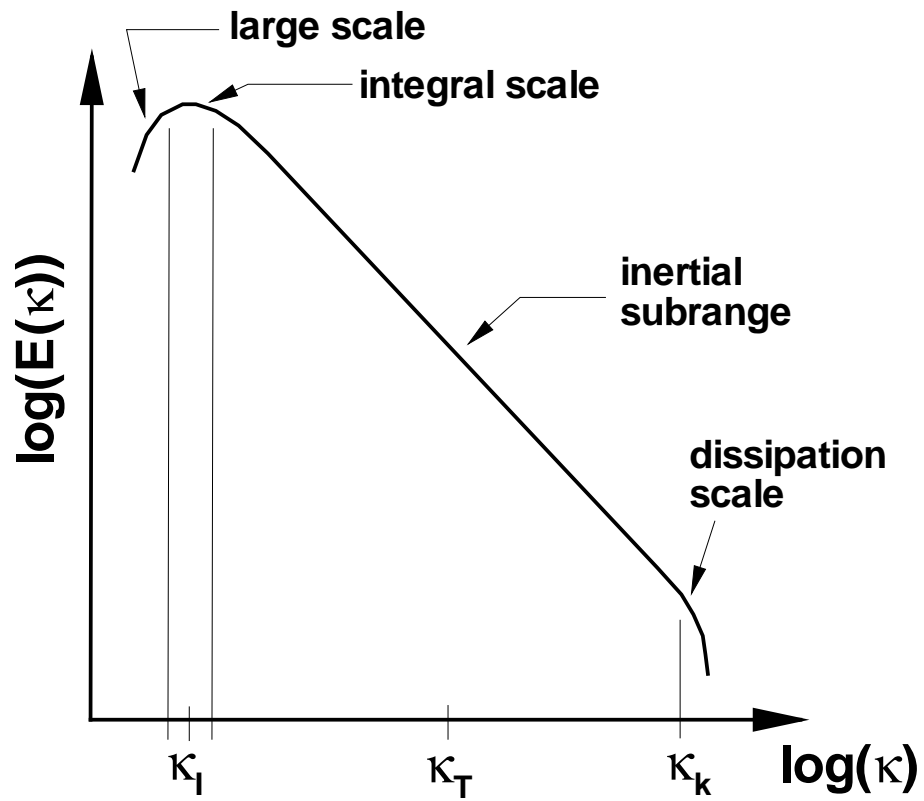


Figure C1. Sketch of Kolmogorov energy spectrum indicating length scales corresponding to different parts of the spectrum.

REPORT DOCUMENTATION PAGE

*Form Approved
OMB No. 0704-0188*

The public reporting burden for this collection of information is estimated to average 1 hour per response, including the time for reviewing instructions, searching existing data sources, gathering and maintaining the data needed, and completing and reviewing the collection of information. Send comments regarding this burden estimate or any other aspect of this collection of information, including suggestions for reducing this burden, to Department of Defense, Washington Headquarters Services, Directorate for Information Operations and Reports (0704-0188), 1215 Jefferson Davis Highway, Suite 1204, Arlington, VA 22202-4302. Respondents should be aware that notwithstanding any other provision of law, no person shall be subject to any penalty for failing to comply with a collection of information if it does not display a currently valid OMB control number.
PLEASE DO NOT RETURN YOUR FORM TO THE ABOVE ADDRESS.

1. REPORT DATE (DD-MM-YYYY) 01-08-2012		2. REPORT TYPE Technical Memorandum		3. DATES COVERED (From - To)	
4. TITLE AND SUBTITLE Parametric Study of Decay of Homogeneous Isotropic Turbulence Using Large Eddy Simulation				5a. CONTRACT NUMBER	
				5b. GRANT NUMBER	
				5c. PROGRAM ELEMENT NUMBER	
6. AUTHOR(S) Swanson, R. C.; Rumsey, Christopher L.; Rubinstein, Robert; Balakumar, Ponnampalam; Zang, Thomas A.				5d. PROJECT NUMBER	
				5e. TASK NUMBER	
				5f. WORK UNIT NUMBER 561581.02.08.07.46.04	
7. PERFORMING ORGANIZATION NAME(S) AND ADDRESS(ES) NASA Langley Research Center Hampton, VA 23681-2199				8. PERFORMING ORGANIZATION REPORT NUMBER L-20152	
9. SPONSORING/MONITORING AGENCY NAME(S) AND ADDRESS(ES) National Aeronautics and Space Administration Washington, DC 20546-0001				10. SPONSOR/MONITOR'S ACRONYM(S) NASA	
				11. SPONSOR/MONITOR'S REPORT NUMBER(S) NASA/TM-2012-217593	
12. DISTRIBUTION/AVAILABILITY STATEMENT Unclassified - Unlimited Subject Category 02 Availability: NASA CASI (443) 757-5802					
13. SUPPLEMENTARY NOTES					
14. ABSTRACT Numerical simulations of decaying homogeneous isotropic turbulence are performed with both low-order and high-order spatial discretization schemes. The turbulent Mach and Reynolds numbers for the simulations are 0.2 and 250, respectively. For the low-order schemes we use either second-order central or third-order upwind biased differencing. For higher order approximations we apply weighted essentially non-oscillatory (WENO) schemes, both with linear and nonlinear weights. There are two objectives in this preliminary effort to investigate possible schemes for large eddy simulation (LES). One is to explore the capability of a widely used low order computational fluid dynamics (CFD) code to perform LES computations. The other is to determine the effect of higher order accuracy (fifth, seventh, and ninth order) achieved with high-order upwind biased WENO-based schemes. Turbulence statistics, such as kinetic energy, dissipation, and skewness, along with the energy spectra from simulations of the decaying turbulence problem are used to assess and compare the various numerical schemes. In addition, results from the best performing schemes are compared with those from a spectral scheme. The effects of grid density, ranging from 32 cubed to 192 cubed, on the computations are also examined. The fifth-order WENO-based scheme is found to be too dissipative, especially on the coarser grids. However, with the seventh-order and ninth-order WENO-based schemes we observe a significant improvement in accuracy relative to the lower order LES schemes, as revealed by the computed peak in the energy dissipation and by the energy spectrum.					
15. SUBJECT TERMS Isotropic decay; Large eddy simulation; Numerical methods; Turbulence					
16. SECURITY CLASSIFICATION OF:			17. LIMITATION OF ABSTRACT	18. NUMBER OF PAGES	19a. NAME OF RESPONSIBLE PERSON
a. REPORT	b. ABSTRACT	c. THIS PAGE			STI Help Desk (email: help@sti.nasa.gov)
U	U	U	UU	74	19b. TELEPHONE NUMBER (Include area code) (443) 757-5802